To The Graduate Council:

I am submitting herewith a thesis written by Richard John Wilk entitled "Structure Variations Through the Thickness of Poly(ethylene terephthalate) Films: Characterization and Mechanism of Formation." I have examined the final copy of this thesis for form and content and recommend that it be accepted in partial fulfillment of the requirements for the degree of Master of Science, with a major in Polymer Engineering.

J. E. Spruiell, Major Professor

We have read this thesis
and recommend its acceptance:

Edward S. Clark

Kenneth J. Mackay

Accepted for the Council:

Vice Provost
and Dean of The Graduate School

CLEMSON CREST

STATEMENT OF PERMISSION TO USE

In presenting the thesis in partial fulfillment of the requirements for a Master's degree at The University of Tennessee, Knoxville, I agree that the Library shall make it available to borrowers under rules of the Library. Brief quotations from this thesis are allowable without special permission, provided that accurate acknowledgments of source is made.

Permission for extensive quotation from or reproduction of this thesis may be granted by my major professor, or in his absence, by the Head of Interlibrary Services when, in the opinion of either, the proposed use of the material is for scholarly purposes. Any copying or use of the material in this thesis for financial gain shall not be allowed without my written permission.

Signature Richard John Wilk

Date August, 1987

STRUCTURE VARIATIONS THROUGH THE THICKNESS OF POLY(ETHYLENE TEREPHTHALATE) FILMS: CHARACTERIZATION AND MECHANISM OF FORMATION

A Thesis

Presented for the

Master of Science

Degree

The University of Tennessee, Knoxville

Richard John Wilk

August 1987

To My Father

and

In Memory of My Mother

ACKNOWLEDGMENTS

The author would like to extend his gratitude to the many people who have aided him throughout the course of this investigation. First and foremost, he would like to thank his advisor Dr. J.E. Spruiell for his constant support and patience during the course of the project. Thanks is also extended to Dr. J.L. White for suggesting the area of research, Dr. D.C. Bogue for his assistance in the early stages of the project, Dr. E.S. Clark for serving as a member of his advisory committee and Dr. E. Graham for his help in preparing microtomed specimens.

It is a pleasure to acknowledge the help and cooperation of the staff of the Film Division of American Hoechst Corporation with whom the author was employed for a portion of his graduate studies. The author would like to thank the following: Mr. J. Penoyer for his constant support and interest in the project, Dr. K. Mackenzie for the implementation and support of the program and Mr. G. Funderburk, Dr. M. Ledbetter, Mr. S. Gust and Mr. J. Veatch for their many helpful discussions throughout the course of the project. The author would like to thank Dr. H.A. Davis at E.I. duPont de Nemours and Co. for providing interference microscopy measurements and for his helpful comments and suggestions. Most importantly the author wishes to thank the Polymer Consortium for providing financial support.

ABSTRACT

An exploratory study was conducted to determine the existence, magnitude and techniques required to characterize through the thickness inhomogeneity in oriented poly(ethylene terephthalate) (PET) films. Variations in through the thickness orientation and morphology are the result of a temperature gradient existing within the film during deformation. A review of experimental techniques was made in order to determine the most suitable and sensitive techniques currently available for characterizing through the thickness inhomogeneity.

A series of single and multilayer oriented films was prepared from cast sheet samples having superimposed temperature gradients present through the thickness prior to stretching. Density, thermal analysis, birefringence and microscopy were used to characterize the stretched samples. Films were characterized both in terms of average properties and in relation to through the thickness variations. The effect of temperature and strain rate on bulk properties of homogeneous (nongradient) and heterogeneous (gradient) films was investigated.

Laminate films were used as a means of characterizing gradient films and to demonstrate the magnitude of through thickness structural gradients. Small-angle light scattering (SALS) patterns of the individual layers of laminate films revealed significant differences in

superstructure present within the layers. Chemical etching of heterogeneous oriented films with n-propylamine showed major differences in surface-to-surface etch patterns, whereas nongradient films exhibited similar etch patterns on both surfaces.

The present study considers the use of critical angle refractometry and the interferometry as practical techniques for the detection and characterization of through the thickness inhomogeneity in oriented PET films. A detailed description of the general principles of measurement, the instruments and the experimental procedure associated with each of the techniques is presented. The advantages and limitations of each technique are also discussed.

TABLE OF CONTENTS

CHAPTER		PAGE
I.	INTRODUCTION	1
II.	BACKGROUND AND LITERATURE REVIEW	5
	A. PET FILMS: PROCESSING, STRUCTURE AND PROPERTIES	5
	a. General	5
	b. Chill-Roll Cast Film Process	6
	c. Basic Structure of PET	12
	Chemical Structure	12
	Crystal Structure	13
	d. Typical Properties of PET Films	16
	Chemical Properties	16
	Physical Properties	16
	B. PET FILMS: CRYSTALLIZATION, MORPHOLOGY AND DEFORMATION BEHAVIOR	17
	a. Quenched PET Films	17
	Heat Transfer Phenomena	17
	Structure Studies	21
	b. Crystallization Behavior of PET	23
	Quiescent Crystallization	23
	Stress-Induced Crystallization	24
	c. Drawing Behavior	34
	C. TECHNIQUES FOR CHARACTERIZING INHOMOGENEITY IN POLYMER FILMS	36
	a. Optical Microscopy	44
	Polarized Light Studies	44
	Determination of Birefringence	49
	Compensators	50
	b. Refractometry	53
	Basic Principles	53
	Abbe Refractometer	57
	Application to Anisotropic Solids	61
	c. Interferometry	66
	Theory	66
	d. The Interference Microscope	69
	Double-Beam Type	70
	Multiple-Beam Type	74
	Measurement and Calculation of Refractive Index	80
	Application to Inhomogeneity in Polymer Films	83

CHAPTER PAGE

e. Electron Microscopy 91
Scanning Electron Microscopy 92
Transmission Electron Microscopy 94

III. MATERIAL AND EXPERIMENTAL PROCEDURES 96

A. MATERIAL 96

B. SAMPLE PREPARATION 96
a. Slab Films 96
b. Laminate Films 98
c. Stretching of Cast Sheet 101
d. Force--Elongation Measurements 103

C. CHARACTERIZATION OF CAST SHEET AND DRAWN FILMS: AVERAGE PROPERTIES 105
a. Density Measurements 105
b. Differential Scanning Calorimetry . . . 105
c. Refractive Index Measurements. 106
d. Small-Angle Light Scattering 107

D. CHARACTERIZATION OF THROUGH THE THICKNESS VARIATIONS IN CAST SHEET AND DRAWN FILMS . . 109
a. Heat Transfer Studies. 109
b. Cutting and Polishing of Slabs for Birefringence 110
c. Birefringence Measurements on Slabs . . 110
d. Refractive Index Measurements on Laminate Films 111
e. Preparation of Thin Sections for Microscopy 112
f. Refractive Index Measurements Using an Interference Microscope 113
g. Polarized Light Microscopy 114
h. Chemical Etching 117

IV. CHARACTERIZATION OF CAST SHEET AND DRAWN FILMS: AVERAGE PROPERTIES 118

A. CAST SHEET 118
a. Density and DSC 118
b. Refractive Index and Birefringence . . . 119
c. Crystallization Behavior 121

B. NONGRADIENT DRAWN FILMS 125
a. Drawing Behavior 125
b. Density 125
c. Birefringence 129
d. Small-Angle Light Scattering 135

CHAPTER PAGE

C. COMPARISON OF NONGRADIENT AND GRADIENT DRAWN FILMS 137
a. Heat Transfer Theory 137
b. Deformation Behavior 142
c. Birefringence 146

V. CHARACTERIZATION OF DRAWN FILMS: THROUGH THE THICKNESS VARIATIONS 150

A. CHARACTERIZATION TECHNIQUES 150
a. Birefringence 150
b. Refractive Index 156
c. Microscopy 160

B. CAST SHEET AND GRADIENT DRAWN FILMS 162
a. Heat Transfer Analysis 162
b. Surface-to-Surface Variations in Refractive Index and Birefringence Obtained Using an Abbe Refractometer. . 166
c. Refractive Index and Birefringence Obtained from Interference Microscopy 170

C. LAMINATE FILMS 179
a. General Characteristics 179
b. Birefringence 179
c. DSC Results 184
d. Small-Angle Light Scattering 187
e. Chemical Etching 194
Optical Microscopy 194
Scanning Electron Microscopy 196

VI. CONCLUSIONS 201

VII. RECOMMENDATIONS 202

LIST OF REFERENCES 203

APPENDIX 213

VITA 219

LIST OF TABLES

TABLE		PAGE
II-1.	Refractive Index Readings Obtained Using an Abbe Refractometer	64
III-1.	Characteristics of PET Cast Sheet	97
III-2.	Laminate Films for Refractive Index Measurements	99
III-3.	Conditions Prior to Stretching Cast Sheet Samples	104
III-4.	Experimental Modes for Determining Refractive Indices from Interference Microscopy Measurements	116
IV-1.	Thermal Characteristics of Cast Sheet Samples	120
IV-2.	Average Refractive Indices of Cast Sheet Samples	122
IV-3.	Birefringence Results on Cast Sheet	123
IV-4.	Thermal Properties of PET	140
IV-5.	Influence of Residence Time on the Predicted Average Temperatures in Cast Sheet Sample C5	141
IV-6.	Comparison of Nongradient and Gradient Drawn Films	149
V-1.	Through the Thickness Birefringence Values for Cast Sheet Sample C5	155
V-2.	Birefringence Results on Cast Sheet Samples Using the Compensator Technique	157
V-3.	Surface-to-Surface Variations in Refractive Index of Cast Sheet Samples	167
V-4.	Surface-to-Surface Variations in Birefringence of Cast Sheet Samples	168

TABLE PAGE

V-5. Differential Birefringences of Cast Sheet and Selected Nongradient and Gradient Uniaxial Films 169

V-6. Samples for Interference Microscopy 171

V-7. Comparison of Birefringence Results 178

V-8. Density and Birefringences of the Individual Layers of UCW Laminate Film GL2 183

V-9. Thermal Characteristics of Gradient One-Piece and Laminate Films 190

LIST OF FIGURES

FIGURE		PAGE
II-1.	Generalized diagram of a process line for the production of biaxially oriented polymer film	7
II-2.	Uniaxial stretching methods: (a) process using nip rolls; (b) process using driven and idle rolls	10
II-3.	Tenter frame for transverse stretching of polymer film	11
II-4.	Chemical structure: (a) bis(β-hydroxyethyl terephthalate) (DHET); (b) poly(ethylene terephthalate) (PET) and (c) diethylene glycol (DEG)	14
II-5.	Azimuths of vibration within a birefringent medium. The optic axis of the medium is parallel to the plane of the page and oriented in the direction shown	38
II-6.	Refractive index ellipsoids: (a) optically isotropic medium and (b) optically anisotropic medium	40
II-7.	Illustration of a fiber and the central section of its refractive index ellipsoid. The optic axis is inclined 30 degrees to the fiber axis	42
II-8.	Film strip showing the projections of the refractive index ellipsoid on the three sides of a polymer film	43
II-9.	The polarizing microscope	45
II-10.	Function of the polarizer and analyzer	46
II-11.	Interference fringe patterns in oblique fiber cross sections: (a) fiber having homogeneous radial structure; (b) and (c) fiber exhibiting radial variations and (d) conditions for fringe formation	48

FIGURE		PAGE
II-12.	Tilting plate compensator: (a) Position of minimum compensation (neutral position); intermediate position and (c) position of maximum compensation	51
II-13.	Phenomenon of refraction	55
II-14.	Diagram of a prism refractometer	56
II-15.	The Abbe′ refractometer and its essential components: (a) refractometer and sodium vapor lamp and (b) close-up of prisms	58
II-16.	Cross section of an Abbe′ refractometer: (a) solid plate; (b) liquid film and (c) liquid film with light incident in a manner different than in (b)	60
II-17.	Diagram showing position of film between the prisms of an Abbe′ refractometer. Polarized components of limiting rays are refracted separately at point B	62
II-18.	Schematic of the Abbe′ refractometer: P_i, illuminating prism; P_r, refracting prism; S, sample; L, contacting liquid; n_r, n_L, and n_S represent the refractive indices of P_r, L and S, respectively; (b) positions of glass prisms with different refractive indices on the refracting prism. Arrows indicate path of light beam	65
II-19.	The interference of light	68
II-20.	Principle of operation of the Leitz interference microscope	71
II-21.	The Leitz Interference Microscope. (a) Scematic and (b) illustration showing actual components	72
II-22.	Transverse interference patterns of PET fibers under an interference microscope: (a) 2,000 m/min; (b) 9,000 m/min (symmetric interference fringe pattern) and (c) 9,000 m/min (asymmetric interference fringe pattern), (b) and (c) are the same sample observed from different directions	75

FIGURE		PAGE
II-23.	Straight line fringes produced by a wedge: (a) small angle between plates and (b) wedge angle increased	77
II-24.	Reflection and transmission from parallel plates: (a) wedge; (b) fringe pattern and (c) ray diagram	78
II-25.	Multiple-beam interference microscope	79
II-26.	Fringes of equal chromatic order from polymers: (a) a polyethylene oxide spherulite at room temperature; (b) a polypropylene spherulite growing at 140^{o}C and (c) after sample in (b) has cooled to room temperature	81
II-27.	(a) Intensity distribution of double-beam interference fringe pattern. (b) The dependence of color and color mixing on wavewlength in a fringe system	82
II-28.	(a) Fringe pattern produced by the interference of light in the image field of a double-beam interference microscope. (b) The fringe displacement produced by a large optically homogeneous section. The solid and broken curves represent fringe patterns in background and section, respectively	85
II-29.	Sections of a polymer film for interference microscopy measurements	86
II-30.	Determination of principal refractive indices through the use of film sections	87
II-31.	Fringe distortion produced by a flat piece of mica between a wedge. The complex pattern is entirely due to wrinkling of the sample, not to differences in thickness or refractive index	90
II-32.	Diagrams of electron microscopes: (a) scanning electron microscope and (b) transmission electron microscope	93
III-1.	Cross section of laminate film	100
III-2.	Deformation modes	102

FIGURE		PAGE
III-3.	Principal refractive indices of a polymer film	108
III-4.	Determination of the principal refractive of a polymer film indices by interference microscopy using sections	115
IV-1.	Effect of residence time on crystallization cast sheet sample C5	124
IV-2.	Stress--strain curves for uniaxial film NGB as a function of strain rate at various temperatures	126
IV-3.	Stress--strain curves for UCW film NGB as a function of strain rate at various temperatures	127
IV-4.	Effect of temperature on crystallization of stretched films: (a) uniaxial NGA; (b) uniaxial NGB; (c) UCW NGA and (d) UCW NGB at various strain rates	128
IV-5.	Effect of strain rate on crystallization of stretched films: (a) uniaxial NGA; (b) uniaxial NGB; (c) UCW NGA and (d) UCW NGB at various temperatures	130
IV-6.	Variation of birefringence with temperature for uniaxial films: (a) NGA and (b) NGB . . .	131
IV-7.	Variation of birefringence with temperature for UCW films: (a) NGA and (b) NGB	132
IV-8.	Variation of birefringence with strain rate for uniaxial films: (a) NGA and (b) NGB . . .	133
IV-9.	Variation of birefringence with strain rate for UCW films: (a) NGA and (b) NGB	134
IV-10.	Effect of temperature on H_v patterns for uniaxial film sample NGB1 drawn at 10.0 min^{-1}	136
IV-11.	Effect of strain rate on H_v and V_v patterns for uniaxial film NGB1	138

FIGURE		PAGE
IV-12.	Photographs of nongradient uniaxial films: (a) NGB1 and (b) NGB2	143
IV-13.	Photgraphs of gradient uniaxial films: (a) GA3 and (b) GB3	144
IV-14.	Photographs of nongradient and gradient UCW films: (a) NGB1 and (b) GA3	145
IV-15.	Stress--strain curves for gradient uniaxial film GA3	147
IV-16.	Stress--strain curves for gradient uniaxial film GB3	148
V-1.	Cross section of slab film used for birefringence measurements	152
V-2.	Birefringence profile for a (0.125 in.) PET slab quenched from the melt (290°C) in ice water	154
V-3.	Refractive index distribution through the thickness of laminate PET films quenched from the melt (290°C) in ice water: (a) L1 and (b) L3. Equal cooling rates at the outer surfaces	158
V-4.	Refractive index distribution through the thickness of laminate PET films quenched from the melt (290°C) in ice water: (a) L2 and (b) L4. Unequal cooling rates at the outer surfaces	159
V-5.	Optical photomicrographs of TD cross sections of uniaxial stretched films in polarized light: (a) NGB1; (b) GA3 and (c) GB3. All films drawn at 10.0 min^{-1}	161
V-6.	SEM photomicrographs of TD cross sections of film samples of uniaxial stretched films: (a) NGB1 (80°C); (b) NGB3 (100°C); (c) GA3 (70--120°C) and (d) GB3 (50--150°C). All films drawn at 10.0 min^{-1}	163
V-7.	Temperature profiles for cast sheet sample C5 prior to stretching: Air stream temperatures: T_C = 70°C and T_H = 120°C . . .	164

FIGURE PAGE

V-8. Temperatures profiles for cast sheet sample C5 prior to stretching: Air stream temperatures: T_C = 50°C and T_H = 150°C . . . 165

V-9. Refractive index profiles through the thickness of the film sample obtained from interference microscopy 173

V-10. Refractive index profiles through the thickness of the bottle sample obtained from interference microscopy 174

V-11. Birefringence profiles through the thickness of the film sample obtained from interference microscopy 175

V-12. Birefringence profiles through the thickness of the bottle sample obtained from interference microscopy 176

V-13. Photographs of uniaxial laminate films drawn at 10.0 min^{-1}: (a) NGL1 and (b) GL2 180

V-14. Photographs of UCW laminate films drawn at 10.0 min^{-1}: (a) NGL1 and (b) GL2 181

V-15. Photograph showing the comparison between nongradient (NGL2) and gradient (GL2) uniaxial laminate films. Both films drawn at 10.0 min^{-1}. 182

V-16. DSC thermograms of gradient uniaxial laminate film GL2 drawn at 10.0 min^{-1} 185

V-17. DSC thermograms of gradient UCW laminate film GL2 drawn at 10.0 min^{-1} 186

V-18. DSC thermogram of the glass transition region of gradient uniaxial film GB3 188

V-19. DSC thermogram of the glass transition region for gradient UCW film GL2 (Layer 1) 189

V-20. SALS H_v and V_v patterns from the individual layers of uniaxial laminate film GL2 drawn at 10.0 min^{-1} 191

FIGURE		PAGE
V-21.	Diagram of the layered structure of a thin polymer film	193
V-22.	SALS H_v and V_v patterns from uniaxial gradient films drawn at 10.0 min^{-1}: (a) GB3 (one-piece) and (b) GL2 (4--layer laminate) .	195
V-23.	Optical photomicrographs of n-propylamine etched uniaxial films drawn at 10.0 min^{-1}: (a) Unetched NGB1 (80°C), (b) Cast Sheet C5, (c) NGB1 (80°C), (d) NGB2 (90°C), (e) NGB3 (100°C) and (f) NGB4 (110°C)	197
V-24.	Optical photomicrographs of n-propylamine etched uniaxial films drawn at 10.0 min^{-1}: (1) GA3: (a) Cold (70°C), (b) Hot (120°C) and (2) GB3: (a) Cold (50°C), Hot (150°C)	198
V-25.	SEM photomicrographs of TD fracture surfaces of uniaxial films drawn at 10.0 min^{-1}: (a) NGB1 (80°C); (b) NGB3 (100°C); (c) GA3 (70--120°C); (d) GB3 (50--150°C) and Cast Sheet C5	199

CHAPTER I

INTRODUCTION

Oriented poly(ethylene terephthalate) film constitutes an important part of the commercial film market (98). The U.S. market for all applications of PET film which represents about half of the total worldwide market, totaled about 400 million lb in 1981. The domestic market is expected to grow at about eight percent anually to 1990 (99). The largest single use category in the U.S. for biaxially oriented PET film is packaging including metallized products (98). However, magnetic tape, especially consumer video tape is forecast to become a major growth area in the decade ahead (99).

The properties of PET film depend on the level of crystallinity and degree of orientation produced during processing (49). The particular end-use application dictates the specific combination of properties required. Clarity is important in packaging applications, whereas surface adhesion and dimensional stability are critical where the film is used as a substrate for magnetic tape. Since these properties depend on the morphology of the film and its variations within the film, an examination of any through the thickness inhomogeneity would provide some insight into the causes of product variability. This

information might be useful in preventing undesirable fluctuations in quality.

Several variations of the cast film process are commercially used to produce oriented PET films. These typically include extrusion of the molten polymer, rapid quenching to a glassy state, orientation by stretching at a temperature above the glass transition followed by some type of thermal treatment to stabilize or relax the film. One of the more important parts of the process is the stretching stage. During this part of the process the film is believed to be homogeneously deformed above the glass transition temperature. If however, the deformation is not homogeneous, that is different parts of the film deform and thus orient at different rates, variations in properties will be observed. Since intermittent variations in properties do not deter the use of the film in many applications these variations and their causes have not been the subject of detailed study.

A polymer film subjected to deformation in the presence of a superimposed through the thickness temperature gradient could be expected to exhibit a heterogeneous deformation profile. In polymeric materials where deformation serves to produce molecular orientation, any such heterogeneity should be reflected in a similar variation in orientation. Futhermore in semicrystalline polymers such as PET, a variation in crystalline structure is also likely to exist.

Most of the studies of the influnce of temperature gradients on polymer morphology have been concentrated in the area of injection molding. Clark (16,17) and Clark and Garber (18,38) have shown that the temperature gradients that occur in polymers during processing produce significant changes in their crystalline superstructure. They reported results on injection molded polyoxymethylene (16) which related variations in crystalline superstructure to processing variables such as mold temeprature and injection pressure. Both variables were found to influence the crystallization rates and temperature gradients within the polymer during processing. Optical microscopy of injection molded specimens revealed a highly oriented fibrillar surface layer encapsulating a spherulitic core. Some samples were observed to have a transcrystalline layer. Similar studies were conducted on blown films (17).

Clark (16) also studied the effect of thermal gradients on injection molded polypropylene. Using wide-angle x-ray scattering (WAXS) and optical microscopy he was able to observe several different layered crystalline morphologies. The size of these layers was shown to be strongly dependent on the temperature gradients existing in the material duirng processing.

A few studies have been conducted on the extrusion of polymer films (90,121,125). Little, if any, attention has

been given to the possibility of significant thermal gradients occurring during the drawing of a film.

This thesis represents an exploratory study of the influence of superimposed thermal gradients in PET films prior to stretching in relation to through the thickness structure development, orientation and overall deformation behavior. Since most standard characterization techniques are not suited to the study of structural inhomogeneity in thin films, a survey of experimental methods was conducted to determine the most appropriate techniques. The use of critical angle refractometry and interferometric techniques, particularly the use of interference microscopy as methods of characterizing through the thickness structural inhomogeneity were investigated.

CHAPTER II

BACKGROUND AND LITERATURE REVIEW

A. PET FILMS: PROCESSING, STRUCTURE AND PROPERTIES

a. General

Since the discovery of poly(ethylene terephthalate) by Whinfield and Dickson (148,149) in the late 1940's and the commercial introduction of PET in the form of a film in 1954, the polymer has captured a significant portion of the synthetic fiber and film markets. The commercial success of PET as a film can be attributed to the broad range of mechanical, optical and electrical properties available.

Biaxially oriented, semicrystalline PET films, produced by the chill-roll cast film process are strong, tough, flexible and have low moisture absorption and low gas permeabilities (49). PET films also have excellent chemical resistance and dielectric properties. Such characteristics make PET attractive for many commercial applications. Among these are packaging, magnetic tape, capacitor dielectrics and industrial belting. Its unique combination of physical and chemical properties meet the rigorous standards of the magnetic tape industry including use as audio, video and computer tapes. Most important in this application are the maintenance of dimensional stability and film thickness uniformity, variations of these properties result in loss of signal and poor overall performance. PET film is also used

in packaging applications especially as a base for heat-sealable laminates or in multilayer coated films. PET is also the choice as a substrate for photographic and x-ray films. An extensive review on the manufacture and uses of polyester films is presented by Heffelfinger and Knox (52).

b. Chill-Roll Cast Film Process

The cast film process used to commercially manufacture biaxially oriented PET film involves three main operations: 1. extrusion and quenching, 2. orientation and 3. annealing. A generalized diagram of a typical film processing line is shown in Figure II-1.

In the first operation or stage, molten polymer is vertically extruded from a silt die onto a internally cooled highly polished metal roll commonly referred to as a chill-roll. The film rapidly cools to an amorphous state which is metastable at room temperature.

Rapid cooling is an essential part of this stage of the process since the extruded film will crystallize if cooled slowly. This would produce a material that is opaque, brittle and difficult to stretch. The thickness of the extruded film is limited by the rate of heat transfer between the film and the chill roll, a direct consequence of the poor thermal conductivity of the polymer. To ensure intimate contact between the film and the chill-roll and thus aid in cooling the film, an air knife or other pinning device is used. Orientation is produced in the film in the

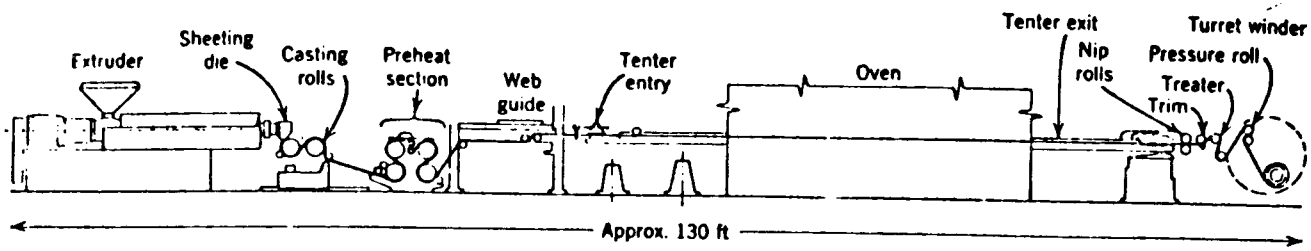


Figure II-1. Generalized diagram of a process line for the production of biaxially oriented polymer film.

Source: Mauro, J.B. and J.J. Levitsky in "The Science and Technology of Polyester Films", Vol. 1, O. Sweeting Ed., Wiley-Interscience, New York (1968), p. 474.

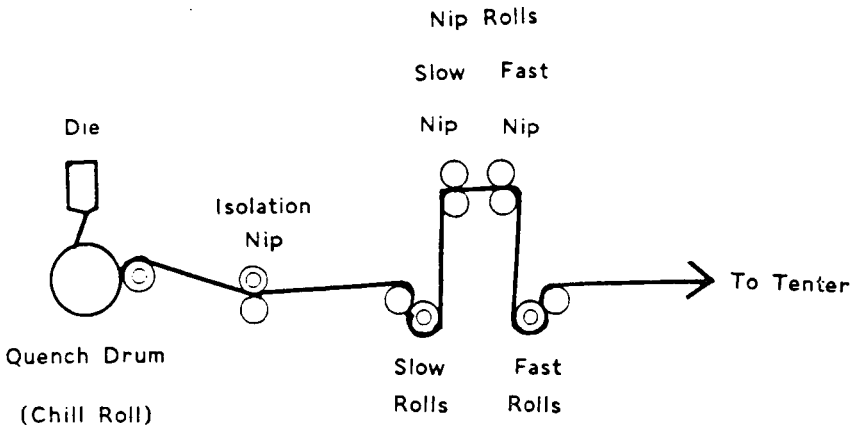
second stage of the process. Stresses developed in the film during stretching cause a preferential alignment of polymer chains in the stretch direction. A biaxially oriented film can be produced in-line immediately following the postextrusion quench by either simultaneous or sequential stretching. An overview of some of the process technology is described in the patent literature (2,3,48,69,74,85, 95,119,136). A more detailed review of the process technology is given by Mauro and Levitsky (78). The most noteworthy patent is that of Scarlett (119), who describes a sequential process for stretching PET film. Scarlett also discusses the influence of process conditions upon film properties.

In the sequential process, the film is first stretched in the machine direction and then in the transverse direction. Prior to being stretched in the machine direction, the film is heated to a temperature slightly above its glass transition temperature (T_g). The most common method employed in heating the film is to pass it between two pairs of heated nip rolls, the second pair of rolls rotating faster than the first. As the film passes through the first pair of rolls, it is heated to the stretching temperature and is subjected to a draw tension. The amount of uniaxial stretch or draw is determined by the speed of the second set of rolls. Machine direction drawing is carried out at temperatures within the 80^{o}C to

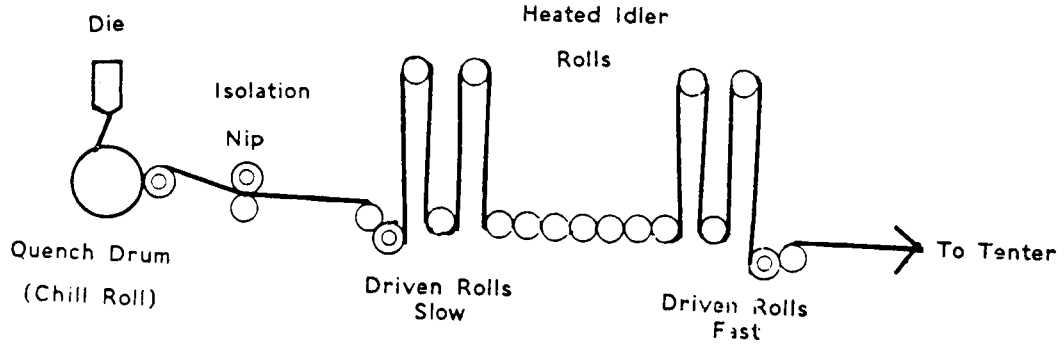
90°C range; at these temperatures the work required to stretch the film is at a minimum (59). Typical draw ratios range from 2.5 to 3.5 times the original dimensions (49). An alternate method of stretching the film in the machine direction, involves passing the film over a series of idle and driven rolls. Both methods are illustrated in Figure II-2.

The film at this point in the process has superior mechanical properties as compared to the quenched film. Uniaxially stretched film is slightly crystalline, a result of stress-induced crystallites produced during drawing.

The most common means of producing transverse or lateral orientation in the film is achieved with the aid of a tenter frame. A tenter frame consists of a series of film gripping devices attached to a continuosly moving endless chain. The chain is guided along channel rails that diverge at the center of the web as shown in Figure II-3. Thus the film is stretched as a direct consequence of the rails of the frame diverging along its length. Prior to being stretched transversely the film is cooled slightly and then reheated. This process aids in establishing a uniform temperature through the cross section. Transverse drawing is performed at slightly higher temperatures in order to keep the work required to a minimum. The tenter frame is enclosed in an oven composed of several different independent zones which can either heat or cool the film



(a)



(b)

Figure II-2. Uniaxial stretching methods: (a) process using nip rolls; (b) process using driven and idle rolls.

Source: Heffelfinger, C.J., Polym. Eng. Sci., 18, 1166 (1978).

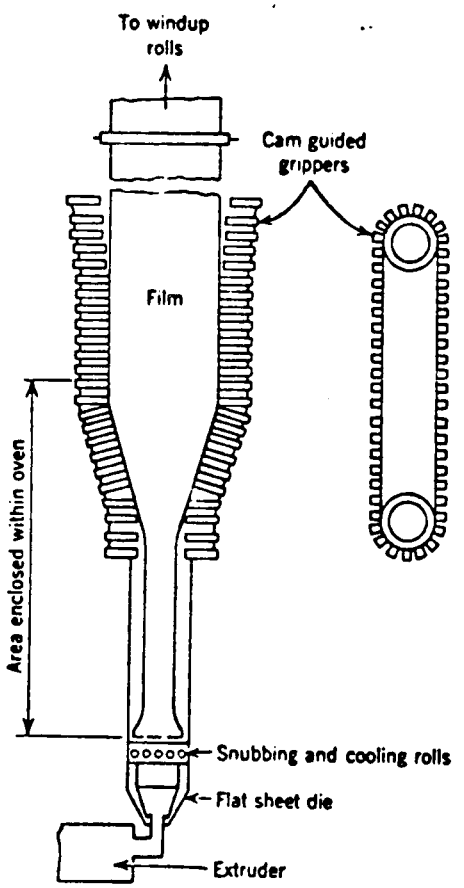


Figure II-3. Tenter frame for transverse stretching of polymer film.

Source: Mauro, J.B. and J.J. Levitsky in "The Science and Technology of Polyester Films", Vol. 1, O. Sweeting Ed., Wiley-Interscience, New York (1968), p. 473.

while it is being stretched. The film may be subjected to various heat-setting or annealing treatments which improve the thermal stability of the final product. Typically, the biaxially oriented product is stabilized by heating the film to temperatures above 200°C while under restraint (40).

Many variations of the process are possible, including simultaneous and poststretching in the machine direction to produce so-called "tensilized" film. An indepth description of the process is presented by Heffelfinger and Knox (52).

c. Basic Structure of PET

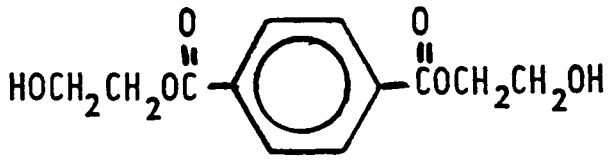
A voluminous literature exists on the structure and properties of PET. A complete review is presented by Korshak and Vinogradova (75). A brief summary follows:

Chemical Structure. PET is produced by the polymerization of bis(2-hydroxy ethyl) terephthalate. Commercially, the monomer is formed as an intermediate from either of two synthesis routes. Bis (2-hydroxy ethyl) terephthalate is synthesized by the tranesterification of dimethyl terephthalate (DMT) with ethylene glycol or by the direct esterification of terephthalic acid (TA) and ethylene glycol (26). Both routes produce a by-product which must be separated from the reaction product. In the transesterification route, methanol is produced, whereas in the direct esterification method the by-product is water. In both cases, the by-product is removed from the product mixture by distillation. The high molecular weight species

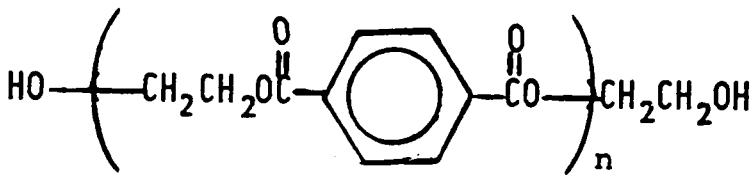
is formed by heating the reaction mixture above its melting point under reduced pressure. A vacuum is required to facilitate rapid removal of excess water or glycol. The reaction is carried out in the presence of a catalyst. Typically, the resulting polymer has an average degree of polymerization of about 75 and a number average molecular weight (M_n) of around 15,000 (49,55). A major undesirable side reaction is the formation of an ether diethylene glycol (DEG) (2,2'-oxydiethanol) a result of the dehydration of ethylene glycol (26). Some DEG becomes incorporated into the chain as 3-oxapentamethylene terephthalate units. These units disrupt the stereoregularity of the backbone and thus influence the rate and level of crystallinity in the film. It has been reported that PET is a copolyester generally containing a variable amount of about one to five mole percent DEG (29,54). Chemical structures are shown in Figure II-4.

The chemical structure of PET can be characterized as having several important features including; a chain composed of planar molecules, carbonyl groups in the trans conformation tilted approximately 12 degrees out-of-the-plane of the benzene rings forming a linear chain without "kinks", and polymer molecules capable of crystallizing (49).

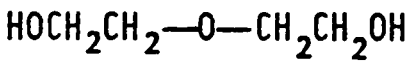
Crystal Structure. The crystal structure of PET was first studied by Daubeny, Bunn and Brown (23) and has since



(a)



(b)



(c)

Figure II-4. Chemical structure:
(a) bis(β-hydroxyethyl terephthalate) (DHET);
(b) poly (ethylene terephthalate) (PET) and (c) diethylene glycol (DEG).

Source: Heffelfinger, C.J. and K.L. Knox in "The Science and Technology of Polymer Films", Vol. 2, O.J. Sweeting Ed., Wiley-Interscience New York, (1971) p. 604-608.

been studied by several investigators (4,66,144,154). The unit cell as proposed by Daubeny et al. is triclinic with dimensions;

a = 4.48 Å	$\alpha = 99.5^{o}$
b = 5.58 Å	$\beta = 118.4^{o}$
c = 10.75 Å	$\gamma = 112^{o}$

One chemical repeat unit is contained in each cell with the molecules arranged in a nearly planar extended chain conformation. The densities of amorphous polymer and the theoretical density for 100 percent crystalline PET as reported by Daubeny et al. are 1.335 and 1.455 g/cm^3 respectively.

Recently, Fakirov et al. (30) redetermined the unit cell and reported values:

a = 4.48 Å	$\alpha = 99.5^{o}$
b = 5.58 Å	$\beta = 118.4^{o}$
c = 10.75 Å	$\gamma = 11.2^{o}$

The calculated crystalline density based on the proposed new unit cell is 1.515 g/cm^3, four percent higher than the value reported by Daubeny and coworkers. The discrepancy in reported values renders all crystallinity calculations based on density measurements somewhat uncertain. The reported c-axis value of 10.75 Å is in good agreement with the calculated value of 10.9 Å based on a fully extended planar chain.

d. Typical Properties of PET Films

Chemical Properties. Biaxially oriented and annealed PET films are highly resistant to most mineral acids and organic solvents. PET is readily attacked by amines, especially alkyl amines (1). The polymer is soluble in only a few solvents, these include trifluoroacetic acid, dichloroacetic acid, ortho-chlorophenol and a mixture of phenol and trichlorophenol (75).

Physical Properties. The glass transition temperature for amorphous PET is reported to be about 70°C (70,79). The effect of drawing on T_g has been studied by Ito and Hatakeyama (60). For films drawn at 65°C, T_g was observed to decrease to a minimum value at a draw ratio of 1.5, then increase to a maximum value at a draw ratio of 2.0. T_g was found to decrease for draw ratios greater than 2.0. Ito and Hatakeyama suggested that the observed behavior of the glass transition is determined by local oscillations in the amorphous regions.

The melting point (T_m) of crystalline PET is about 264°C. The high melting point is attributed to the rigidity of the aromatic moiety in the chain backbone (23).

The tensile strength of highly oriented PET film ranges from 17,000 to 25,000 psi (49). A valuable characteristic of PET films is their electrical properties; thin PET films are good insulators. Reddish (107) studied the dependence

of dielectric constant and loss factor on temperature and frequency.

B. PET FILMS: CRYSTALLIZATION, MORPHOLOGY AND DEFORMATION BEHAVIOR

a. Quenched PET Films

Heat Transfer Phenomena. Sifleet, Dinos and Collier (125) studied the influence of cooling rate on the morphological distribution in a crystallizing polymer, a chlorinated polyether [3,3'-bis (chloromethyl) oxycyclobutane] during quenching. Unsteady state temperature profiles were obtained by solving the one-dimensional heat conduction equation for an isotropic solid with a heat generation term included to account for the heat produced by crystallization. Such an equation is of the form

$$\partial T / \partial t = \alpha \, \partial^2 T / \partial x^2 + g / \rho \, C_p \qquad \text{(II-1)}$$

where T represents temperature, t, time, x, distance, g is a volumetric heat generation rate and ρ, α and Cp represent density, thermal diffusivity and heat capacity respectively. The boundary condition for the polymer surfaces in contact with air were described by

$$dT / dx_S = h / k \, (T_a - T_s) \qquad \text{(II-2)}$$

where h is the heat transfer coefficient, k is thermal

conductivity , T_a represents the ambient temperature and T_s the temperature at the surface of the polymer.

All physical properties of the polymer were assumed to be constant. Sifleet et al. used an Avrami type analysis to calculate crystallization rates. The effects of different quench temperatures, heat transfer coefficients and sample thicknesses on relative crystallinity were investigated. Polymer samples were heated well above the melting point and then one surface was rapidly quenched in a water bath while the opposite surface was kept insulated. Although Sifleet et al. were unable to maintain a uniform slab temperature, they did demonstrate that crystallization significantly slowed the rate at which the polymer cooled.

Sifleet and coworkers also investigated the possibility of a crystallinity profile developing within the slab. Rapid surface cooling resulted in a lower degree of crystallinity at the slab surface than in the interior. The overall degree of crystallinity was found to be sensitive to quench temperature.

Several investigators (12,46,90,96,100) have applied similar heat transfer analyses to polymer films undergoing simultaneous cooling and crystallization. Pollard and Perkins (100) studied heat transfer in a crystallizing polymer extruded onto multiple chill-rolls. The modified form of the Avrami equation was used to predict through the thickness temperature and crystallinity profiles in a

polyethylene sheet. They included an empirical expression to relate the relative degree of crystallinity of the sheet to polymer temperature;

$$x_c = X_c / [A \exp \{ B / (T - C) \}] \qquad \text{(II-3)}$$

where A, B and C are constants, T is temperature and x_c and X_c represent the final crystalline fraction and the maximum crystalline fraction in the film respectively.

Pollard and Perkins also investigated the difference between using constant physical properties in the heat transfer analyses with including correlations for the dependence of physical properties on temperature and crystallinity. The predicted temperature profiles assuming constant physical properties were found to be significantly different from those where variable properties were included in the analysis.

More recently, Muzzy et al. (90) have developed a general phenomenological model to predict transient temperature and crystallinity profiles in PET films during cooling and solidification. Actual processing conditions were approximated by suddenly exposing hot polymeric slabs of finite thicknesses to an isothermal cooling environment. The resultant morphology through the film cross section was predicted by using a volumetric growth model for spherulitic crystal growth from heterogeneous nuclei.

Muzzy et al. considered only the simplified case of one

dimensional transient heat conduction under quiescent conditions. Under such conditions the heat transfer model can be described by

$$\partial T / \partial t = \partial^2 T / \partial x^2 + (\rho_c Hc / \rho C_p) \, dX/dt \qquad (II-4)$$

where X is a measure of the instantaneous degree of crystallinity, ρ_c is the density of the crystalline phase and H_c is the latent heat of crystallization. The density, ρ, heat capacity, C_p, and thermal diffusivity, a, were assumed to be functions of X, at any point within the slab.

Transient temperature profiles were obtained by solving Equation II-3 using the Crank-Nicolson finite difference technique (20). Muzzy et al. used kinetic data and average spherulite diameters obtained from Differential Scanning Calorimetry (DSC) measurements and optical microscopy respectively in the model to predict the morphology at any position in the cross sections of the slabs. They observed that for quenching below 100°C, the growth rate of spherulites was negligible. Furthermore the final degree of crystallinity was found to be strongly dependent on quench temperature and that despite rapid cooling the model predicts that some isolated spherulites may form in quenched films.

Heat transfer phenomena associated with the drawing process has received less attention, probably because of the inherent complexity of the process. Both Pai and Hyman (96)

and Brazinsky and Davis (12) studied heat transfer phenomena involving PET fibers or filaments drawn over heated rolls. Brazinsky and Davis calculated both lateral and axial temperature profiles for thin PET tapes travelling alternately over heated rolls and through an air space. The entire drawing assembly being enclosed in an oven. The temperature profiles in the tapes were determined by solving a two dimensional steady state heat transfer equation of the form

$$\rho C_p V_z [\partial T / \partial t] = k [\partial^2 T / \partial y^2] \qquad \text{(II-5)}$$

where y and z represent lateral and axial tape positions respectively and V_z is the tape velocity.

The effect of crystallization on film temperature was neglected, but radiant and convective heat transfer modes were investigated. The predicted temperature profile across the tape was found not to be absolutely flat and the temperatures of the tape surfaces were observed to rapidly equalize whenever the tape travelled through an air space.

Structure Studies. Investigations of several glassy, so-called amorphous polymers have revealed that these materials are heterogeneous on a microscopic level (13,82). Quenched PET film is believed to be isotropic; however, several researchers have suggested that it may possess some low degree of paracrystalline order (39,108,111,124). Siegmann and Turi (124) studied the effects of structural

changes in glassy PET on crystallization, melting and mechanical properties. In their investigation, thin glassy PET films were quenched from the melt, annealed below the glass transition temperature and subsequently thermally crystallized or drawn. DSC thermograms of quenched films showed a strong dependence of crystallization temperature on quench temperature and film thickness. Characterization of the quenched films by classical techniques such as x-ray diffraction and density indicated all films were similarly "amorphous". Yeh and Geil (155,156) reported the existence of nodular structures in PET cast sheet (quenched film). These nodular or ball-like structures ranged from 45 Å to 100 Å with an average size of 75 Å. On annealing below T_g, the ball-like structures were observed to move, aggregate and align. Annealing at 154°C resulted in the growth of well defined spherulites, the size of which was found to depend on the thermal history of the film.

Renninger and Uhlmann (108) recently conducted extensive small-angle x-ray diffraction (SAXS) studies of amorphous PET films. Based on these studies they characterized the bulk structure of glassy PET films as being that of a random amorphous polymer containing a small quantity of heterogeneities, ranging in size from 100 Å to 2000 Å superimposed on thermal density fluctuations frozen in at the glass transition. The larger structures they regarded as being contaminants or processing aids; however,

they speculated that some of the heterogeneities on the order of a few hundred Angstroms may be crystallites that formed on cooling from the melt, especially since these structures were found to be present in the bulk of the film rather than on the surface.

b. Crystallization Behavior of PET

Quiescent Crystallization. The crystallization characteristics of PET are still not well understood despite numerous studies. Under quiescent conditions PET will crystallize to form spherulites (63,65). Early investigations into the crystallization kinetics of PET were conducted by Keller et al. (63,64,65), Morgan (89), Cobbs and Burton (19), Zachmann and Stuart (157) and Hartley et al. (47). The researchers observed that the crystallization kinetics depended on a number of factors besides temperature; there was a significant influence of such factors as molecular weight, molecular weight distribution, mechanical stress, impurities and processing conditions. Sheldon (120) investigated the influence of extrusion conditions on subsequent thermal crystallization behavior. Keller (63) reported that the diameter of spherulites increased with crystallization temperature. More recently Van Antwerpen and Van Krevelen (145) studied the effects of temperature, molecular weight and additives on the growth rate and morphology of spherulitic crystallization. Kinetics

studies of the isothermal crystallization of unoriented PET have shown that the maximum spherulite growth rate occurs at 155°C for crystallization from the melt and 190°C from the glassy state (8,127). Spherulite size has a direct influence on mechanical properties, in general, impact strength, elongation to break and yield stress decrease as spherulite size increases (129).

Most of the investigations into the mechanism of crystallization in polymers have been directed at isothermal crystallization in the absence of external stress. Most polymer processing operations, including the stretching of a quenched amorphous PET film, involve crystallization under nonisothermal conditions and under the influence of an applied stress.

Stress-Induced Crystallization. Deformation of polymer chains to a more extended conformation can result in an enhanced rate of nucleation and crystallization. The deformation of polymer molecules in a purely extensional flow such as the spinning of a fiber or the drawing of a film would therefore be expected to increase the rate of formation and the subsequent growth of crystals. Several studies have shown that crystallization rates for oriented materials are several orders of magnitude higher than those for unoriented specimens (127).

Crystal nuclei in polymers are believed to originate as the result of thermal fluctuations. The entropy of a

molecule deformed to an extended conformation is lower than that of an unextended molecule. Thus a deformed polymer molecule would be expected to have a greater degree of supercooling at any particular temperature and therefore a greater driving force toward both nucleation and crystallization. The drawing of PET fibers or films produces a deformation of polymer chains and thereby causes nucleation and crystallization to occur at temperatures where the rate of thermal crystallization is otherwise negligible (127).

Rabesiaka and Kovacs (106) in their studies of polyethylene presented evidence that even residual stress caused by preorientation could enhance nucleation through memory effects. They also suggested the existence of "quasi-indestructable" nuclei which could exist in the melt. Frolova et al. (37) studied the effect of deformation on the crystallization kinetics of several polymers including PET.

Early studies on stress-induced crystallization of PET fibers were first carried out by Thompson (140). He observed two distinct deformation regions for amorphous PET fibers drawn above the glass transition temperature. One region occurred at high strain rates and was accompanied by the formation of a high degree of orientation and crystallinity. In this region pronounced necking was observed. The second region was characterized by low deformation stress with little molecular orientation or

crystallization. Spruiell et al. (128) observed similar behavior in their studies of PET tensile bars drawn above T_g. Furthermore stress rather than strain was found to be the critical factor in initiating crystallization during stretching. Orientation has been shown to appreciably alter the crystallization kinetics in PET. Crystallization occurs on the order of milliseconds in oriented materials as compared to several minutes in unoriented specimens (127).

Elsner et al. (27,28) have recently reported results on SAXS studies on the isothermal crystallization of oriented as well as unoriented PET films using synchrotron radiation as the x-ray source. The use of an intense highly focused monochromatic x-ray beam from the synchrotron source allowed them to detect and record minute changes in the SAXS patterns in very short periods of time. Thus they were able to measure crystallization taking place at rapid rates. Both studies show a decrease in the long period spacing with increased crystallization time. Elsner et al. believe that this discrepancy can be explained in terms of a corrugated crystalline superstructure present in the early stages of crystallization which then diminishes as crystallization proceeds. They also suggested that the decrease may be the result of an increase in the lateral growth of the crystals or in their perfection or in a combination of both.

A number of structural parameters are required to adequately describe the morphology of oriented

semicrystalline polymeric materials, these include; the size and orientation distribution of the crystallites, the orientation of the noncrystalline regions, the existence and nature of any superstructures such as spherulites or fibrillar structures and variations in these quantities within the film, especially through the thickness. The determination of the orientation distributions of both the crystalline and noncrystalline regions is important because they control the mechanical and physical properties of the film.

In general, it is known that the morphology of semicrystalline polymers crystallized under stress changes as the level of stress changes. In the absence of external stress PET crystallizes with a spherulitic superstructure, however as the level of stress increases the spherulitic superstructure becomes increasingly deformed (73).

Birefringence, infrared dichroism and x-ray studies by Dulmage and Geddes (24) of annealed uniaxially stretched PET films showed that the stretching caused the alignment of chain molecules parallel to the stretch direction and tended to orient the planes of the molecules parallel to the plane of the film. Upon annealing, they observed a pronounced tilting of the c-axes of the crystallites, producing a distribution of preferred c-axis orientations. These ranged from almost perpendicular to the stretch direction at low elongations to approximately parallel to the direction of

stretching at high elongations. Heffelfinger and Burton (50) observed a similar tilting of the c-axes in uniaxially drawn and annealed films. In addition they reported x-ray results showing that a small fraction of the crystallites remained oriented perpendicular to the stretch direction suggesting a bimodal orientation of crystallites.

X-ray studies by Heffelfinger and Schmidt (53) showed that the uniaxial stretching of amorphous PET film resulted in the development of orientation in the stretch direction accompanied by partial crystallization. The c-axes of the crystalline regions tended to become aligned parallel to the stretch direction with a portion of the (100) crystallographic planes oriented parallel to the film surface. Subsequent stretching in the transverse direction was shown to result in an increase in the parallelism of the (100) planes to the film surface. SAXS patterns revealed an increase in the average crystallite length but little change in the size of the noncrystalline regions. Heffelfinger and Schmidt suggested that the structural changes occurring during sretching in the transverse direction are associated with a redistribution of structure produced as a consequence of uniaxial stretching. Evidence for the existence of a strained amorphous structure in uniaxially oriented films was proposed on the basis of relaxation studies.

Several models have been proposed to explain the development of molecular orientation and crystalline

superstructure of drawn PET (11,130,153). Statton and Goddard (130) proposed a microplatlet model for uniaxially oriented PET films. Their model consists of parallel platelets stacked in successive rows with the individual crystallites in each layer arranged in a chessboard array. Bonart (11) also suggested a stacked platelet model consisting of crystalline and noncrystalline platelet shaped domains oriented essentially parallel to the film surface. Some support for such micro-platelet morphologies has come from SAXS studies by Heffelfinger and Lippert (51). Diffraction patterns of oriented films indicated that a range of morphological domains were present including a layered platelet superstructure, each with an average size of 2000 Å X 10,000 Å situated parallel to the film surface.

Yeh and Geil (155,156) reported the existence of a nodular morphology in oriented PET film. The nodular superstructure is believed to be the result of the rotation, alignment and increase in the perfection of paracrystalline nodular or ball-like structures originally present in glassy films. Uniaxial stretching caused these ball-like structures to align into staggered rows with a pronounced tilt to the stretch direction. Yeh and Geil did not observe any significant change in the size of these structures during stretching, however the c-axes of the unit cells were observed to align in the stretch direction. Subsequent stretching in the transverse direction produced block-like

domains on the order of 1000 Å oriented approximately 45 degrees from the transverse direction.

Koenig and Cornell (71,72) conducted polarized infrared spectroscopic studies on the effect of temperature and draw ratio on the orientation and structural changes caused by uniaxial and biaxial drawing of PET film. Uniaxially drawn films were characterized as having highly oriented crystalline regions with almost randomly oriented noncrystalline domains. A comparison of simultaneously biaxially stretched and sequentially stretched films showed that the films subjected to simultaneous drawing had nearly balanced properties whereas the sequentially stretched films were observed to have a preferential orientation of the crystalline regions in the transverse direction. The sequentially stretched films were found to have higher degrees of crystallinity than those drawn simultaneously.

Klement and Geil (67,68) investigated the morphology and deformation behavior of uniaxially and biaxially oriented PET films. In addition to observing the nodular morphology seen by Yeh and Geil (155), they observed a supernodule structure of the order 250 Å to 500 Å. Investigations of both thick and thin films revealed similar morphologies after drawing. Annealing of drawn thick films above 180^{o}C resulted in the formation of a fibrillar structure arranged perpendicular to the stretch direction in

uniaxially drawn films and randomly oriented in biaxially stretched films.

Most studies of the morphology of PET films and fibers have dealt almost exclusively with the characterization of superstructure in the final product, that is after annealing. However, there has been relatively little investigation of the intermediate state produced as a result of the uniaxial deformation of the amorphous film or fiber. The most noteworthy attempt to characterize this intermediate state is that of Casey (15) who studied the crystalline superstructure in unannealed uniaxially drawn films by x-ray diffraction. Casey showed that a small c-axis crystalline tilt exists in unannealed uniaxially drawn films but in a different direction from that observed by other investigators (24). He proposed a microfibrillar model to explain the morphological changes occurring in the film during stretching. Casey also speculated on the existence of transverse crystalline links between adjacent fibrils, this was based on an observed increase in modulus with increasing degree of orientation in the stretch direction.

The concept that the morphology of oriented PET film consists of layers situated parallel to the film surface has gained some support from etching studies (1,5,25,88). Adams (1) used n-propylamine to selectively etch both the crystalline and noncrystalline regions in uniaxially drawn

unannealed and annealed PET films. The films studied were drawn in the 90°C to 100°C range at elongation rates of 10,000 percent per minute. Scanning electron photomicrographs of the etched films revealed a macrostructure consisting of long network elements of about 1,500 A. These structures were observed in oriented as well as in unoriented films. Adams also found that the long direction of these elements was aligned perpendicular to the stretch direction and that the size of these elements decreased as the degree of orientation in the film increased.

Early studies by Baker (5) revealed the macrostructure of oriented films to consist of micron-size platelets which could be cleaved off using an amine etchant. The size of the platelets was found to decrease from the film surface inward toward the center. Uniaxially oriented films were observed to have evenly spaced parallel lines etched into both film surfaces in the stretch direction. At long etch times delamination of the films was observed.

Small-angle light scattering (SALS) has been used to characterize the nature of the crystalline morphology produced as a result of stress-induced crystallization in PET film (73,76,86,87,134,139,141). SALS studies by Stein (134) of film stretched at 80°C and at constant strain rate without susequent annealing revealed a variety of morphologies depending on the degree of elongation imposed

on the films. Stein concluded that the crystals composing the superstructure did not originate from rod-like "shishes" elongated in the direction of stretching but rather from structures oriented perpendicular to the stretch direction. Recently, Misra and Stein (86) presented results of SALS studies on the formation of crystalline morphologies in uniaxially drawn PET film at temperatures above and below the glass transition. For films drawn above T_g the superstructure at low elongations was found to consist of rod-like structures which did not significantly contribute to the overall crystallinity and had their major axes oriented perpendicular to the stretch direction while at higher elongations these structures became more "spherulitic" in appearance. At intermediate elongations a sheaf-like structure was observed. SALS patterns and optical photomicrographs of the films stretched to high elongations revealed the formation of a rod-like morphology in the stretch direction, indicative of a fibrillar superstructure.

Recently Terada et al. (139) and Matsuo and coworkers (76) used SALS to investigate the deformation behavior and stress-induced crystallization in uniaxially oriented PET films. Eight lobe H_v SALS patterns from amorphous PET films drawn to various draw ratios at 95°C were observed. The patterns consisted of four broad lobes at small azimuthal angles and four sharp streaks at large angles. These H_v

"butterfly" type pattterns are attributed to a row-nucleated sheaf-like structure whose rows are preferentially oriented at a particular angle to the stretch direction.

c. Drawing Behavior

The main purpose of drawing a polymer fiber or film is to increase the degree of molecular orientation in the material and thereby improve the mechanical properties of the finished product, particularly tensile strength. The mechanical properties depend on many variables including crystallinity, orientation, chemical composition and morphology all of which are related to drawing conditions. The ultimate goal of the drawing process is to achieve a perfect highly preferential degree of orientation, thus imparting selective changes in the structure and properties of the material. However perfect orientation is never achieved, rather a distribution of orientations results.

The uniaxial drawing of a polymer film can be considered as a non-uniform, non-isothermal elongational deformation. Studies of the tensile deformation behavior of PET films show a marked transition from cold drawing accompanied by necking to homogeneous deformation occurs near the glass transition (56,97,110,128). Rietsch et al. (110) found that the homogeneous deformation of PET at temperatures above 80^{o}C is consistent with the theory of a molecular network in a rubbery state. The approximation is valid only for low extensions, typically below a draw ratio

of 1.7. Several investigators (56,128) have observed that a critical temperature and strain rate region exists where PET can be drawn without producing orientation. Hinrichsen and coworkers (56) studied nonorientation drawing of PET films. Hinrichsen et al. found that within the temperature interval between 80°C and 100°C forces required to draw a film are very low and are strongly dependent on strain rate. At temperatures between 95°C and 100°C amorphous PET sheets were drawn to produce films without any orientation or crystallinity.

Polarized fluorescence has been used to study the distribution of orientation within the noncrystalline regions of PET (81,91,92). The technique is based on the premise that fluorescent probe molecules are too bulky to be accomodated in the crystalline regions of the polymer. Combined with x-ray diffraction and birefringence measurements, polarized fluorescence has been utilized as a means of separating the orientation in the noncrystalline regions from the overall degree of orientation. Since PET has low to moderate levels of crystallinity it is believed that the orientation of the noncrystalline regions has a strong influence on overall properties.

Infrared and nuclear magnetic resonance spectroscopy to study the rotational conformation of the ethylene glycol portion of the PET repeat unit in the polymer chain (22,59,62). Spectroscopic studies indicated that the

crystalline regions are composed entirely of repeat units in the trans conformation while the noncrystalline regions consisted of units having both trans and guache conformations. Furthermore, conversion of gauche to trans conformations has been used to explore the structural changes occurring during stress-induced crystallization (22).

Several studies have focused on biaxially oriented films. Yokouchi et al. (157) studied the effect of strain rate on the mechanical properties of constrained-uniaxially and simultaneous biaxially drawn PET films. Blumentritt (10) investigated the influence of film thickness on dimensional stability and mechanical properties of biaxially oriented films. Thin films were observed to be more optically and dimensionally anisotropic than thick films a result of a higher degree of in-plane orientation in the thin samples.

C. TECHNIQUES FOR CHARACTERIZING INHOMOGENEITY IN POLYMER FILMS

Determination of the optical properties of polymers is a major part in the overall characterization of these materials. To be of any commercial value, most polymer films and fibers must be drawn. Drawing serves to produce molecular orientation and in turn improves overall properties. The level and distribution of orientation

present in a finished product can be correlated to processing conditions, this information may then be used to determine a optimum range of conditions.

Optical anisotropy can best be described in terms of wave characteristics of light. Consider light rays passing through a optically anisotropic medium. One of the light rays will pass through the medium with a velocity which is invariant with direction. This ray is called the ordinary ray (O-ray) and has a spherical wave surface. The O-ray is plane polarized and it vibrates in a direction perpendicular to the plane defined by the O-ray and the optic axis of the medium as shown in Figure II-5. The second ray is known as the extraordinary ray (E-ray) and its velocity unlike that of the O-ray varies with direction. Its wave surface is elliptic. The E-ray vibrates in a direction parallel to the plane defined by the optic axis of the medium and by the direction of propagation of the E-ray. The relationship between the azimuths of vibration of the O-ray and E-ray and the optic axis of the material is also illustrated in Figure II-5. In the special case where the O-ray and E-ray cannot be distinguished, the material appears to be optically isotropic. This phenomenon occurs because incident light which travels parallel to the optic axis must vibrate only in directions perpendicular to the optic axis.

Light passing through an optically anisotropic solid will be resolved into two plane polarized waves, the

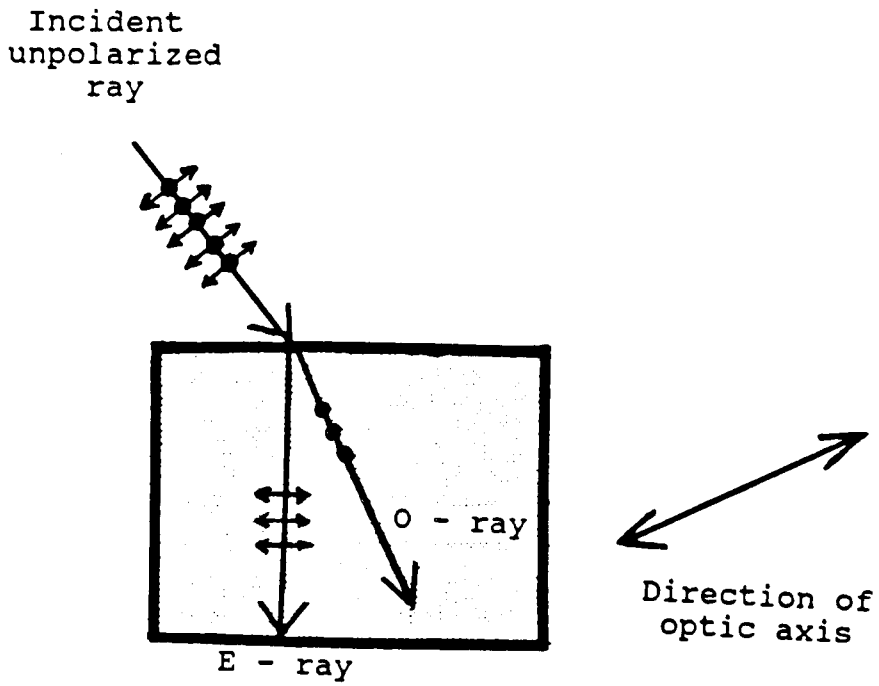


Figure II-5. Azimuths of vibration within a birefringent medium. The optic axis of the medium is parallel to the plane of the page and oriented in the direction shown.

Source: Slayter, E.M., "Optical Methods in Biology", Wiley-Interscience, New York (1970), p. 103.

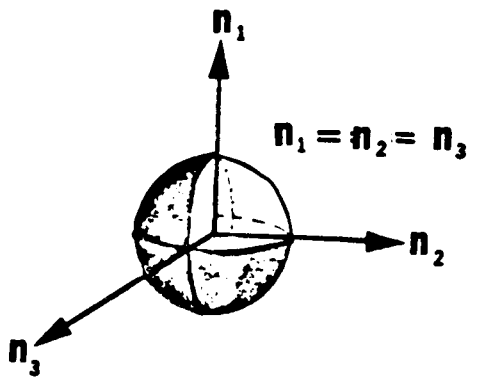
propagation directions of the wavefronts being mutually perpendicular. The velocities of the two waves will be different as will the optical path lengths, thus, one wave will be retarded with respect to the other. The phase angle between the transmitted O-ray and E-ray is determined by the extent of retardation between the rays as they travel through the medium. Retardation is the phase difference in path length between positions of equal phase of the polarized beams passing through the material. The optical retardation of a specimen is defined by

$$\Gamma \equiv (n_e - n_o) t \qquad \text{(II-6)}$$

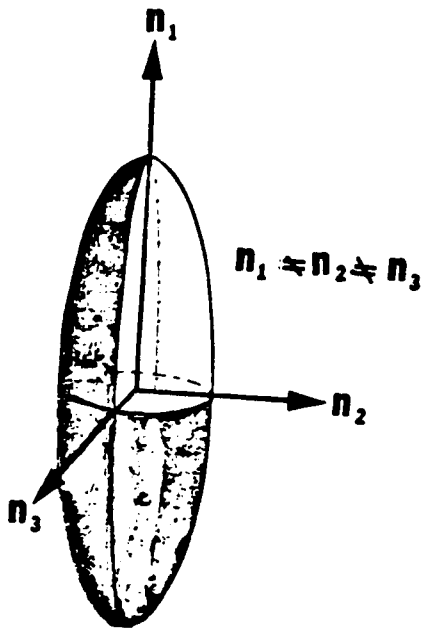
where e and o refer to the oridanary and extraordinary rays passing through the medium, respectively and t is the distance the light rays have travelled.

Optical retardation is a function of the material, thickness and specific state of orientation. These materials are characterized by at least two different refractive indices and are thus referred to as being birefringent.

The variation in refractive index with direction may be represented graphically in terms of a figure known as an index ellipsoid. In the case of optically isotropic materials, refractive index is invariant with direction therefore the figure is spherical as shown in Figure II-6a, whereas optically anisotropic media can be represented by a



(a)



(b)

Figure II-6. Refractive index ellipsoids: (a) optically isotropic medium and (b) optically anisotropic medium.

Source: Slayter, E.M., "Optical Methods in Biology", Wiley-Interscience, New York (1970) p.

figure of the type shown in Figure II-6b. Index ellipsoids do not have any physical meaning but are simply a convenient means of representing variations in refractive index with direction. For a fiber, the index ellipsoid is defined as an ellipsoid of rotation such that one axis has length proportional to n_e and is oriented parallel to the optic axis of the fiber and the other two axes are of equal length and proportional to n_o. The fiber and the central portion of its index ellipsoid are illustrated in Figure II-7. Central portions of index ellipsoids for a film are shown in Figure II-8.

In a birefringent material there exists one direction, called the optic axis in which the two components of the transmitted light cannot be distinguished. A material viewed along this direction will appear to be optically isotropic. Optic axes may be helical, linear, radial or tangential. In biaxial materials, all three axes of the index ellipsoid have different lengths and are inclined with respect to the optic axes.

Birefringent materials can be characterized by observing the interference of light beams which have traversed the material in a direction perpendicular to the optic axis. Complete characterization implies determination of the shape and orientation of the index ellipsoid.

Polymers can be catagorized as belonging to either of two groups of optical materials, the first group is

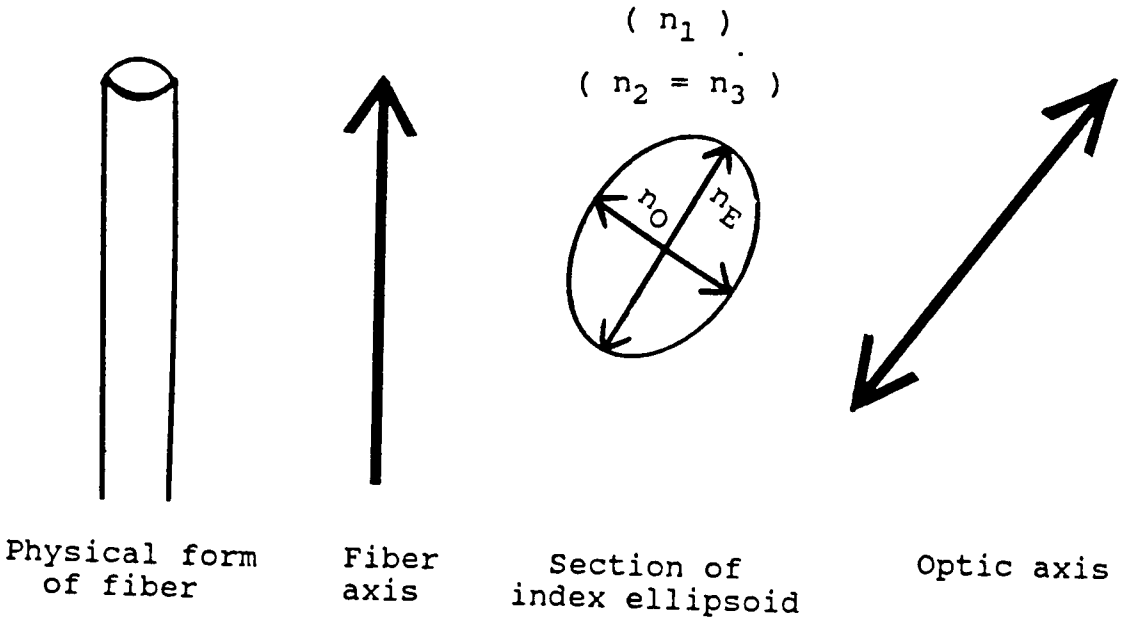


Figure II-7. Illustration of a fiber and the central section of its refractive index ellipsoid. The optic axis is inclined at 30 degrees to the fiber axis.

Source: Slayter, E.M., "Optical Methods in Biology", Wiley-Interscience, New York (1970), p. 339.

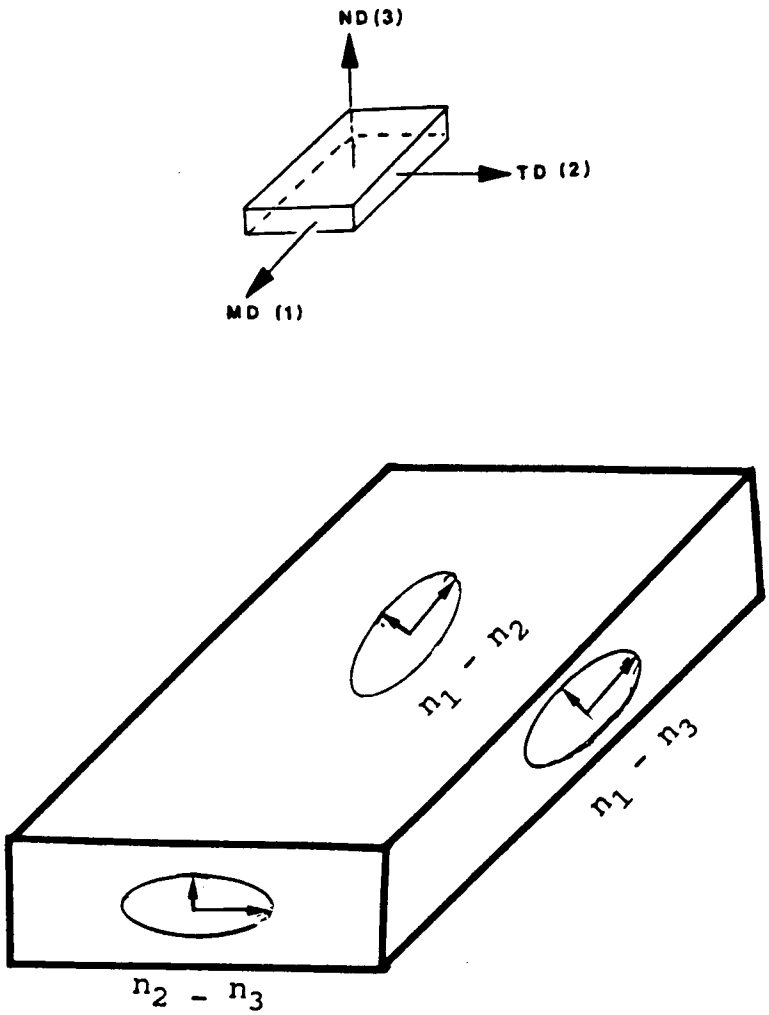


Figure II-8. Film strip showing the projections of the refractive index ellipsoid on the three sides of a polymer film.

Source: Iyer, K.R.K., S. Sreenivasan and N.B. Patil, Textile Res. J., 53, 442 (1983).

isotropic materials, the second being anisotropic materials. Unoriented amorphous polymers belong to the isotropic group. The optically anisotropic group includes semicrystalline polymers as well as strained amorphous materials. Transparent anisotropic polymeric materials can be conveniently studied with the polarizing microscope.

a. Optical Microscopy

Polarized Light Studies. Optical anisotropy is easily observed by using polarized light. The polarizing microscope can be used to locate the optic axes of materials and to determine the shape and orientation of index ellipsoids. A generalized schematic of the polarizing microscope is shown in Figure II-9. A typical polarizing microscope consists of a conventional compound light microscope fitted with two polars, usually sheets of Polaroid film. One polar called the polarizer is located below the condenser and the other polar referred to as the analyzer is positioned above the objective. The function of the polarizer and analyzer is illustrated in Figure II-10.

In practice, the polarizer is fixed and the analyzer is rotated until its privileged direction is perpendicular to that of the polarizer, in this configuartion the image field will exhibit minimum illumination and any birefringent specimen placed on the rotatable stage will transmit light depending on the orientation of its optic axes with respect

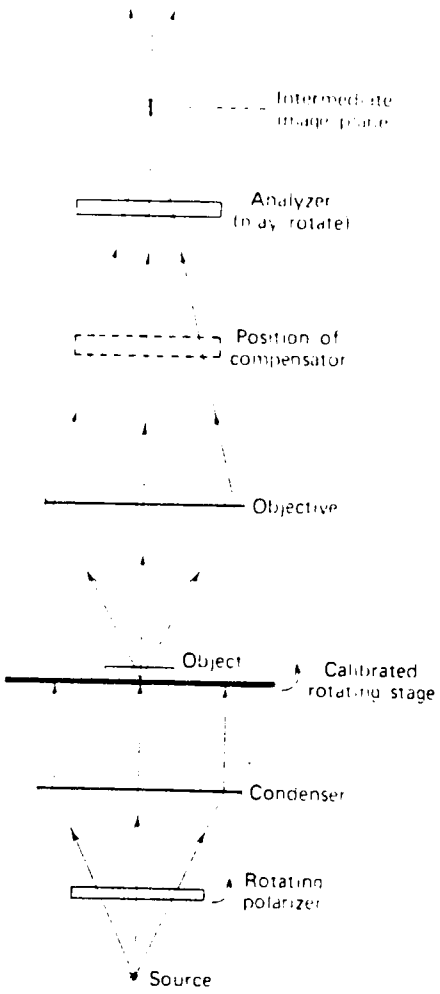


Figure II-9. The polarizing microscope.

Source: Slayter, E.M., "Optical Methods in Biology", Wiley-Interscience, New York (1970), p. 329.

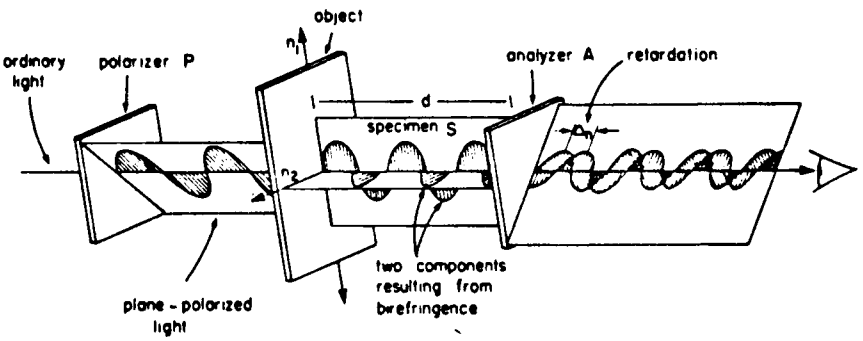


Figure II-10. Function of the polarizer and analyzer.

Source: Rochow, T.G. and E.G. Rochow, "An Introduction to Microscopy by Means of Light, Electrons, X-rays or Ultrasound", Plenum Press, New York (1978), p. 100.

to the microscope axis. In polarized light microscopy, the birefringent material itself resolves the light from the first polarizer into two mutually perpendicular beams; these beams are recombined by the analyzer. The two beams will interfere either constructively or destructively depending on the phase relationship between the two beams. If constructive interfernce occurs, light will be transmitted and the specimen under examination will be seen, if however destructive interference takes place no image is formed. If in addition, a variation in path length is present in a specimen having uniaxial optical symmetry, that is two principal refractive indices of equal value, interference fringes will be formed. Oblique cross sections of oriented polymeric fibers produce fringe patterns when viewed through crossed polarizers.

This phenomenon can be used to study radial variations in structure in fibers produced by high speed spinning. Shimizu et al. (122,123) used polarized light microscopy to investigate structure development in high speed spun PET and Nylon 6 filaments. Fringe patterns of oblique fiber cross sections were semi-elliptical, the foci of the ellipses being located on the fiber axis as shown in Figure II-11. Shimizu et al. observed that for fibers having a homogeneous radial structure the fringe patterns were generally symmetric about the fiber axis (Figure II-11a) while fibers exhibiting radial variations in structure produced



(a) (b) (c)

OBLIQUE CROSS SECTION



(d)

$P\ (\ x\ ,\ x^2 - y^2\ )$

$Q\ (\ x,\ y\ )$

PQ : Optical Path Length
$n\ (\ r\ )$: Local Birefringence $(\ r = x^2 - y^2\ )$
λ : Wavelength
k = 1, 2, 3, . . .

d : Distance Between Fringes in Sample
D : Distance Between Undisplaced Fringes
n : Refractive Index of Fiber
N : Refractive Index of Immersion Oil
$2y$: Thickness of Sample
λ : Wavelength

Figure II-11. Interference fringe patterns in oblique fiber cross sections: (a) fiber having homogeneous radial structure; (b) and (c) fiber exhibiting radial variations and (d) conditions for fringe formation.

Source: Shimizu, J., N. Okui and T. Kikutai, Sen-i-Gakkaishi, 37, T135 (1977).

asymmetric patterns (Figures II-11b and II-11c). The conditions required to produce fringe patterns are shown in Figure II-11d.

Determination of Birefringence. Birefringence is readily obtained by measuring retardation and the thickness of the specimen. The method although straightforward in principle has one practical limitation, that is, the thickness of the specimen must be known. The simplest way to measure birefringence is by means of a microscope and a compensator.

For accurate determination of birefringence, the specimen must be oriented so that its optic axis is exactly perpendicular to the microscope axis. The approximate orientation of the optic axis may be determined by inspection between crossed polars. A optically anisotropic specimen will produce four positions of maximum intensity and correspondingly four of extinction when the specimen is rotated through an angle of 360 degrees between crossed polars. The orientation of the specimen where extinction occurs at all angles coincides with a direction parallel to its optic axis, at this point the specimen appears to be optically isotropic. Characteristic orientations of the optic axes of oriented polymer films can be obtained by observation of sections cut in several different planes. The precise measurement of retardation may be made with the aid of a device known as a compensator.

Compensators. Several types of compensators are available. Two popular types are the wedge compensator and the tilting plate compensator. The Babinet compensator consists of two opposing quartz wedges each having its optic axis within the plane face of the wedge but with the two optic axes being perpendicular. In practice, one wedge is fixed, the other mounted on a movable micrometer. Relative translation of the two wedges is used to produce changes in retardation. A complete description of the compensator and its operation is given in reference (9). The tilting plate compensator is a birefringent plate cut with its optic axis normal to the plate surfaces. The plate may be tilted about an angle with respect to the microscope axis. A common tilting plate compensator utilizing this principle is the Berek compensator (57). The Berek compensator consists of a single 0.1 mm thick calcite plate (9). The amount of retardation imposed by the compensator depends on the angle of tilt as can be seen in Figure II-12. As shown, positions A, B, and C represent minimum, intermediate and maximum degree of retardation, respectively.

Measurement of the optical retardation of incident light perpendicular to the surface of a polymer film provides the difference between the two principal refractive indices in the plane of the film but does not provide any information about the refractive index normal to the surface. Stein (133) developed a method for characterizing

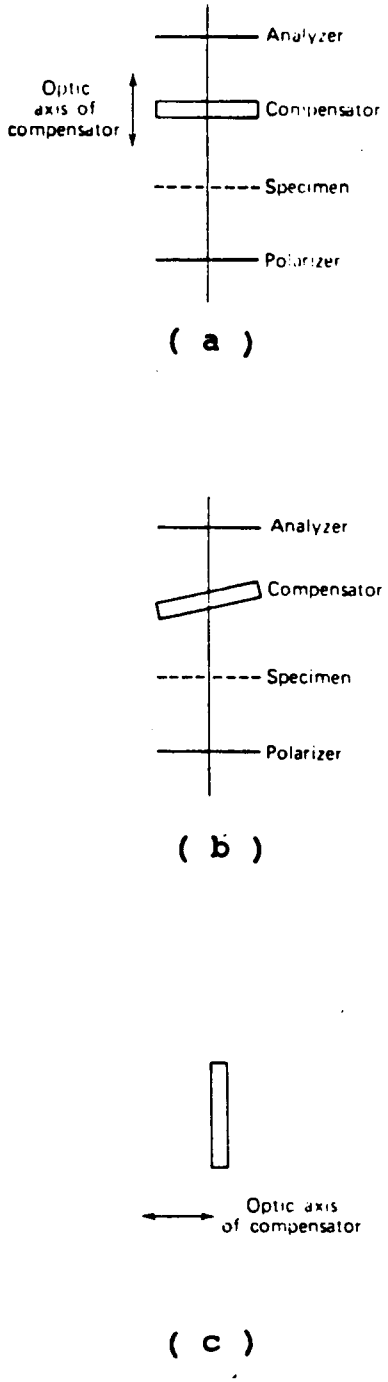


Figure II-12. Tilting plate compensator: (a) Position of minimum compensation (neutral position); (b) intermediate position and (c) position of maximum compensation.

Source: Slayter, E.M., "Optical Methods in Biology", Wiley-Interscience, New York (1970), p. 334.

the optical properties of biaxially oriented films including the ability to obtain out-of-plane birefringences. The technique involves measuring optical retardation as a function of the tilt angle of the film.

Iyer et al. (61) used the compensator method to determine the birefringence of stretched cellulose films. In-plane and out-of-plane birefringences were determined by measuring retardation at normal incidence on thin sections (50--100 μm) cut parallel and perpendicular to the stretch direction using a Berek compensator.

The variation in overall molecular orientation in the thickness direction of thick polymer films and fibers can be determined by measuring birefringence at several points through the cross section. Roylance and Roylance (114) studied the orientation distribution in the thickness direction of rolled polypropylene sheets. Wust and Bogue (152,153) used the compensator technique to obtain birefringence profiles for amorphous slabs quenched in different cooling media. Quenched slabs were sectioned and optical retardation measured at various points through the thickness.

For most purposes a knowledge of birefringence is adequate to describe the state of orientation in a material. However, several different combinations of refractive index can yield the same birefringence value. Refractive index can be measured by exploiting the optical phenonmena of

refraction and interference. The principal refractive indices of a material can be measured by a variety of techniques which differ both in their range of applicability and in sensitivity.

The general principles and applications of these subjects can be found in numerous texts and articles (42,80,113,147,150). The desription presented in the following section will be limited to the application of these techniques to polymer fibers and films.

b. Refractometry

Basic Principles. The change in direction of a ray of light when it passes obliquely from one medium into another of different optical density is called refraction. Refractive index is defined as the ratio of the velocity of light in vacuum c, to that in the medium v, that is;

$$n = c / v \qquad \text{(II-7)}$$

The law of refraction, also known as Snell's Law is given by

$$\frac{\sin \theta_i}{\sin \theta_r} = \frac{n_2}{n_1} \qquad \text{(II-8)}$$

where n_1 and n_2 are the refractive indices of the two media and where the angles between the incident and refracted rays and the normal to the boundary between the two media are

designated as the angle of incidence θ_i, and the angle of refraction θ_r, respectively as shown in Figure II-13.

The phenomenon of total internal reflection is a consequence of the behavior of light as described by Snell's Law. As the angle of incidence is increased, the angle of refraction will correspondingly increase. If the angle of incidence is increased so that the angle of refraction equals 90 degrees, the beam of light will no longer travel from the first medium to the second, but will pass through the first medium to the boundary surface separating the two media and then proceed to travel along this surface. This ray would make an angle of 90 degrees with the perpendicular to the surface, such a ray is called the critical ray and the corresponding angle is referred to as the critical angle θc. If a ray has an angle of incidence less than Oc it will pass through the second medium, if however the ray has an angle of incidence greater than θc, it will be totally reflected at the boundary. Total reflection can only occur when light passes from a medium of higher refractive index into a medium of lower refractive index. In the case where light is incident upon an interface between media of different refractive indices the intensity of the incident beam is divided between the reflected and refracted beams.

Most refractometers utilize the critical angle phenomenon to measure refractive index. A cross section of a prism refractometer is illustrated in Figure II-14. A

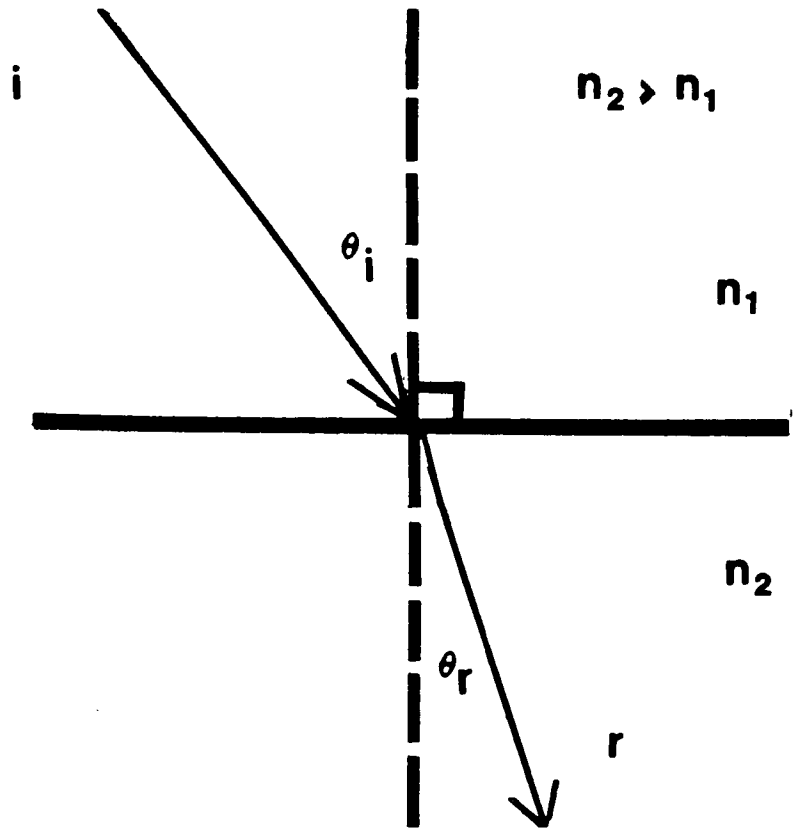


Figure II-13. Phenomenon of refraction.

Source: Slayter, E.M., "Optical Methods in Biology", Wiley-Interscience, New York (1970), p. 6.

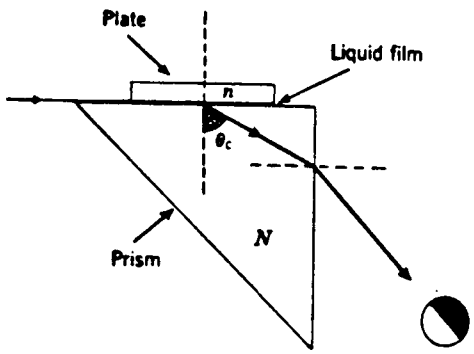


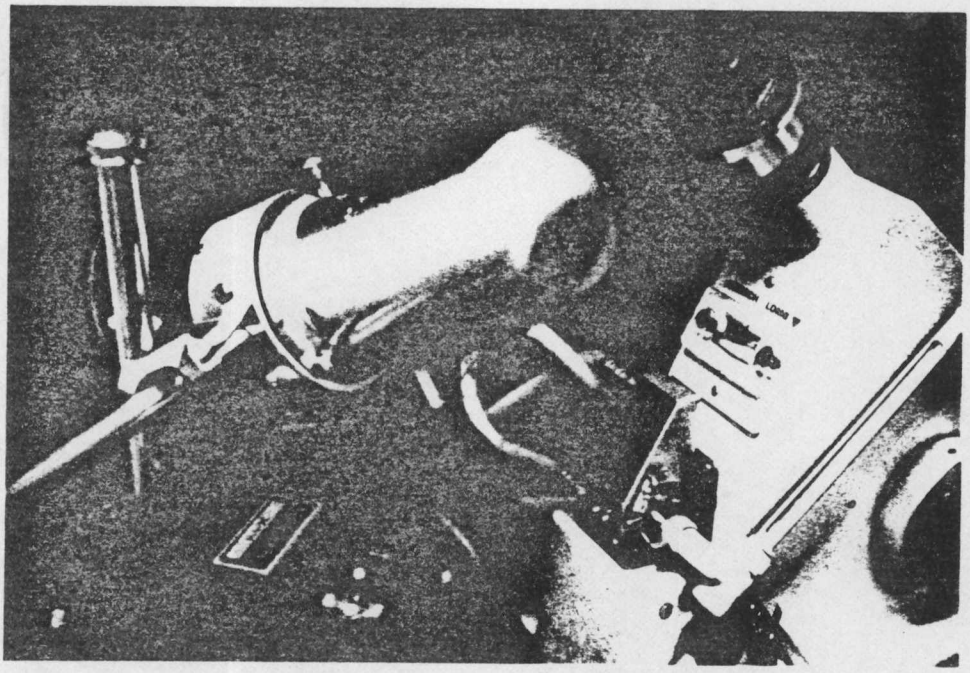
Figure II-14. Diagram of a prism refractometer.

Source: Wahlstrom, E.E., "Optical Crystallography", John Wiley and Sons, New York (1978), p. 147.

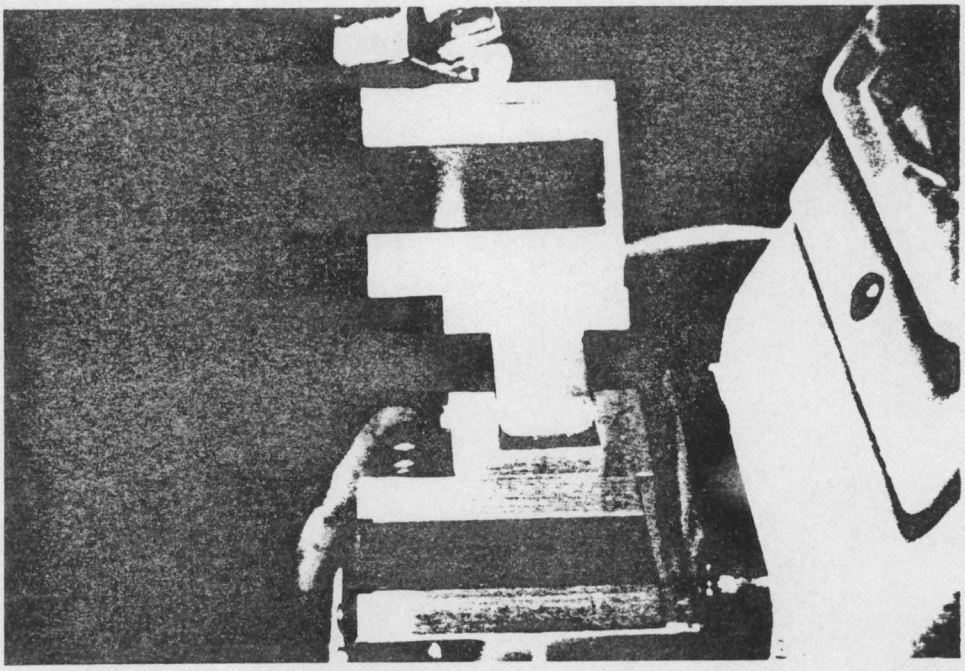
liquid or solid having refractive index n_L is placed on the face of the prism of higher refractive index. In the case of a solid sample, an inert immersion liquid having a refractive index higher than that of the sample is used to exclude any air at the solid-prism interface. All light rays having an angle of refraction less than Θ_c will be partially reflected whereas rays having angles of refraction in excess of Θ_c will be totally reflected. A telescope aligned with the critical ray reveals a divided field, half dark, half bright. The contrast results from the fact that the totally reflected light is more intense than that which is partially refracted. Using a calibrated scale mounted on the instrument, the measured angle Θc directly yields the refractive index of the sample.

Abbe' Refractometer. Refractometers that utilize the phenomenon of the refraction of light to measure refractive index include the Abbe' refractometer. The Abbe' refractometer is one of the most widely used refractometers. Its popularity can be attributed to its low cost, simple design and ease of operation. The instrument and its working components are shown in Figure II-15.

Light from the illumination source is reflected from a mirror prior to passing into the illuminating prism P_i. The upper surface of P_i is rough ground, this rough surface acts as the source of an infinite number of rays which pass through the substance in all directions. Upon emerging from



(a)



(b)

Figure II-15. The Abbe' refractometer and its essential components: (a) refractometer and sodium vapor lamp and (b) close-up of prisms.

the substance the rays strike the polished surface of the refracting prism P_r sometimes called the measuring prism and are refracted. The refractometer is equipped with a moveable telescope and a calibrated scale. The index of refraction of the substance is read directly from the scale after the telescope has heen positioned over the central portion of the refracted light. Cross-hairs inscribed on the eyepiece aid in the alignment of the line of demarcation. The critical ray forms the border between the light (upper) and dark (lower) portions of the field when viewed through the telescope as previously described. The loss in intensity of the incident beam determines whether or not an image can be seen. Most refractometers typically use white light as the illumination source. When white light is used a colored indistinct boundary between the upper and lower fields is produced. The boundary is a result of the difference in refractive indices for light of different wavelengths, a consequence of the dispersion of light at the liquid--prism interface. Dispersion is defined as the variation of refractive index with wavelength. To compensate for this effect, two prisms, called Amici prisms are installed in series in front of the objective of the telescope as shown in Figure II-16. To obtain greater accuracy in measurement, a monochromatic light source, usually a sodium vapor lamp is used in place of the conventional white light source.

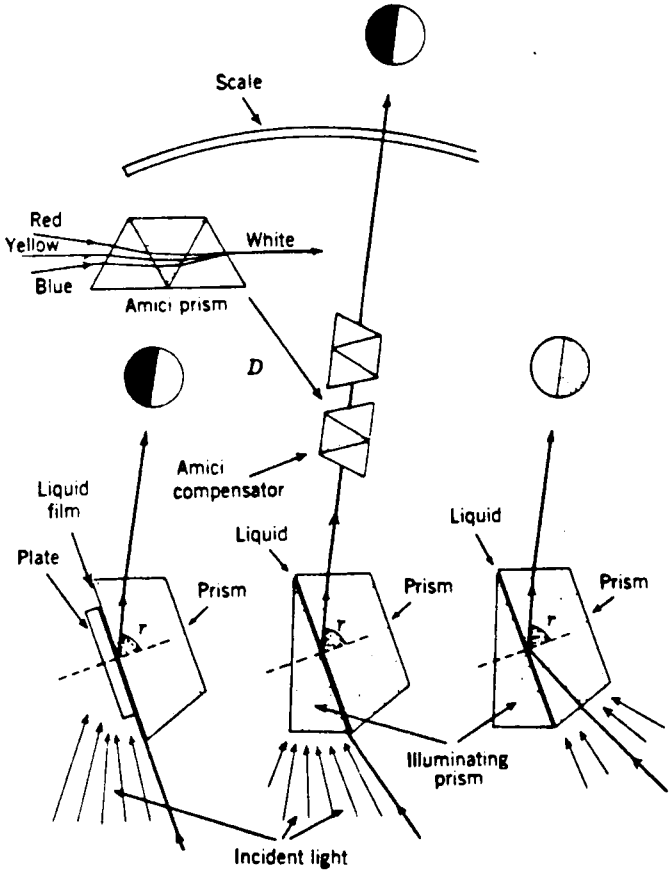


Figure II-16. Cross section of an Abbe' refractometer: (a) solid plate; (b) liquid film and (c) liquid film with light incident in a manner different from that in (b).

Source: Wahlstrom, E.E., "Optical Crystallography", John-Wiley and Sons, New York (1978), p. 147.

Since refractive index changes markedly with temperature, especially in the case of liquid samples the two prisms are enclosed in hollow casings through which water may be passed. Refractive index is reported with regard to a reference temperature and wavelength of light, for example, the designation, n_D^{25}, represents refractive index measured using the D-line of sodium as the illumination source and at a temperature of 25°C.

Application to Anisotropic Solids. Okajima and Koizumi (93) first applied the technique to determining the refractive index of anisotropic solids. The analysis presented below is that described by Samuels (115,116). The quantities n_1, n_2, n_3 are defined as the principal refractive indices measured with plane polarized light having its electric field vectors parallel to the corresponding principal directions 1, 2, and 3 in the anisotropic solid. As shown in Figure II-17 unpolarized light is scattered at the rough ground surface of the illuminating prism. Since the solid is optically anisotropic, upon passing through the material the light will no longer be unpolarized. The light rays scattered at point A will consist of two sets of plane polarized rays. The electric field vectors of the light rays can be decomposed into two sets of components, one set being polarized parallel to the x-y plane while the other is polarized perpendicular to the plane.

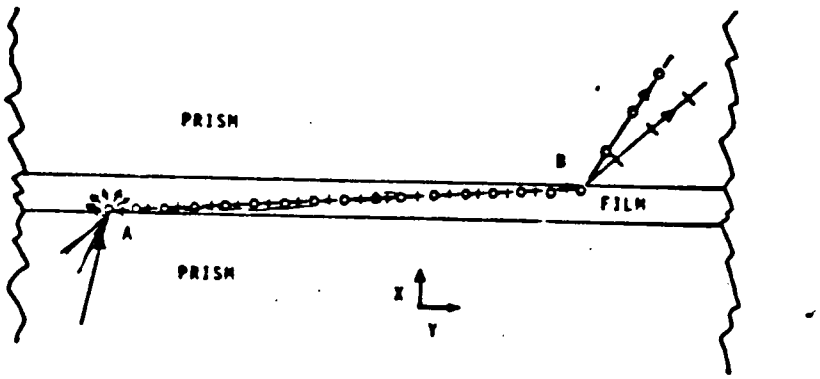


Figure II-17. Diagram showing the position of film between the prisms of an Abbe' refractometer. Polarized components of limiting rays are refracted separately at point B.

Source: Samuels, R.J., J. Appl. Polym. Sci., 26, 1383 (1981).

Upon entering the refracting prism at point B, the polarized components of the critical rays are refracted through different angles. Each set of rays can be descriminated from each other with the aid of a Polaroid analyzer mounted on the refractometer eyepiece. A complete description of experimental procedure is given in Table II-1.

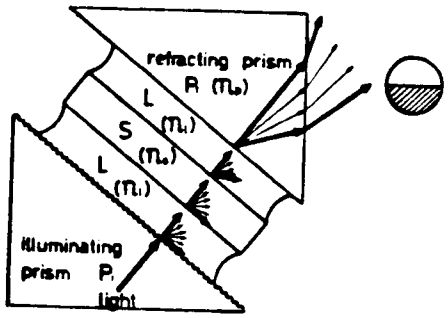
Schael (117,118) used the technique to study the effect of process conditions on orientation development in polyethylene and polypropylene films. Samuels (115) applied the technique to oriented hydroxypropylcellulose (HPC) films and has recently (116) presented a detailed description of the experimental procedure. Tanaka and coworkers (77,93,137,138) observed that two different values of refractive index were obtained depending on which surface of the film was in contact with the refracting prism. In order to study the distribution of refractive index through the thickness of cast films, Tanaka et al. constructed multilayer films from thin polypropylene cast sheet. Both one-piece and laminate films were quenched under identical conditions. Measurements of the refractive indices of the individual surface layers were in good agreement with the readings obtained using one-piece films. An experiment using optically plane glass prisms having different refractive indices as shown in Figure II-18 was performed to eliminate any influence of surface roughness. Tanaka et al.

Table II-1

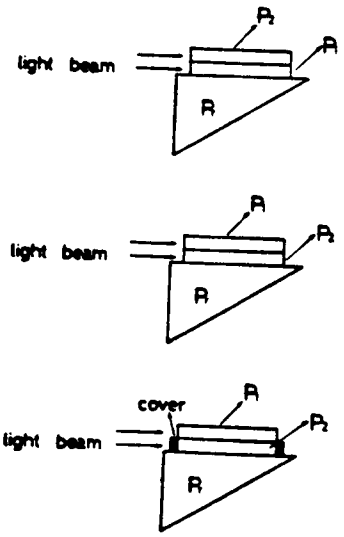
REFRACTIVE INDEX READINGS OBTAINED USING AN ABBE REFRACTOMETER

Sample MD axis P_r axis	Stretch Direction	Polaroid Analyzer Setting (degrees)	Refractive Index Reading
Parallel	ND	0	n_3
	TD	90	n_2
Perpendicular	ND	0	n_3
	MD	90	n_1

Source: Samuels, R.J., J. Appl. Polym. Sci., 26, 1408 (1981).



(a)



(b)

Figure II-18. Schematic of the Abbe' refractometer: P_i, illuminating prism; P_r, refracting prism; S, sample; L, contacting liquid; n_p, n_L, and n_s represent the refractive indices of P_r, L, and S, respectively; (b) positions of glass prisms with different refractive indices on the refracting prism. Arrows indicate path of light beam.

Source: Tanaka, H., T. Masuko and S. Okajima, J. Appl. Polym. Sci., 16, 443 (1972).

concluded that the refractive index measured with an Abbe' refractometer is that of a surface region of the film in contact with the refracting prism independent of the refractive index distribution within the film.

A limitation of the measurement of the three principal refractive indices with the Abbe' refractometer is that only the value at the surface is obtained. If the properties of the film surface are significantly different from those of the bulk, as is likely to be the case for thick films exposed to thermal or deformation gradients, the refractive indices obtained will not be a true representation of the state of orientation in the film. This limitation can be overcome by utilizing interferometric methods.

c. Interferometry

In this section the principles of the interference phenomenon in relation to the operation of the interference microscope are described and the application of interferometry to the study of inhomogeneity in polymers especially oriented fibers and films is discussed.

Theory. The phenomenon of the interference of light provides an alternate and more precise means of determinig refractive index. The relative phases of the emergent beams are determined by differences in optical path length through the specimen. Optical path length is defined as the product of refractive index and distance. Interference refers to the interaction of light waves regardless if the result is

an increase or decrease of intensity as shown in Figure II-19. Variations in physical distance or refractive index or both will produce phase interactions between emerging beams. The resultant image is called a interfernce pattern. If monochromatic light is used the differences appear as differences in intensity, while for white light a series of colored bands are seen.

The most intense fringe is called the zero order fringe, since it results from interference between beams which have no difference in optical path length. First order fringes result from the interference between beams which differ in optical path length by one full wavelength. Higher order fringes result from interference between beams which differ in path by 2, 3, 4, ..., n wavelengths.

Since the images formed by all wavelengths superimpose only at the center of the interference pattern, the white light image consists of a central white fringe surrounded by an overlapping series of colored higher order fringes which are formed by light of different wavelengths. Thus the zero order fringe can be identified by locating the position of the white fringe formed when the interferometer is illuminated by white light.

An interferometer is an instrument in which phase differences between light beams are obtained from their interference patterns. Interferometers are used for the

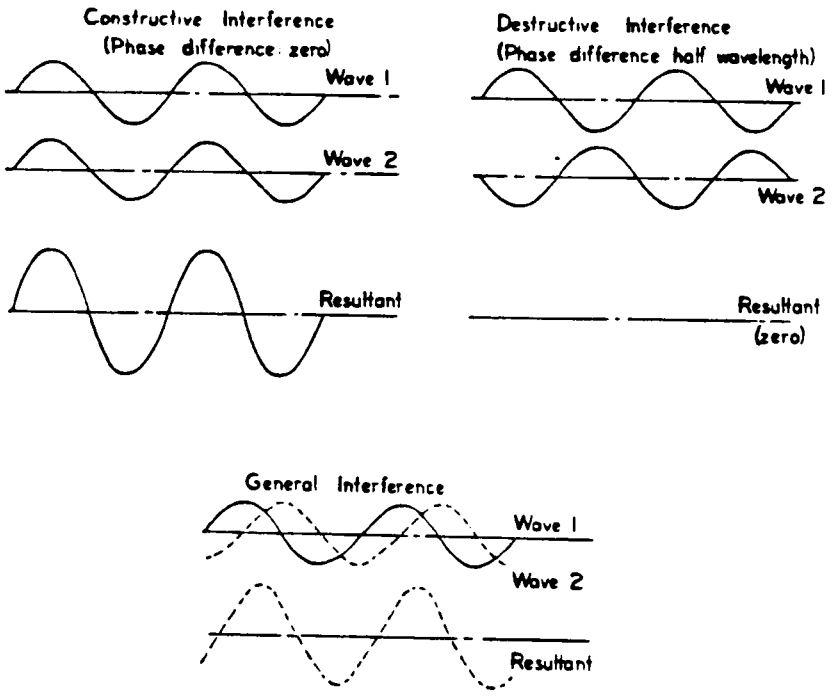


Figure II-19. The interference of light.

determination of either refractive index or thickness of a specimen.

d. The Interference Microscope

An interference microscope is essentially a combination of a microscope and an interferometer. The instrument uses the interference of light to form an image and then utilizes the components of a microscope to magnify the image.

The first interference microscope was introduced by Sirks in 1894 (42). Commercial microscopes did not become available until the late 1940's. Since then, numerous interference microscopes based on a wide variety of designs have been manufactured and are commercially available. Interference microscopy has been extensively used in the biological sciences and has recently become increasingly important in characterizing inhomogeneity in synthetic textile fibers spun at high speeds.

Interference microscopes can be classified as being either of two types; the double beam type or the multiple beam type depending on the method used to produce interference patterns. Both types of interference microscopes operate by causing light waves to interfere. The waves are divided so that they traverse different physical paths and finally the beams are recombined to produce an interference pattern. A summary of the principles and experimental technique involved is presented below. A more detailed description is given in references

(42,126,131,132,142,143). The advantages and limitations of each type will be discussed in the context of applying interference microscopy to the study of inhomogeneity in polymers.

Double-Beam Type. In a double-beam interference microscope, light passing through the specimen and light passing through the reference medium result in image contrast. A commercially available transmitted light interference microscope of the double-beam type is the Leitz interference microscope based on an adaptation of the interferometer developed by Mach and Zehnder (126).

The principle of operation is illustrated in Figure II-20. Light emerging from the illumination source S is split into two beams (1) and (2) by a semireflecting plate L_1. Beam (1) passes through beam splitter L_1, is reflected by mirror M_1, passes through the object P and the objective O_1, is reflected by another semireflecting plate L_2 and finally enetrs the ocular O_2. Beam (2) is reflected by semireflecting plate L_1 and mirror M_2, passes through a reference medium then through objective O_1' and L_2, and is combined with Beam (1) before entering the ocular O_2. The interference between the sample (1) and reference (2) beams produces an interference pattern.

A diagram of the actual microscope is shown in Figure II-21a. The instrument consists of two matched microscopes contained in a single housing: one microscope

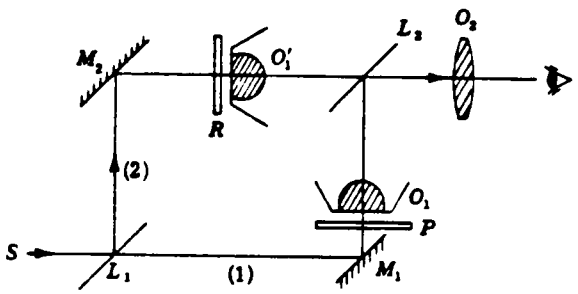


Figure II-20. Principle of operation of the Leitz interference microscope.

Source: Hale, A.J., "The Interference Microscope in Biological Research", E. & S. Livingstone LTD, Edinburgh and London, (1958), p. 286.

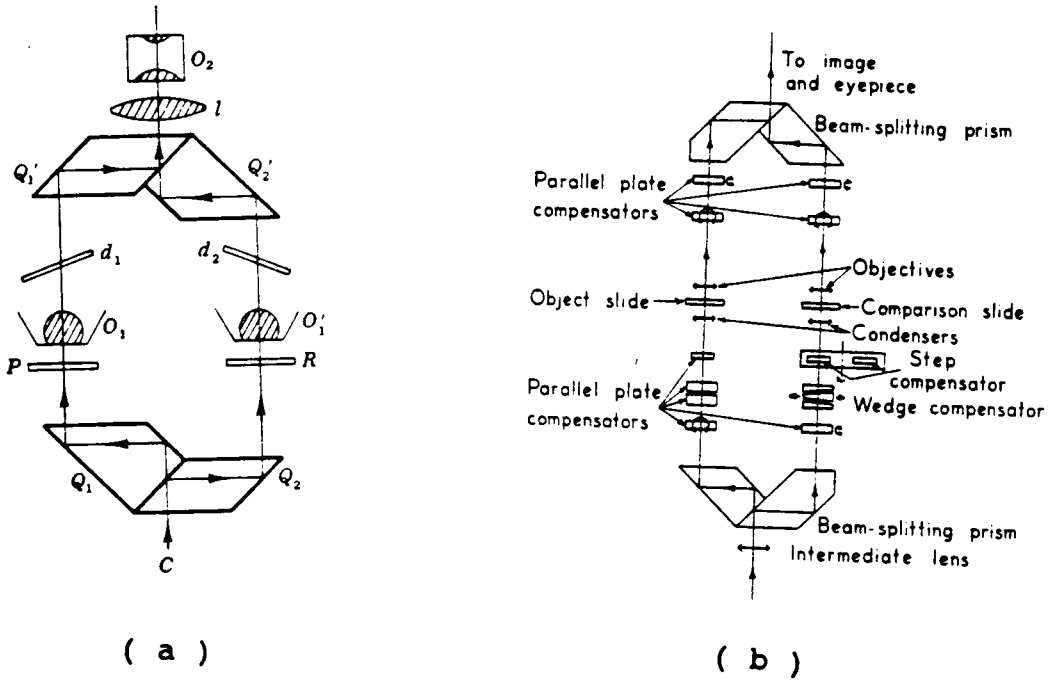


Figure II-21. The Leitz interference microscope. (a) Schematic and (b) Illustration showing actual components.

Source: Hale, A.J., "The Interference Microscope in Biological Research", E. & S. Livingstone LTD, Edinburgh and London, (1958), p. 123.

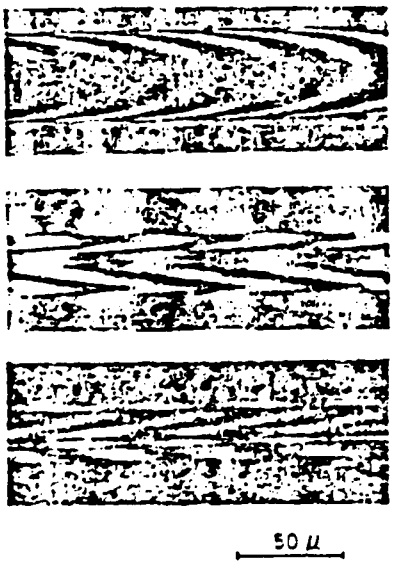
for the specimen and the other for the reference beam. In the actual microscope, the semireflecting plates L_1 and L_2 together with the mirrors M_1 and M_2 are replaced by a combination of prisms Q_1, Q_1', Q_2 and Q_2' as illustrated in Figure II-21a. Illumination from a single source is divided by means of a beam splitting prism. The two beams are separated by 62 mm (126). The plane-parallel plates d_1 and d_2 are used to vary the path difference between the specimen (1) and the reference (2) beams. Coarse adjustment of the optical path is controlled by the step compensator as can be seen in Figure II-21b.

An important application of this type of interference microscope is in the determination of the refractive index of anisotropic solids. Since anisotropic solids have at least two different refractive indices, the microscope is equipped with a polarizer. A portion of the incident polarized light passes through the specimen while the other part passes through the reference. The specimen is mounted in a liquid of known refractive index and is oriented so that its optic axis coincides with on of the two positions of extinction. The two beams are recombined and the resultant retardation appears as differences in amplitude in the image. The retardation is measured by means of a built-in wedge compensator as shown in Figure II-21b. If the thickness at a given point in the specimen is known, the refractive index can be calculated directly.

Recently, Roche and Davis (112) presented a detailed description of how the double beam technique can be used to study inhomogeneity in high speed spun fibers. Shimizu et al. (123) investigated the effect of spinning speed on PET fibers as illustrated in Figure II-22. Transverse interference patterns obtained using a double-beam interference microscope revealed a skin--core morphology in PET fibers spun at high speeds. Fibers spun at 2,000 m/min produced symmetric interference patterns whereas those spun at 9,000 m/min produced asymmetric patterns as shown in Figure II-22.

Pluta (100,101) developed a polarizing interference microscope with a variable amount and direction of wavefront shear. Hamza and Sikorski (45) used the Pluta double refracting microscope to study the optical anisotropy of poly (p.phenylene terephthalamide) fibers.

Multiple-Beam Type. As the name suggests, multiple beam techniques utilize more than two beams to produce interference fringes. These systems are based upon the etalon which has been derived from the Fabry-Perot type of interferometer (83,84,142,143). This method differs from the double-beam method in that interference is produced between two very closely spaced partially transmitting highly reflective optical flats. The two optical flats inclined at an angle are commonly referred to as a wedge. The larger the angle the smaller the separation between



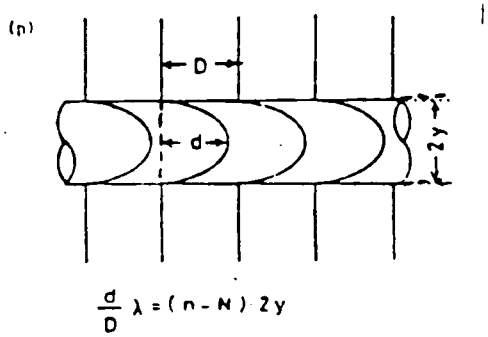


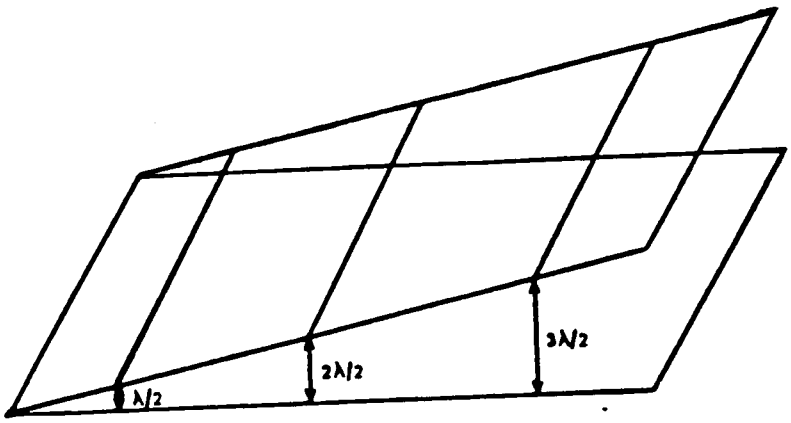
Figure II-22. Transverse interference patterns of PET fibers under an interference microscope. (a) 2,000 m/min; (b) 9,000 m/min (symmetric interference fringe pattern); (c) 9,000 m/min (asymmetric interference fringe pattern), (b) and (c) are the same sample observed from different directions.

Source: Shimizu, J., N. Okui and T. Kikutai, Sen-i-Gakkaishi, 37, T135 (1977).

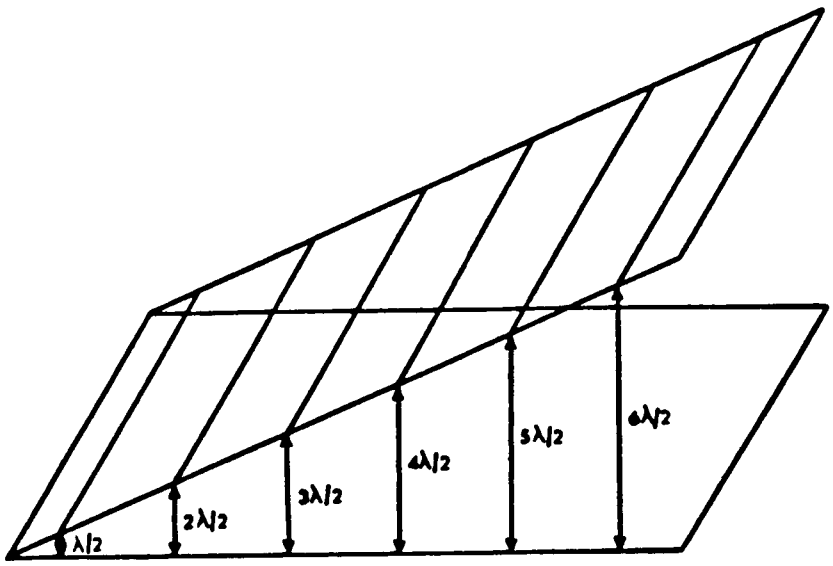
adjacent fringes as can be seen in Figure II-23. In transmission, the specimen to be examined is placed between the wedge, and the wedge is illuminated with a beam of monochromatic parallel light. The beam undergoes multiple reflections between the wedge as shown in Figure II-24. Thus multiple beam fringes are inherently sharper than are double beam fringes. The specimen causes a retardation of the beam each time the beam passes through the wedge, thus retardation for any given reflection transmitted through the inferometric wedge is double that of any preceeding reflection. Any minute difference in refractive index or thickness in the specimen will result in a change in intensity and displacement of the fringe.

Measurements made by multiple beam methods are more precise than those made with double beam methods. Multiple beam methods can be used to detect differences in optical path length as small as 10 A whereas double beam methods are limited to path lengths of several hundred Angstroms. A diagram of a commercial multiple-beam interference microscope is presented in Figure II-25.

Multiple beam methods have been used to study radial variations in refractive indices in oriented fibers (6,7,34,36,43,44,45). Barakat and coworkers (6,7) have used multiple-beam methods to study skin--core type structures in acrylic fibers. Barakat derived mathematical expressions



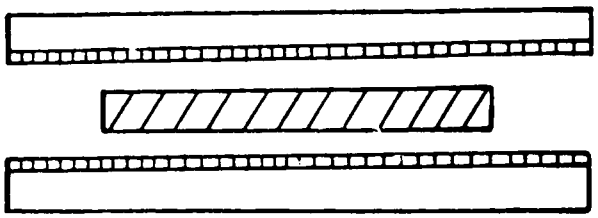
(a)



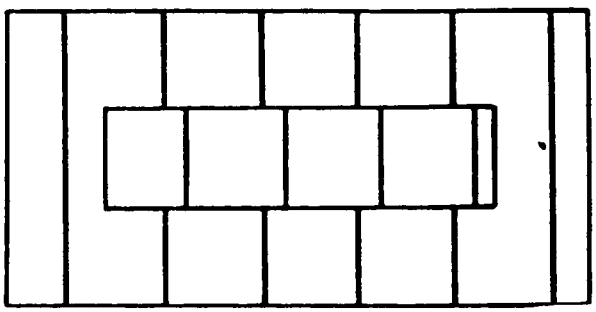
(b)

Figure II-23. Straight line fringes produced by a wedge: (a) small angle between plates and (b) wedge angle increased.

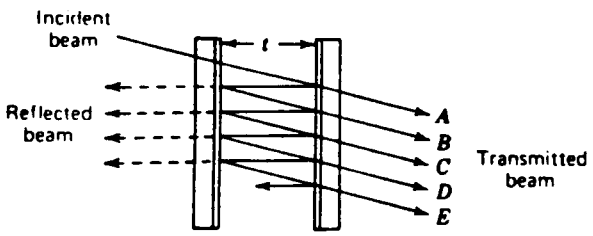
Source: Tolansky, S. "Microstructure of Surfaces Using Interferometry", American Elsevier, New York (1968), p. 9.



(a)



(b)



(c)

Figure II-24. Reflection and transmission from parallel plates: (a) wedge; (b) fringe pattern and (c) ray diagram.

Source: Slayter, E.M., "Optical Methods in Biology", Wiley-Interscience, New York (1970), p. 311.

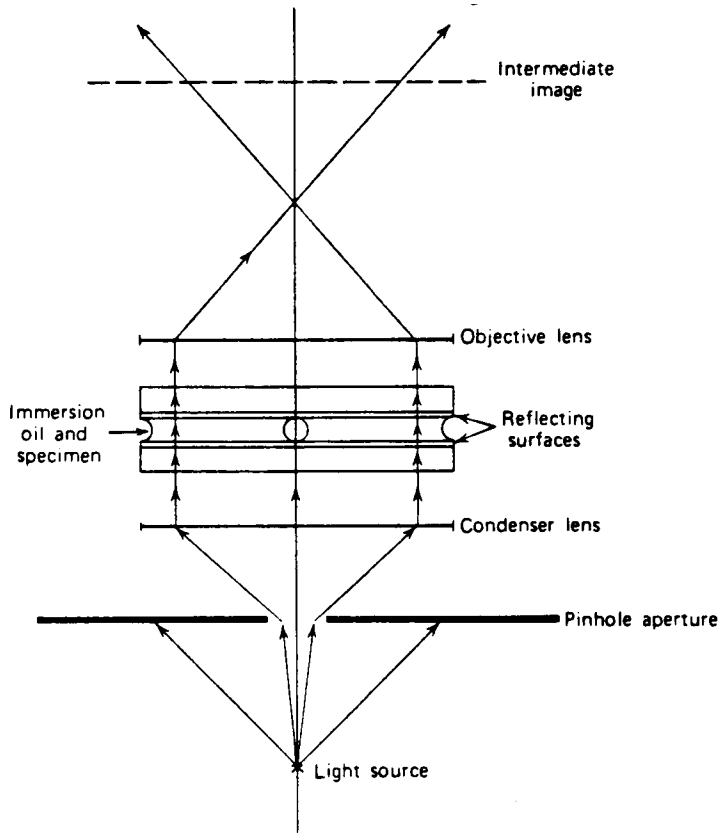


Figure II-25. Multiple-beam interference microscope.

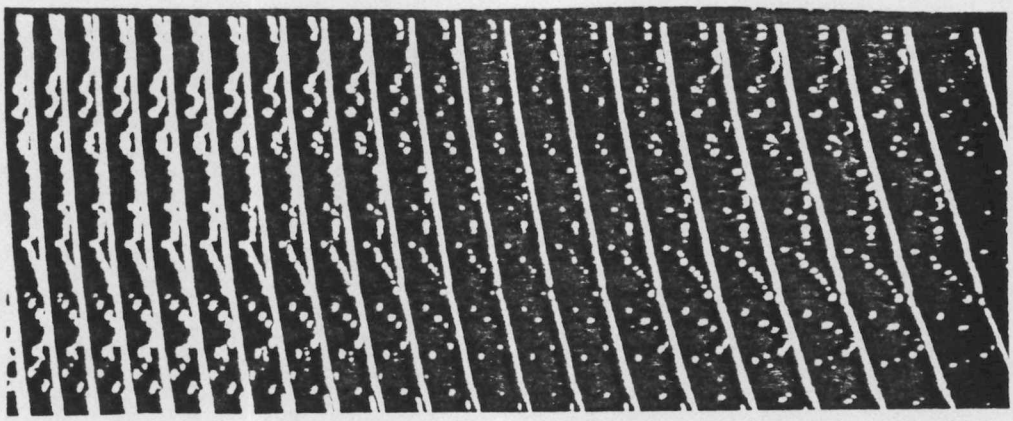
Source: Slayter, E.M., "Optical Methods in Biology", Wiley-Interscience, New York (1970), p. 315.

for the shape of multiple beam fringes crossing round fibers possessing a skin--core morphology.

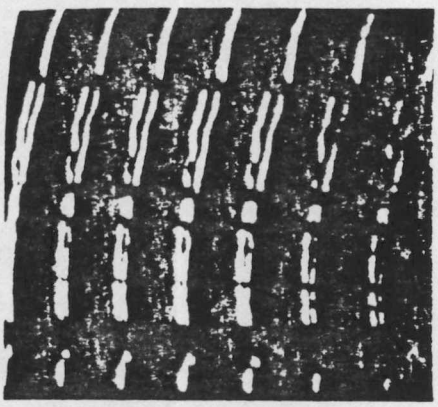
Faust (31,32,33) discusses both techniques and their applications including the need for sectioning specimens when an axis of symmetry is absent such as in oriented cellulose acetate sheet. Rhodes (109) applied the multiple-beam technique to unoriented polymer films. Variations in fringe patterns were observed in various regions of spherulitic films of polyethylene oxide, polyethylene and polypropylene. Multiple-beam fringe patterns from various films are shown in Figure II-26. The fringe patterns are complex especially for the polyethylene oxide spherulite.

Measurement and Calculation of Refractive Index. An interference microscope measures differences in optical path length, irrespective of whether double-beam or multiple-beam interferometric methods are used. Optical path length is defined as the product of the thickness, t, of the specimen and the difference in the refractive index (n_L - n) in the immersion fluid, n_L, and in the specimen, n.

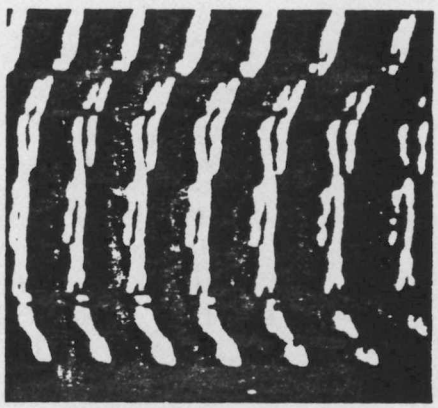
The optical path length between the interfering beams in the image field varies linearly across the field in a direction perpendicular to the field and is constant along any particular fringe. The intensity distribution of a double-beam interference pattern is illustrated in Figure II-27. Path length varies by one wavelength from one fringe to another. Thus, each point in the field



(a)



(b)



(c)

Figure II-26. Fringes of equal chromatic order from polymers: (a) a polyethylene oxide spherulite at room temperature; (b) a polypropylene shperulite growing at 140^{o}C and (c) after sample in (b) has cooled to room temperature.

Source: Rhodes, R.S., in "Structure and Properties of Polymer Films", R.W. Lenz and R.S. Stein Eds., Plenum Press, New York (1973), p. 115.

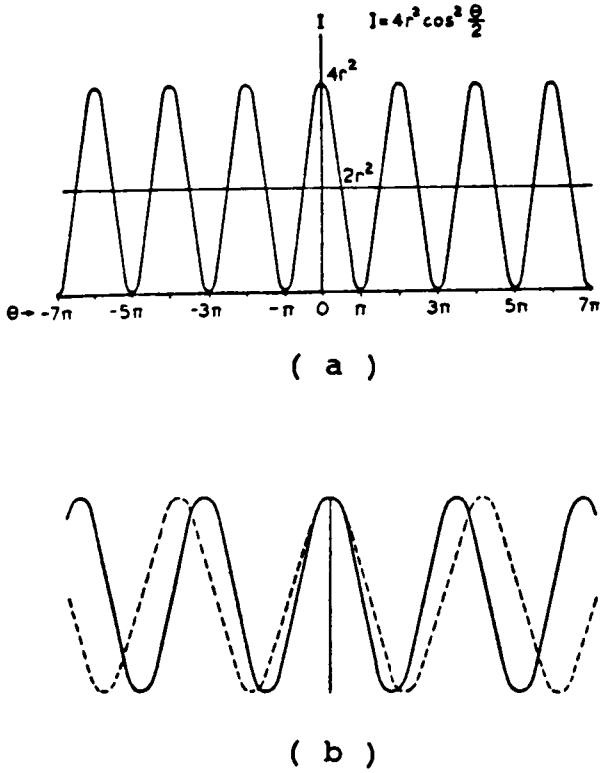


Figure II-27. (a) Intensity distribution of a double-beam interference fringe pattern. (b) The dependence of color and color mixing on wavelength in a fringe system.

Source: Hale, A.J., "The Interference Microscope in Biological Research", E. & S. Livingstone LTD, Edinburgh and London, 1958, p. 5.

corresponds to a specific path length between the two interfering beams. The difference of refractive index between the object and the surrounding medium causes one wave to be accelerated or retarded. The result is an alteration of path length by an amount $(n_L - n)t$.

For specimens of known thickness, the refractive index can be computed directly from a measurement of optical path length. In practice fringe patterns are recorded on photographic film and subsequently enlarged, recent developments include automated data acquiscistion and computer-aided analysis.

Fringe displacements are related to refractive index and specimen thickness according to the following relationship

$$d(x) / D = (n(x) - n_L) t / \lambda \qquad \text{(II-9)}$$

where d is the fringe displacement at a specific point, D is the distance between undisplaced adjacent fringes, l is the wavelength of light used, typically λ = 4560 Å for the mercury green line, t is the specimen thickness at the point where d is measured, n is the refractive index at point x and n is the refractive index of the immersion fluid. For each fringe displacement, d, measured on the film, a set of n values exists.

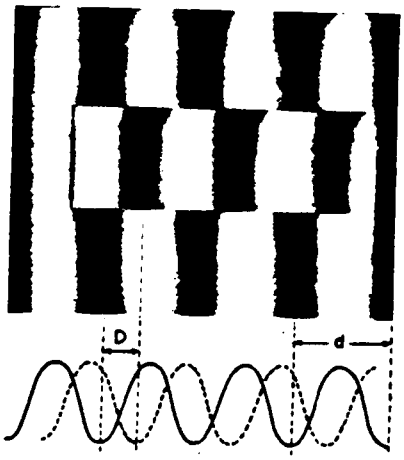
Application to Inhomogeneity in Polymer Films. The pattern produced by a large optically homogeneous object of

uniform thickness for example, a homogeneous cross section of an oriented polymer film is shown in Figure II-28. Since the object is optically homogeneous, the optical path length associated with all points through the thickness are displaced by the same amount. The variation in light intensity across the object and image field are shown as dashed and solid curves respectively.

In the case of biaxial materials such as oriented polymer film, sections are required. Faust (31,32,33) describes the types of sections to be cut from biaxial materials. It is convenient to choose sections perpendicular to the film plane. The sections are chosen so as to contain two of the axes of the refractive index ellipsoid. As shown in Figure II-29 two sections designated as MD and TD are cut from a sample. The sections are then examined in the interference microscope. Each section is positioned so that one axis is perpendicular to the microscope axis as illustrated in Figure II-30. If the direction of the incident light does not coincide with an optic axis of the film section, the light will be divided into two waves traversing the specimen with different velocities. The fringes will not appear as single bands but will be split into two overlapping bands. The fringe doublets correspond to the two refractive indices of the solid within the plane of the microscope. For specimens of uniform thickness, the fringe doublets are easily



(a)

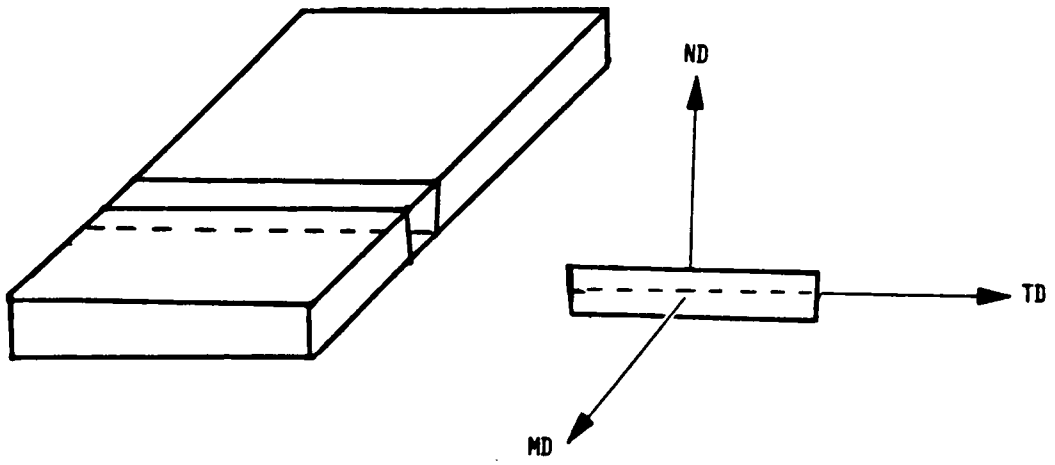


(b)

Figure II-28. (a) Fringe pattern produced by the interference of light in the image field of a double-beam interference microscope. (b) The fringe displacement produced by a large optically homogeneous section. The solid and broken curves represent fringe patterns in background and section, respectively.

Source: Hale, A.J., "The Interference Microscope in Biological Research", E. & S. Livingstone LTD, Edinburgh and London, (1958), p. 43.

MD SECTION



TD SECTION

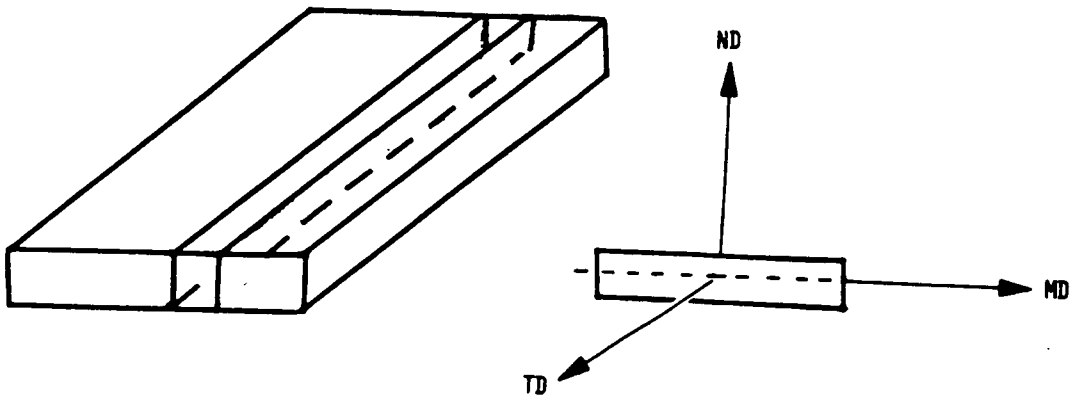


Figure II-29. Sections of a polymer film for interference microscopy measurements.

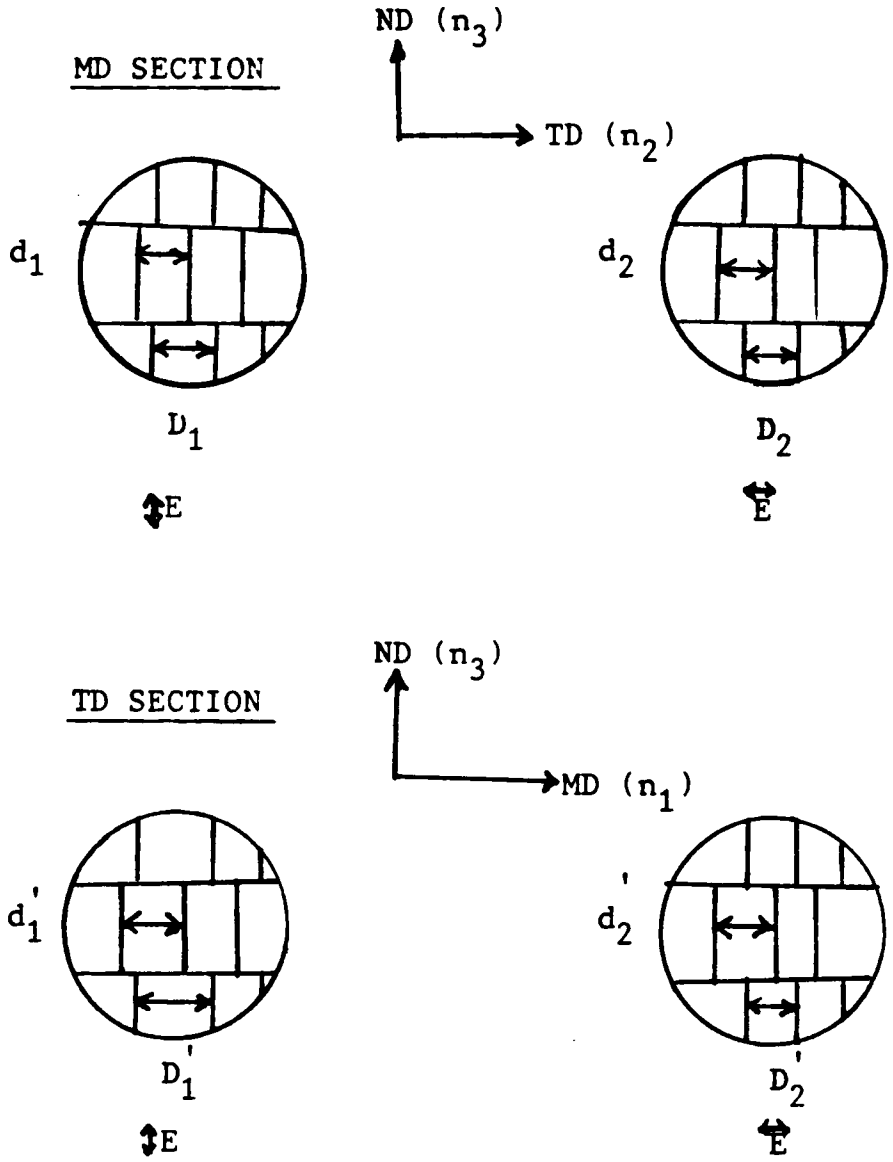


Figure II-30. Determination of principal refractive indices through the use of film sections.

distinguished, but in the case where specimens of highly irregular thickness or structure are examined, the overlapping fringes combine to form a highly complex pattern. In order to eliminate any confusion in discriminating between patterns, a polarizer is inserted in the incident beam, then each pattern can be resolved by positioning the polarizer so that the incident beam is plane polarized either parallel or perpendicular to the film section. The section is first examined with incident light vibrating parallel to a chosen axis and then perpendicular to the axis. Each section will then produce two-plane polarized fringe patterns, one for each of the two principal refractive indices. Equation II-8 can be used to calculate the refractive indices and therefore the birefringence at each point across the section. The resulting profiles providing an indication of the orientation distribution through the thickness.

Even under optimum conditions of sectioning a considerable degree of distortion occurs in the specimen. significant thickness variations in sections cannot be neglected when quantitative measurements are desired. A complete correction for thickness variations in each section would require a specific thickness profile of each individual section. Obviously, this is impractical, if not impossible to obtain, and furthermore any such experimental procedure would be extremely time consuming.

Since thickness variations will alter any measurement of refractive index, a correction must be made to account for this factor. The correction is easily obtained by examining the specimen in two different immersion fluids. Theoretically any of three parameters, namely temperature, wavelength or immersion fluid may be changed. The choice of using two different immersion fluids is a matter of convenience. For each fluid Equation II-8 can be applied

$$n = n_1 + d_1 \lambda / D\,t \qquad \text{(II-9a)}$$

$$n = n_2 + d_2 \lambda / D\,t \qquad \text{(II-9b)}$$

Eliminating thickness t, and solving simultaneously gives

$$n = n_{L1} + d_1 \left(n_{L1} - n_{L2} \right) / \left[d_2 - d_1 \right] \qquad \text{(II-10)}$$

Then both refractive index and thickness can be obtained.

It is particularly difficult to prepare smooth thin sections from polymers, since significant deformation occurs during cutting. In general, sections will possess some knife marks and wrinkling. As noted by Faust (30), if a cross section cut from a highly anisotropic film was not perfectly planar, but displayed significant wrinkling, noticeable fringe distortion would result as shown in Figure II-31. The irregularities in the fringe pattern originate from the fact that the optic axes of the specimen are oriented differently with respect to the microscope axis at various positions across the section. Fringe distortion



Figure II-31. Fringe distortion produced by a flat piece of mica between a wedge. The complex pattern is entirely due to wrinkling of the sample, not to differences in thickness or refractive index.

Source: Tolansky, S., "Interference Microscopy for the Biologist", Charles C. Thomas, Publisher, Springfield, IL., (1968), p. 150.

is a significant problem, especially if subtle variations in refractive index are present within the specimen.

The distinctive feature of the interference microscope is that it allows measurements of optical path length at a specific point to be made with a high degree of precision. From these measurements information on refractive index and thickness at the point can be obtained.

This method gives a refractive index profile for each section, rather than a value for the surface only as in the Abbe' method. In the preceeding sections, two techniques for measuring refractive index, critical angle refractometry and interferometry have been presented. A detailed study of structural inhomogeneity requires knowledge of the specific morphology and its distribution within the specimen. This information can be obtained with the aid of an electron microscope.

e. Electron Microscopy

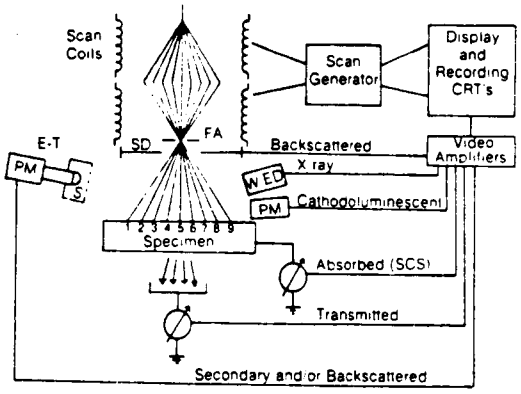
Electron microscopy unlike optical microscopy produces exceptionally high resolution of features in a specimen. The high resolution arises from the very short wavelength of electrons and the ability to produce a well-focused beam. There are several types of electron microscopes, two of which will be discussed here. These include the scanning electron microscope (SEM) and the transmission electron microscope (TEM). Generalized diagrams of both instruments

are presented in Figure II-32. A detailed description of the instruments and their operation in given in references (113,150).

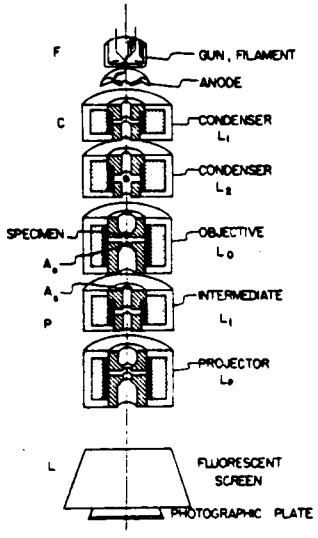
Scanning Electron Microscopy. Electrons originate in an electron gun, usually a hot filament and are deflected and focused by a series of magnets. The beam of electrons impinge on the surface of the specimen and are scattered. Scattered electrons from the surface are converted to electrical signals by a scanning probe and are seen as an image on a cathode ray tube (CRT). The resulting signals are secondary electrons, backscattered electrons, characteristic x-rays, Auger electrons and photons of various energies (113).

One of the most important aspects of the SEM image formed by secondary and backscatterred electrons is the resemblence to images of depressions and elevations illuminated from above by an oblique beam of light. SEM indirectly produces a topographical "image" of the specimen. The resultant image has a three-dimensional quality. Crystalline specimens produce contrast by electron channelling and by semiconducting or magnetic effects. Even at high magnification the depth of focus and resolution far exceed that of the optical microscope.

In studies of polymer morphology, SEM photomicrographs of fracture surfaces are routinely used. The specimen is first cooled in a cryogenic medium, typically liquid



(a)



(b)

Figure II-32. Diagrams of electron microscopes: (a) scanning electron microscope and (b) transmission electron microscope.

Source: Rochow, T.G. and E.G. Rochow, "An Introduction to Microscopy by Means of Light, Electron, X-rays or Ultrasound", Plenum Press, New York, (1978) p. 247-274.

nitrogen and then fractured. Peeling techniques have been used to study the morphology of fibers especially those having a fibrillar superstructure (146).

Transmission Electron Microscopy. In TEM the image is formed from electrons which pass through the specimen. The resultant beam will be composed of some of the original electrons which have not interacted with the specimen and some electrons which have undergone changes in direction or velocity or both. Since the electron image cannot be viewed directly, the image is projected onto a fluorescent screen and ultimately onto photographic film.

The thickness of the specimen in TEM is critical. The specimen must be thin enough to allow for significant penetration of electrons and yet thick enough so that some preferential absorption occurs. Typical specimen thicknesses are below 1000 A.

A transmission electron microscope can be used to obtain electron diffraction patterns. A particular advantage of electron diffraction as opposed to x-ray diffraction is the ability to obtain patterns from specific areas of the specimen. In selected area diffraction a small region of the specimen is chosen and the diffraction patterns of this part is obtained. Typically, a microscopic image is obtained and after proper adjustment of the aperture, the lens currents are altered to produce a diffraction pattern. The analysis of electron diffraction

patterns is analogous to that of x-ray patterns. The technique can be used to detect variations in crystallinity and orientation.

Both SEM and TEM are extremely useful in studying the morphology of semicrystalline polymer films and fibers. Yeh and coworkers (39,155,156) used both techniques to investigate the structure of drawn and annealed PET films.

CHAPTER III

MATERIAL AND EXPERIMENTAL PROCEDURES

A. MATERIAL

Samples were prepared from PET pellets and cast sheet supplied by the Film Division of American Hoechst Corporation. Cast sheet was supplied in the form of roll samples ranging in thickness from 279 μm (11 mil) to 1067 μm (42 mil). The PET contained no additives or fillers (105). Density of cast sheet samples was determined in a density gradient column composed of n-heptane and carbon tetrachloride at 23°C. The general characteristics of cast sheet samples are listed in Table III-1.

B. SAMPLE PREPARATION

a. Slab Films

PET pellets were molded into 25.4 mm X 38.1 mm X 3.2 mm (1.0 in. X 1.5 in. X 0.125 in.) slabs using a manually operated ram injection molding machine. Prior to molding the pellets were dried in an oven at 120°C under vacuum for about 18 hours. A quantity of pellets was introduced into the barrel and heated at 290°C for five minutes. The melt was injected into a aluminum mold and the mold quickly removed from the machine and quenched in an ice water bath. Density measurements confirmed that the as-molded 3.2 mm (0.125 in.) thick samples were essentially amorphous.

Table III-1

CHARACTERISTICS OF PET CAST SHEET

Cast Sheet Sample	Thickness μm (mil)	[η] (g/dl)	Percent DEG	Density (g/cm^3)
C1	279 (11)	0.61	3.34	1.339
C2	483 (19)	0.61	3.51	1.339
C3	762 (30)	0.61	3.46	1.339
C4	965 (38)	0.61	3.19	1.338
C5	1067 (42)	0.61	3.32	1.338

Samples thicker than 3.2 mm (0.125 in.) could not be quenched to give amorphous samples. All molded samples were stored in a desicator to minimize moisture absorption.

b. Laminate Films

Multilayer films hereafter referred to as laminate films were prepared from cast sheet sample C1 using a hot press (Wabash Metal Products, Inc., (Wabash, IN)). Laminate films used in refractive index studies are listed in Table III-2. Cast sheet samples were dried at 120°C for 18 hours prior to molding. Films were constructed by alternately stacking 23 μm (0.91 mil) aluminum foil and pieces of sample C1 sheet as shown in Figure III-1. The aluminum foil acting as a spacer between adjacent layers. The surfaces of the aluminum foil were lightly coated with a silicone mold release agent (Miller-Stephenson Chemical Co., Inc., (Danbury, CT)) to prevent sticking of the individual layers. The laminate was then inserted between two aluminum plates.

The stack was placed in a hot press at 290°C for five minutes, after which time the press was closed and the pressure raised to 12 tons. The press was held at this pressure for one minute. The stack was removed and quenched in an ice water bath. Control groups were prepared in an identical manner except for the absence of the aluminum foil spacers.

Laminate films for stretching experiments were prepared by layering four pieces of cast sheet sample C1 together and

Table III-2

LAMINATE FILMS FOR REFRACTIVE INDEX MEASUREMENTS

Film Sample	Thickness of Laminate μm	(mil)	No. of Sample C1 Sheets	Number of Aluminum Spacers	Thickness of Metal Plates mm	(in.)
L1	533	(21)	3	4	0.5 0.5	(0.020) (0.020)
L2	533	(21)	3	4	0.5 3.2	(0.020) (0.125)
L3	1067	(42)	7	8	0.5 0.5	(0.020) (0.020)
L4	1067	(42)	7	8	0.5 3.2	(0.020) (0.125)

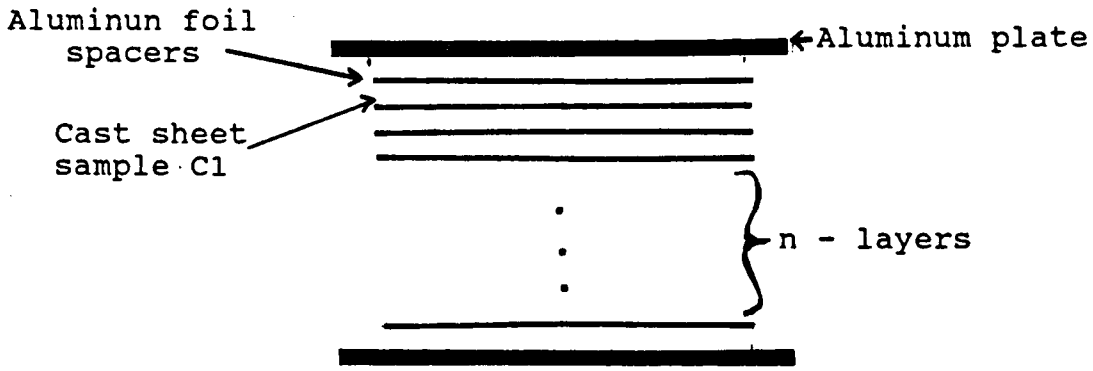


Figure III-1. Cross section of laminate film.

cementing the outer edges with a small quantity of epoxy (3M, (Minneapolis, MN)). A thin coating of Dow Corning 200 Silicone Fluid (Dow Corning, (Midland, MI)) was placed between the layers to facilitate in the separation of the individual layers after stretching.

c. Stretching of Cast Sheet

Cast sheet samples C1 and C5 were stretched on a T.M. Long Biaxial Film Stretcher (T.M. Long Co. (Sommerville, N.J.)). Deformation modes shown in Figure III-2, included uniaxial (U) and uniaxial with lateral constriant hereafter referred to as "uniaxial constant width (UCW)." Cast sheet sample sizes prior to stretching were 60 mm X 45 mm (2.4 in. X 1.8 in.) and 60 mm X 60 mm (2.4 in. X 2.4 in.) for uniaxial and uniaxial constant width films, respectively. Strain rates of 0.4, 1.8, 3.6, 10.0 and 40.0 min^{-1}, respectively were used. Immediately upon completion of stretching, the sample was quenched to room temperature using a stream of cold air.

Gradient films were prepared by establishing thermal gradients in cast sheet samples prior to stretching. Gradients were imposed by using different combinations of air stream temperatures. Air stream temperatures of 70°C and 120°C were utilized as were 50°C and 150°C. A sample was placed in the heating chamber of the stretcher and exposed to the two different air streams for residence times of 1.0, 1.5 and 2.0 minutes before being stretched. A

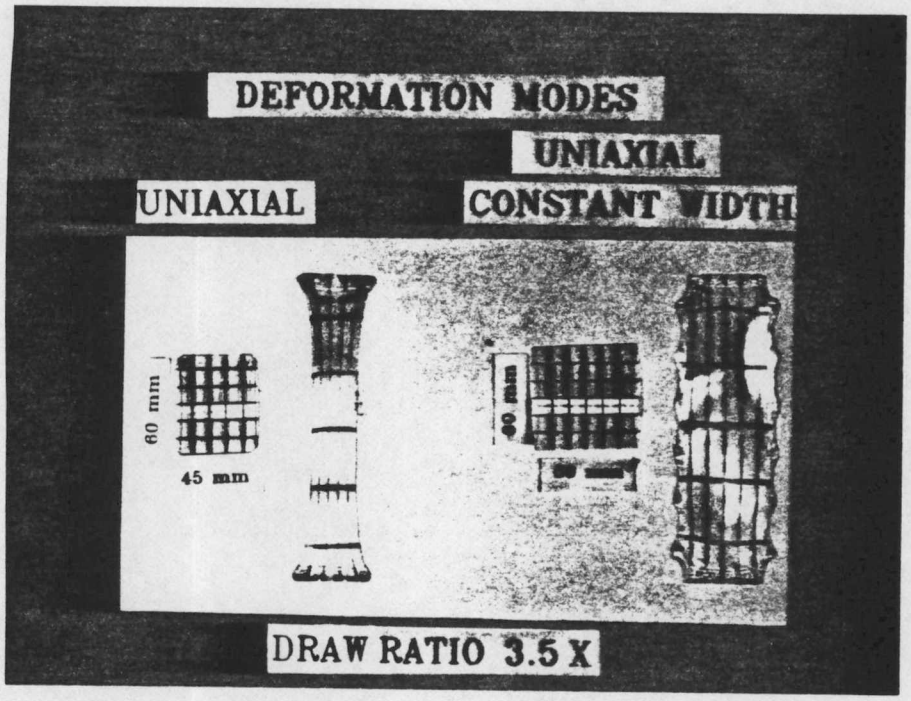


Figure III-2. Deformation modes.

complete list of conditions is given in Table III-3. Following the completion of stretching the sample was rapidly cooled to below the glass transition using a stream of CO_2 gas.

Both surfaces of each cast sheet specimen were marked with a 1 mm X 1 mm (0.25 in. X 0.25 in.) color-coded grid. All films were streched to a nominal draw ratio of 3.5X. The actual draw ratios were determined from the displacement of the grid marks in the drawn portion of the final specimen. Actual draw ratios ranged from 3.41X to 3.65X. In the case of gradient films, a blue grid was used to represent the surface exposed to the low temperature air stream and correspondingly a red grid to represent the side of the sheet exposed to the high temperature air stream. For laminate films a grid was marked on both sides of each individual layer.

d. Force--Elongation Measurements

Forces were recorded during stretching using the force transducers furnished with the T.M. Long Stretcher. Transducer outputs were calibrated following the procedure described by the manufacturer. Millivolt responses were recorded on a strip chart recorder and subsequently converted to forces using a calibration scale.

Table III-3

CONDITIONS PRIOR TO STRETCHING CAST SHEET SAMPLES

Film Sample	Cast Sheet Sample	Lower Air Stream Temperature (°C)	Upper Air Stream Temperature (°C)	Preheat Time (min)
NGA1	C1	80	80	2.0
NGA2	C1	90	90	2.0
NGA3	C1	100	100	2.0
NGA4	C1	110	110	2.0
NGB1	C5	80	80	2.0
NGB2	C5	90	90	2.0
NGB3	C5	100	100	2.0
NGB4	C5	110	110	2.0
GA1	C5	70	120	1.0
GA2	C5	70	120	1.5
GA3	C5	70	120	2.0
GB1	C5	50	150	1.0
GB2	C5	50	150	1.5
GB3	C5	50	150	2.0
NGL1	C1	80	80	2.0
NGL2	C1	90	90	2.0
NGL3	C1	100	100	2.0
NGL4	C1	110	110	2.0
GL1	C1	70	120	2.0
GL2	C1	50	150	2.0

NG - Nongradient, G - Gradient

NGL - Nongradient Laminate, GL - Gradient Laminate

C. CHARACTERIZATION OF CAST SHEET AND DRAWN FILMS: AVERAGE PROPERTIES

a. Density Measurements

Densities were measured at 23°C in a density gradient column composed of an aqueous sodium bromide solution. Density values within the column ranged from 1.325 g/cm^3 to 1.4000 g/cm^3. The density of a sample was determined after being immersed in the column for about 24 hours. Densities are believed to be accurate to within $\pm$ 0.0005 g/cm^3.

The volume percentage crystallinity X_c was determined from the following relationship

$$X_c = \frac{\rho_m - \rho_a}{\rho_c - \rho_a} \times 100 \qquad \text{(III-1)}$$

where ρ_m is the messured density, ρ_a is the amorphous density and ρ_c is the theoretical density for a 100 percent crystalline material.

The densities of the crystalline and amorphous regions were taken to be 1.333 g/cm^3 (29) and 1.455 g/cm^3 (23), respectively.

b. Differential Scanning Calorimetry

The thermal behavior of cast sheet and selected stretched film samples was studied using a differential scanning calorimeter (Perkin-Elmer Model DSC-2B, The Perkin-Elmer Corporation, (Norwalk, CT)). Each film was cut into

identical circular shapes ranging in weight from 5 to 20 mg; and the sample placed in a standard aluminum sample pan. Cast sheet samples were heated at a constant rate of 20°C/min, whereas the rate used for some drawn film samples was 40°C/min. The instrument was calibrated with a indium standard (ΔH_m = 6.80 cal/g, T_m = 156.6°C (150)). Peak areas were calculated using a microprocessor software package supplied by Perkin-Elmer. The percent crystallinity was estimated from

$$X_c = (\Delta H_f / \Delta H_f) \times 100 \qquad \text{(III-2)}$$

where ΔH_f and ΔH_f are the heat of fusion for the sample and the theoretical heat of fusion for a 100 percent crystalline material. The latter value was taken to be 30 cal/g[3] (151).

Peak crystallization temperatures (T_c), melting points (T_m), crystallization and melting enthalpies and where possible glass transition temperatures (T_g) were obtained for each sample.

c. Refractive Index Measurements

Refractive index measurements of the film samples were made using an Abbe' Refractometer (Bausch and Lomb Model 12, Bausch and Lomb, (Rochester, N.Y.)) following the technique described by Samuels (116). Methylene Iodide (n_D^{25} = 1.738) was used as the immersion fluid and a sodium vapor lamp (λ = 5890 Å) was used as the illumination source.

A 30 mm X 40 mm (1.18 in. X 1.57 in.) piece of film was

cut from the central portion of the samples. In the case of uniaxial films a large enough sample could not be obtained therefore, the uncovered part of the measuring prism was covered with a piece of black paper and fastened with tape to prevent any stray light from entering the prism and reducing the contrast of the boundary line. Care was taken to evenly disperse the immersion fluid and prevent any air bubbles from being trapped between the sample and prism. A drop of immersion fluid was placed on top of the film prior to folding the illuminating prism into place.

Birefringence values were calculated from the following definitions

$$\Delta n_{12} = n_1 - n_2 \qquad \text{(III-3a)}$$

$$\Delta n_{13} = n_1 - n_3 \qquad \text{(III-3b)}$$

$$\Delta n_{23} = n_2 - n_3 \qquad \text{(III-3c)}$$

where subscript 1 corresponds to the principal stretch direction or machine direction (MD), subscript 2 to the transverse direction (TD) and subscript 3 to the sheet normal direction (ND) as shown in Figure III-3.

d. Small-Angle Light Scattering

A photographic light-scattering apparatus was used to obtain scattering patterns on selected film samples. The apparatus, similar to that of Stein and Rhodes (135), consists of a 2.5 mW helium-neon laser, a rotatable Polaroid

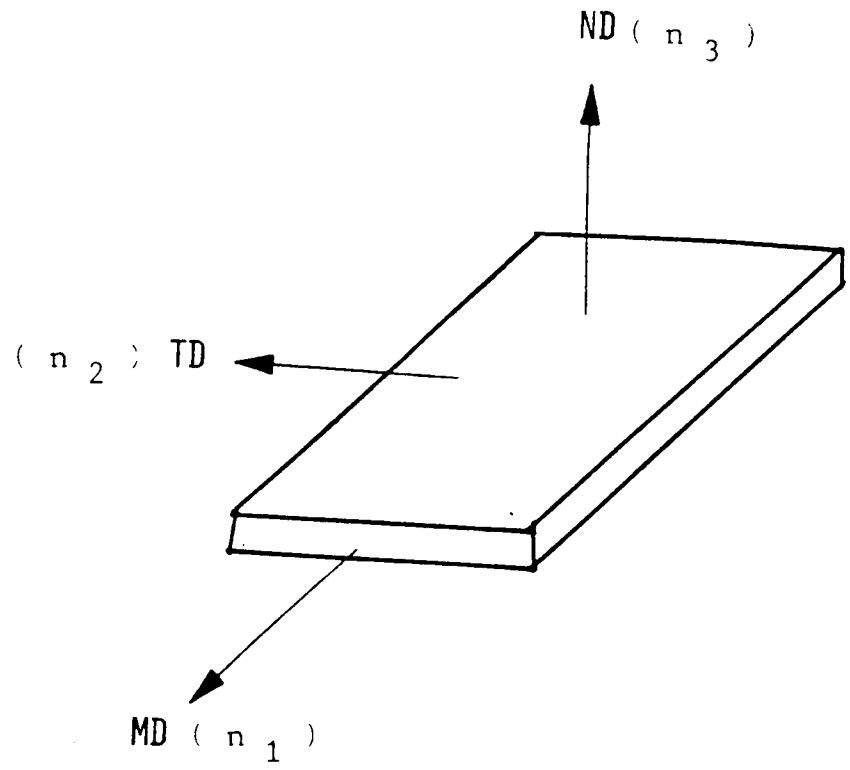


Figure III-3. Principal refractive indices of a polymer film.

polarizer, a mechanical shutter, a Polaroid analyzer and a sample mounting device. All components were mounted on a optical bench. Scattering patterns were recorded on Type 55 Polaroid Film (Polaroid Corp., (Cambridge, MA)). Exposure times varied with each specimen. Hv exposure times ranged from one to thirty seconds, while V_v times ranged from 1/10 to 1/50 second. Sample-to-film distance was 15 cm (5.9 in.) Specimens were mounted between a microscope slide and cover slip. Cargille Fluid, a silicone immersiom liquid (R.P. Cargille Labs, Inc., (Cedar Grove, N.J.)) was placed between the film and glass surfaces to eliminate any surface scattering.

D. CHARACTERIZATION OF THROUGH THE THICKNESS VARIATIONS IN CAST SHEET AND DRAWN FILMS

a. Heat Transfer Studies

Very fine wire thermocouples (0.025 mm (0.001 in.) diameter iron-constantan Type K wire) (Omega Engineering Inc., Stamford, CT) were attached to the surfaces of cast sheet specimens using the following technique: A very fine hot copper wire attached to a soldering iron was placed in close contact with the surface for a period of time sufficient to cause localized softening of the surface. A thermocouple was then lightly pressed onto the heated area and allowed to fuse to the surface; after thermocouple attachment the region was quenched with a stream of room

temperature air. The technique is believed to provide intimate contact with the polymer while minimizing the amount of damage to the surface.

In the case of laminate samples, fine (0.127 mm (0.005 in.) iron-constantan) thermocouples were placed between adjacent layers. All thermocouple responses were recorded on a strip chart recorder. Temperature measurements were made both during heating and cooling of one piece and laminate cast sheet samples.

b. Cutting and Polishing of Slabs for Birefringence

Sections (2 mm) were cut from slab films using a Gillins-Hamco thin-sectioning machine. A water stream was used to cool the specimen surface during cutting. The effects of cutting were removed by polishing the surfaces of the sections. Polishing was done in two steps. The first step involved sanding on a Buehler polishing table using successively finer grit emery paper (1/0, 2/0, 3/0 and 4/0 grit). Final polishing was performed on a Buehler polishing wheel using an aqueous suspension of 9.5 ìm aluminum oxide powder. The wheel was operated at its lowest speed.

c. Birefringence Measurements on Slabs

Birefringence measurements were made using a microscope and Babinet compensator following the procedure described by Wust (152). Retardation was merasured at various points across the thickness with the aid of a micrometer mounted on

the microscope--compensator apparatus. Birefringence profiles were calculated from the following expression

$$n = \Gamma_{avg} / t \qquad \text{(III-4)}$$

where Γ_{avg} is the average of the 0 and 90 degree compensator positions and t is the thickness for each point in the slab.

d. Refractive Index Measurements on Laminate Films

A 30 mm X 40 mm (1.18 in. X 1.57 in.) section was cut from the center of each laminate sample. The layers were removed one by one and the aluminum spacers peeled away from the films. The film surfaces were wiped free of any silicone mold release agent. Refractive indices of each layer were measured using an Abbe' refractometer with 1-bromonaphthalene (n_D^{20} = 1.658) as the immersion fluid.

Readings were obtained for both film surfaces, thus two sets of birefringences, one for each surface were calculated. In addition a differential birefringence defined as the difference of birefringence values obtained on opposite surfaces of the film was calculated from the following equations:

$$\delta n_{12} = \Delta n_{12} - \Delta n'_{12} \qquad \text{(III-5a)}$$

$$\delta n_{13} = \Delta n_{13} - \Delta n'_{13} \qquad \text{(III-5b)}$$

$$\delta n_{23} = \Delta n_{23} - \Delta n'_{23} \qquad \text{(III-5c)}$$

e. Preparation of Thin Sections for Microscopy

A small section was cut from the central portion of each sample. One end of the specimen was cut into a v-shape. Each specimen was placed in a size 00 Beem capsule (E.F. Fullam, Inc., (Schenectady, N.Y.)). The capsule was filled with EPOX 812 mounting medium (E.F. Fullam) and allowed to harden for 48 hours at room temperature. Some specimens were cured at 60°C in a laboratory oven for 12 hours. No difference in hardness or sectioning performance was observed between the two curing techniques. After hardening, the Beem capsule was cut away with a razor leaving the polymer specimen mounted in a epoxy stud. The stud was preshaped into a pyramid using a sharp disposable metal blade. In the case of sections used for interference experiments, the samples were partially mounted in epoxy. Sections were cut from the samples without any surrounding embedding media.

Thin sectioning was performed on a American Optical Model 812 thin sectioning microtome (American Optical Corp., (Southbridge, MA)) using a 45 degree glass knife. Some sections were cut on a LKB ultramicrotome (LKB Instruments, Inc., (Gaithersburg, MD)) using 45 and 60 degree glass knives. All glass knives were fitted with boats filled with a 30-70 percent mixture of isopropanol and water. Sectioning was performed at room temperature. Thin sections (1000 A) for TEM could not be successfully cut from film

samples at room temperature. Specimen thicknesses of 5, 10, 20 and 25 μm were obtained. A minimum of six sections for each sample were cut. Difficulties encountered in sectioning, namely wrinkling and thickness variations especially for sections of 10 μm or less is believed to be attributed to the relative softness of the samples. The microtomed cross sections were mounted on standard glass microscope slides and covered with a glass cover slip.

f. Refractive Index Measurements Using an Interference Microscope

A Leitz Double-Beam Interference Microscope (E. Leitz, Inc., (Rockleigh, N.J.)) was used to measure refractive index as a function of through the thickness position. The experimental procedure followed was that described by Roche and Davis (112), Davis (104) and Frankfort and Knox (34).

Prior to making any measurements the microscope was aligned. A pair of half-slides were prepared from a single clean microscope slide. A film section and a drop of immersion fluid (Cargille "Certified Index of Refraction Liquids") was placed on one half-slide. An ordinary clean glass coverslip was used to cover the specimen. Similarly, a drop of immersion fluid was placed on the other half-slide and covered with a coverslip. The two half-slides were then placed on the two stages of the microscope. A mercury lamp (λ = 5460 Å) was used as the illumination source and all measurements were performed using 40X objectives.

The film section was positioned so that the long axis is perpendicular to the pattern of interference fringes as shown in Figure III-3. A reference mark is placed on the microscope slide so that all susequent measurements are made at the same position along the length of the film section. The refractive index of the immersion fluid is chosen so as to provide the maximum displacement between adjacent displaced fringes within the section fringes, typically about 25 percent of the distance between undisplaced fringes. A photograph of the section and the associated fringe pattern is recorded on high speed high contrast film. The first immersion fluid is completely washed away from the section and a second fluid having refractive index n_{L2} is placed on the specimen. The refractive index of the second fluid is chosen so as to produce approximately the same displacement but in a direction opposite that obtained with the first fluid. The resultant image is focused and a second photograph taken. The analyzer is rotated by 90 degrees and the specimen is immersed in a third fluid. The same procedure was repeated for the TD section.
Table III-4 lists the experimental modes in which the refractive index measurements are made and the accompanying refractive indices obtained for each section.

g. Polarized Light Microscopy

Microtomed cross sections were examined under a Leitz ORTHOLUX polarizing microscope. Several photographs of

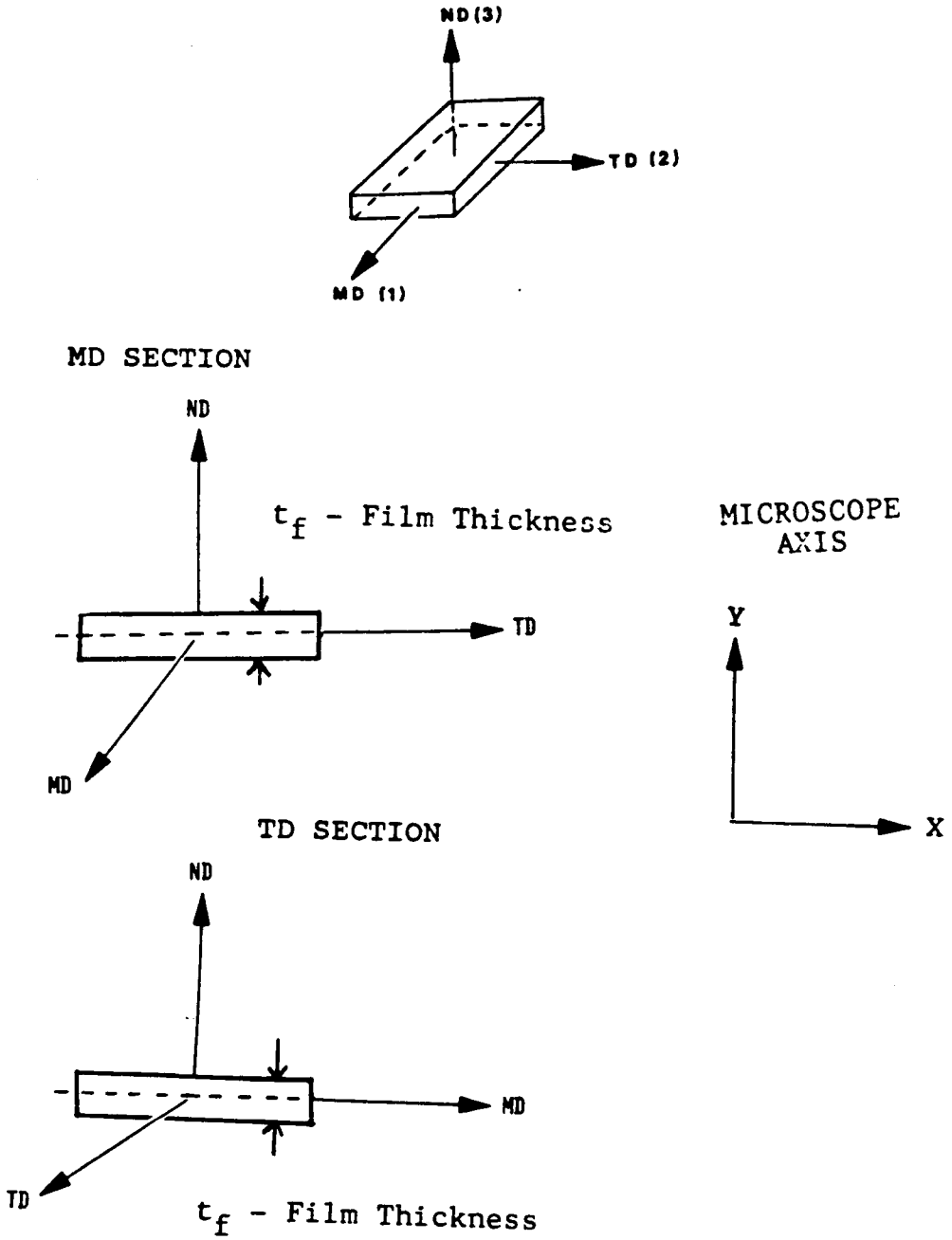


Figure III-4. Determination of the principal refractive indices of a polymer film by interference microscopy using sections.

Table III-4

EXPERIMENTAL MODES FOR DETERMINING REFRACTIVE INDICES FROM INTERFERENCE MICROSCOPY MEASUREMENTS

Film Section	Measurement	Analyzer Position (degrees)	Refractive Index	
			Immersion Fluid	Film
MD	1A	0	n_{L1}	n_3
MD	1B	0	n_{L2}	n_3
MD	1C	90	n_{L3}	n_2
TD	2A	0	n_{L1}	n_3
TD	2B	0	n_{L2}	n_3
TD	2C	90	n_{L3}	n_1

MD - Section cut perpendicular to the machine direction.

TD - Section cut perpendicular to the transverse direction.

selected cross sections were taken using Kodachrome 64 (Eastman Kodak Co., (Rochester, N.Y.)) color slide film. Oblique cross sections of films were also examined. Sections were cut at angles of 45 and 60 degrees to the film surface.

h. Chemical Etching

A 54.8 mm X 54.8 mm (2.0 in. X 2.0 in.) specimen was suspended without tension in 100 ml of n-propylamine (Reagent grade, Eastman Kodak, (Rochester, N.Y.)) in a covered beaker. Specimens were etched at room temperature without agitation for 1, 2, 4 and 8 hours. After a desired etch time, the specimen was removed from the amine bath, rinsed in fresh amine, rinsed thoroughly in distilled water and dried in a forced air oven at 30^{o}C for one hour.

The etched samples were examined using optical microscopy and SEM. Both surfaces were examined using an optical microscope and in addition selected samples were fractured in liquid nitrogen and the fracture surfaces observed using a scanning electron microscope.

CHAPTER IV

CHARACTERIZATION OF CAST SHEET AND DRAWN FILMS: AVERAGE PROPERTIES

Although the major emphasis of the present research was on the characterization of through the thickness inhomogeneity in uniaxially stretched PET films, a concurrent study was performed on the influence of temperature and strain rate on the overall properties of uniaxial and UCW films. This investigation provides a means of comparing nongradient and gradient films. The objective of this study was to demonstrate that although significant through the thickness orientation and structural gradients may exist, measurement of average properties may not reflect these gradients. That is, based on overall properties nongradient and gradient films may be indistinguishable.

This chapter is divided into four sections: the first is devoted to studies of PET cast sheet, the second and third deal with the characterization of nongradient and gradient films in terms of average properties and the fourth involves a comparison of nongradient and gradient films.

A. CAST SHEET

a. Density and DSC

Density and DSC measurements were performed on cast sheet samples to determine the existence and nature of any

structure which may have formed during casting. Any structures such as spherulites would influence drawing behavior and subsequent structure development. Crystallinities calculated from Equation III-1, show all cast sheet samples to be essentially amorphous having density crystallinities of about four percent. DSC thermograms show three distinctive features; the first at about 70°C corresponds to the glass transition, the second peak associated with crystallization is an exotherm at about 130°C and the third is an endotherm representing melting at around 249°C. Peak temperatures are listed in Table IV-1. Crystallization temperatures (T_c) and melting points (T_m) were obtained from the respective minima and maxima on the DSC curves. As shown in Table IV-1, peak crystallization temperatures and melting points are similar for all samples.

b. Refractive Index and Birefringence

In order to determine if the samples were optically isotropic, the principal refractive indices were measured using an Abbe' refractometer following the procedure described in Chapter III (see page 61). In addition, the isotropic refractive index n_{iso} was calculated from the average of the values obatined at both surfaces using the following relationship

$$n_{iso} = (n_1 + n_2 + n_3) / 3 \qquad \text{(IV-1)}$$

where n_1, n_2, and n_3 are the principal refractive indices of

TABLE IV-1

THERMAL CHARACTERISTICS OF CAST SHEET SAMPLES

Cast Sheet Sample	Temperatures (^{o}C) Glass Transition	Crystallization	Melting Point
C1	69	131	250
C2	71	130	248
C3	73	130	251
C4	70	130	249
C5	72	130	250

the film. The results are shown in Table IV-2. Associated birefringences were also determined and are listed in Table IV-3. All cast sheet samples are slightly oriented with the thickest sample C5 having the highest birefringence. This finding is significant, since any orientation present in the cast sheet would have an effect on the crystallization kinetics during stretching and on the final level of orientation in the stretched film. The effect of cast sheet thickness on n_{iso} can be seen in Table IV-2. The value of n_{iso} decreases with thickness, this is most likely a reflection of small differences in crystallinity.

c. Crystallization Behavior

Crystallization studies were conducted to determine the effect of residence time on the development of crystallinity in cast sheet sample C5. Crystallization of samples was carried out in the heating chamber of the T. M. Long Film Stretcher.

A comparison of isothermal crystallization curves for sample C5 as a function of residence time is shown in Figure IV-1. The curves are sigmoidal and the values are generally in agreement with a previous study by Spruiell et al. (128). As can be seen in Figure IV-1, no measurable increase in crystallinity was detected for temperatures below 100°C even at long residence times. This result confirms that the structure developed in the stretched film samples is a result of stress-induced crystallization and not due to the

TABLE IV-2

AVERAGE REFRACTIVE INDICES OF CAST SHEET SAMPLES

Sample	Thickness μm	(mil)	Refractive Index n_1	n_2	n_3	n_{iso}
C1	279	(11)	1.5782	1.5778	1.5765	1.5775
C2	483	(19)	1.5781	1.5771	1.5768	1.5773
C3	762	(30)	1.5780	1.5763	1.5755	1.5766
C4	965	(38)	1.5770	1.5758	1.5746	1.5758
C5	1067	(42)	1.5800	1.5721	1.5700	1.5740

TABLE IV-3

BIREFRINGENCE RESULTS ON CAST SHEET

Sample	Thickness μm (mil)	Birefringence $\Delta n_{12} \times 10^3$	$\Delta n_{13} \times 10^3$	$\Delta n_{23} \times 10^3$
C1	279 (11)	0.4	1.7	1.3
C2	463 (19)	1.0	1.3	0.3
C3	762 (30)	1.7	2.5	0.8
C4	965 (38)	1.2	2.4	1.2
C5	1067 (42)	7.9	10.0	2.1

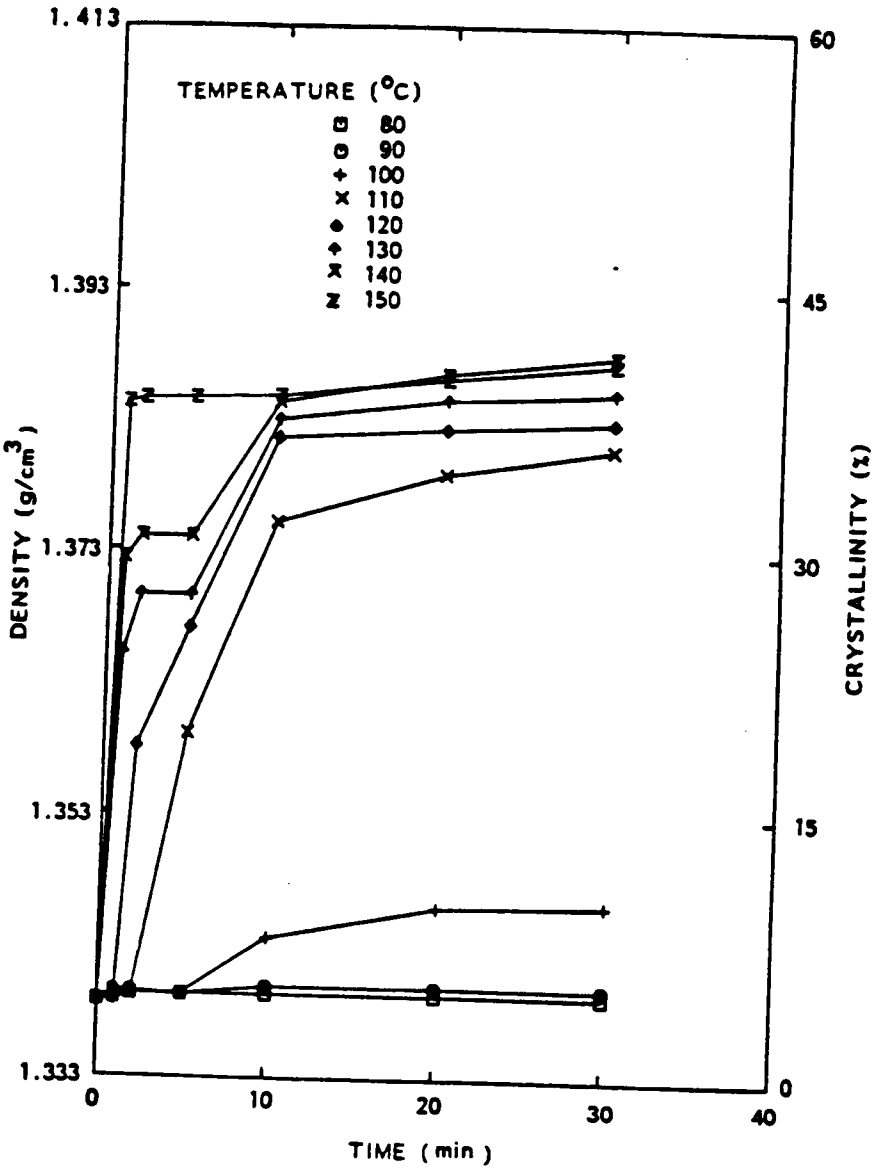


Figure IV-1. Effect of residence time on crystallization of cast sheet sample C5.

deformation of crystallites present in the original cast sheet.

B. NONGRADIENT DRAWN FILMS

a. Drawing Behavior

In order to study the influence of temperature and strain rate on drawing behavior, force versus elongation curves were recorded during stretching. Stretching conditions are listed in Table III-3 (see Chapter III, page 104). Figure IV-2, shows stress versus strain curves for uniaxial film NGB. Similar curves for UCW film sample NGB are shown in Figure IV-3. In all instances, the magnitude of the stress increased with strain rate and decreased with temperature. Spruiell et al. (128) also observed two deformation regimes for PET tensile bars drawn at temperatures above the glass transition. One regime occurred at low strain rates and produced little orientation and crystallinity while the other regime was observed at high strain rates and resulted in the formation of samples having high levels of orientation and crystallinity.

b. Density

Densities and corresponding percent crystallinities for uniaxial and UCW films NGA and NGB plotted as a function of temperature are shown in Figure IV-4. In all cases crystallinity increases with strain rate except in the interval between 100^{o}C and 110^{o}C at low strain rates;

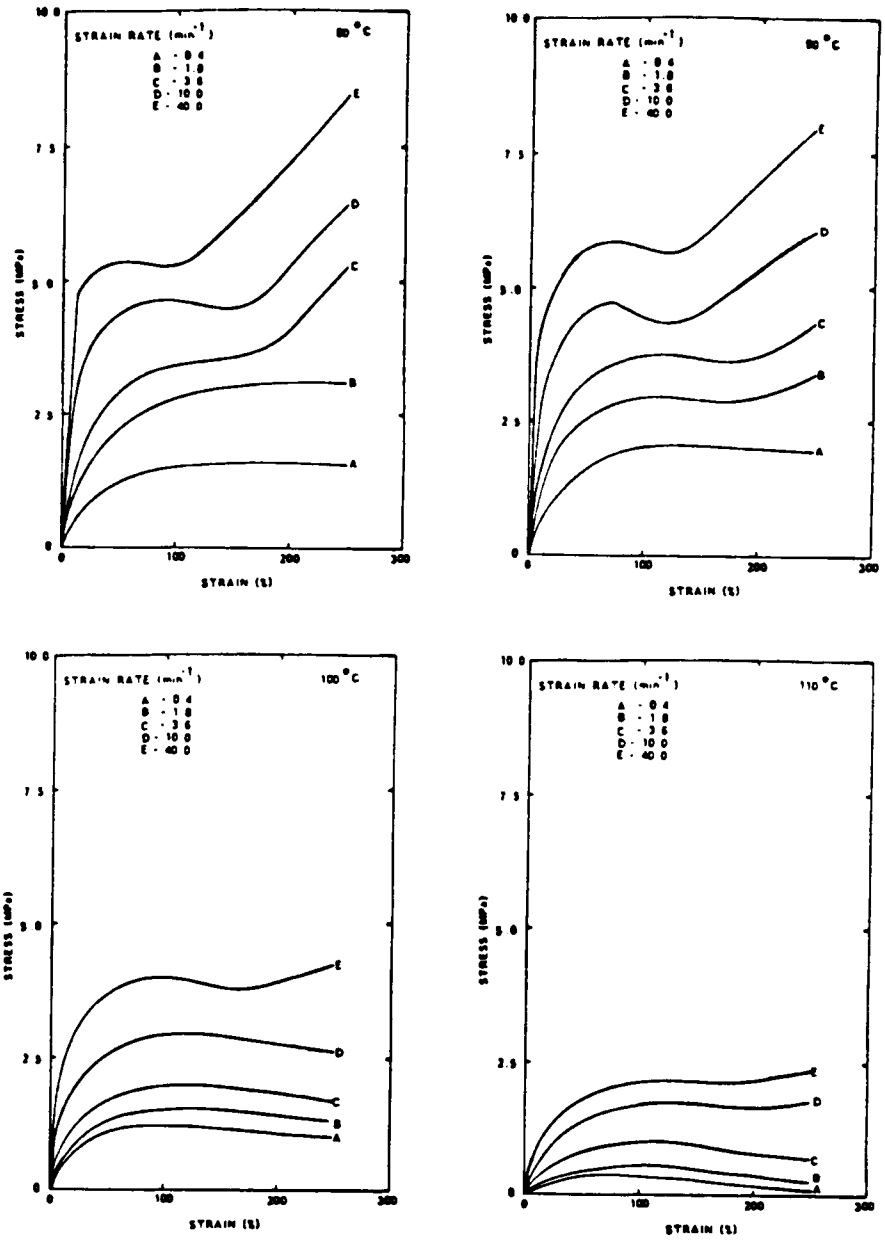


Figure IV-2. Stress--strain curves for uniaxial film NGB as a function of strain rate at various temperatures.

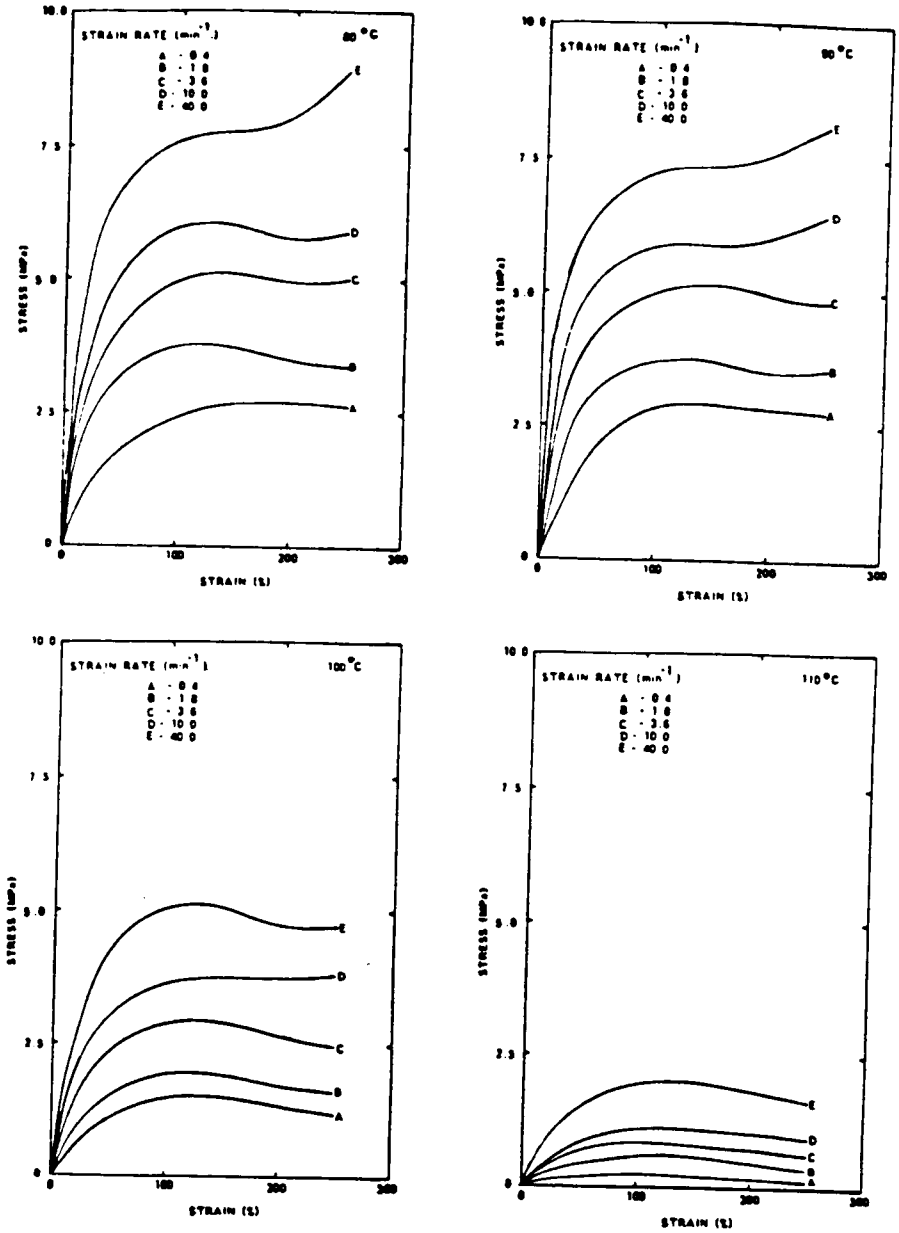


Figure IV-3. Stress--strain curves for UCW film NGB as a function of strain rate at various temperatures.

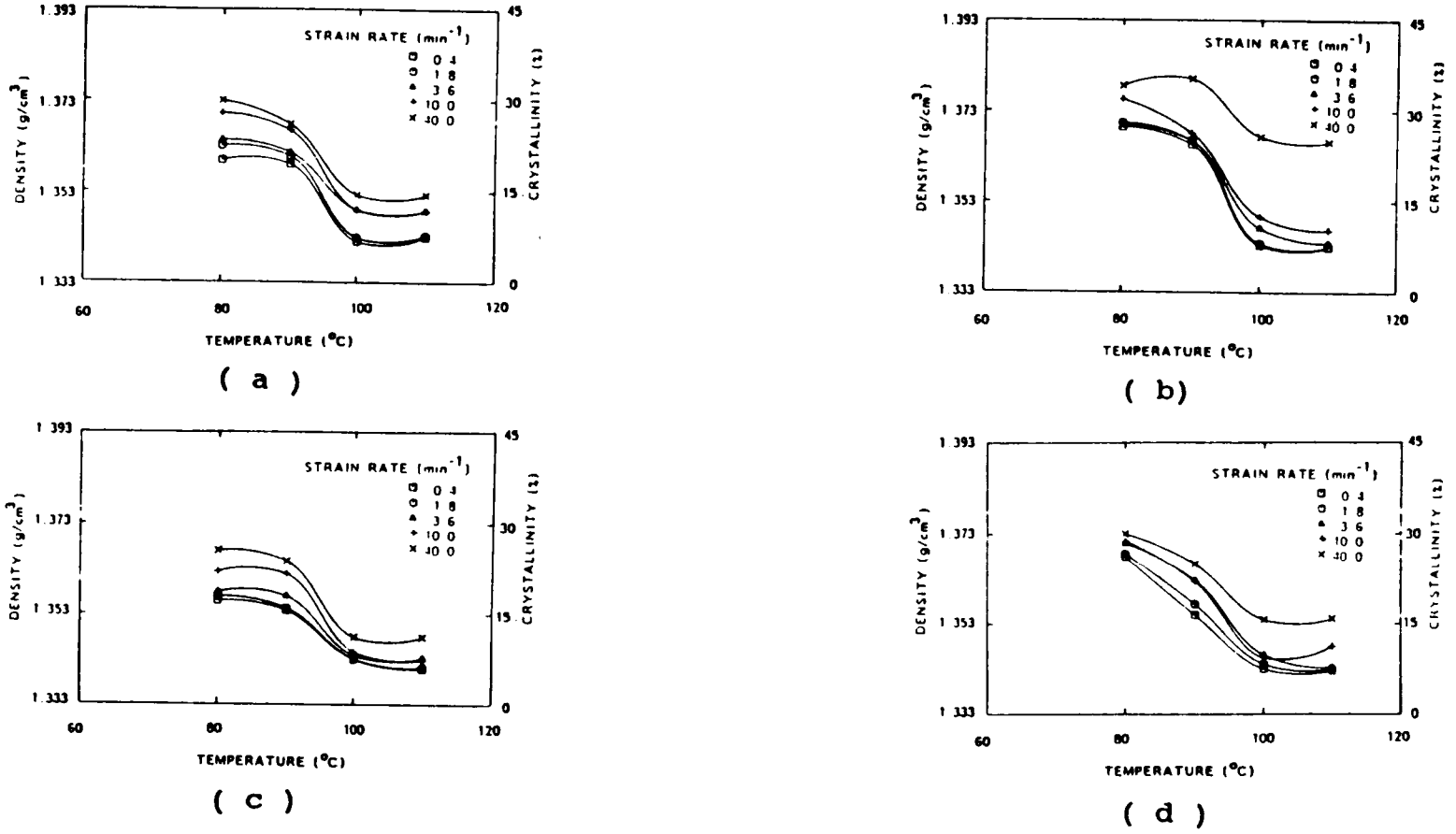


Figure IV-4. Effect of temperature on crystallization of stretched films: (a) uniaxial NGA; (b) uniaxial NGB; (c) UCW NGA and (d) UCW NGB at various strain rates.

however, notice the sharp increase at high strain rates. Corresponding curves showing the influence of strain rate are plotted in Figure IV-5. The difference in crystallinity for both uniaxial and UCW thin films (sample NGA) and for thick films (sample NGB) may be related to the slower quench rate for the thick samples. However, the difference is more likely a reflection of the slightly higher degree of orientation present in the cast sheet from which the thick films were prepared. In all cases, maximum values were obtained for films drawn in the range between 80°C to 90°C.

c. Birefringence

Birefringence represents a measure of the overall degree of orientation present within a film. Birefringence values were calculated from refractive index measurements made on the central portion of drawn film samples. In-plane Δn_{12} and out-of-plane Δn_{13} and Δn_{23} birefringences plotted as a function of temperature for uniaxial and UCW films NGA and NGB are shown in Figures IV-6 and IV-7 respectively. In all cases, maximum values were observed for films drawn at 80°C. As can be seen in Figures IV-6 and IV-7, temperature has a strong effect on birefringence. The effect of strain rate is shown in Figures IV-8 and IV-9. Strain rate becomes increasingly significant at high temperatures. Notice the sharp increase at strain rate of 40.0 min^{-1} even at temperatures in excess of 100°C.

The existence of a critical stress has been observed by

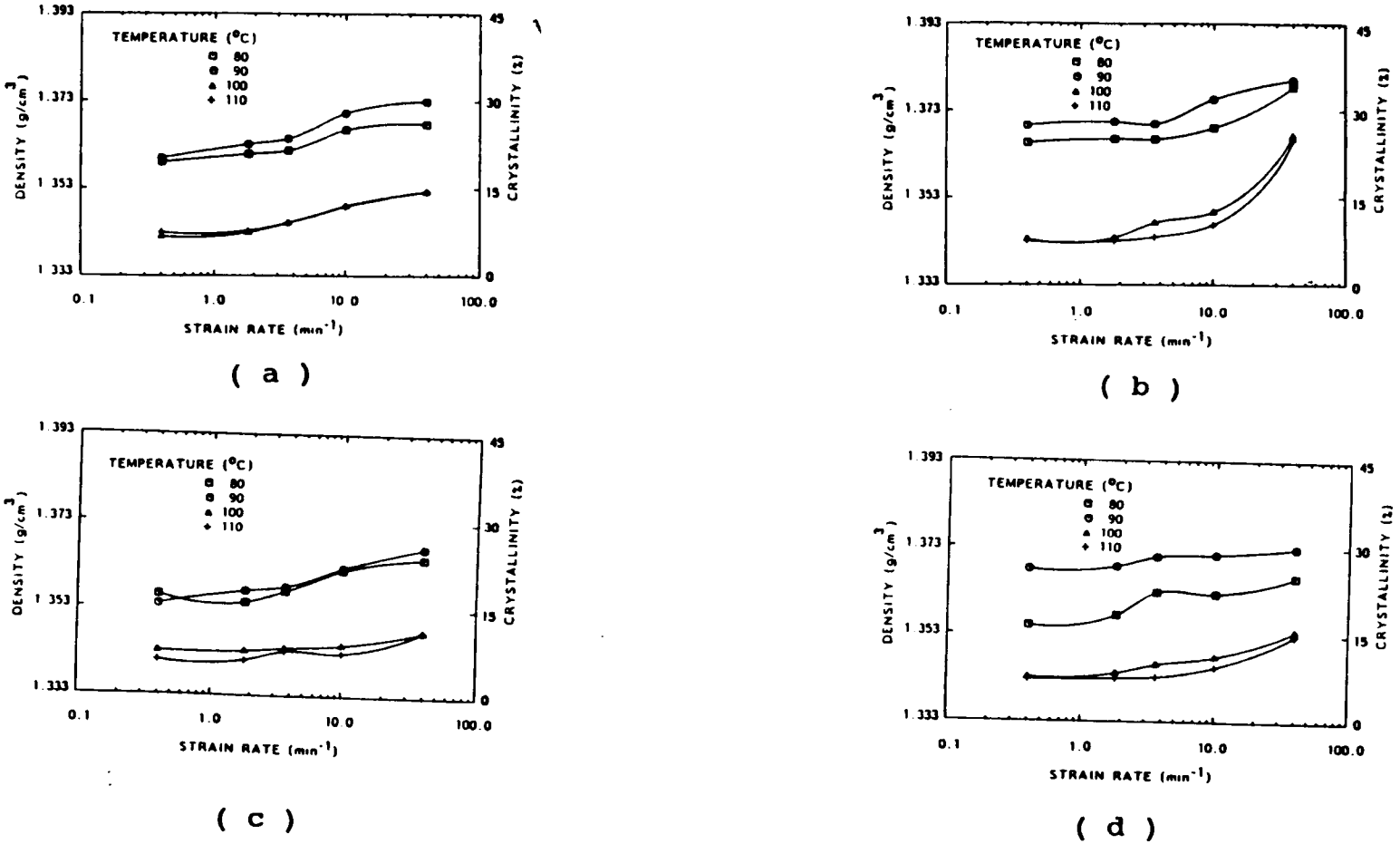
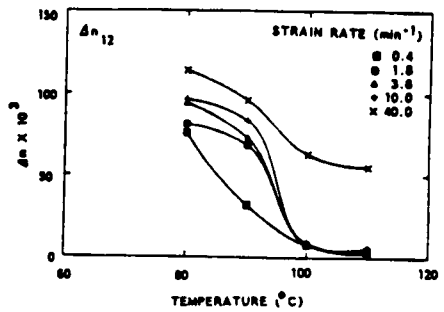
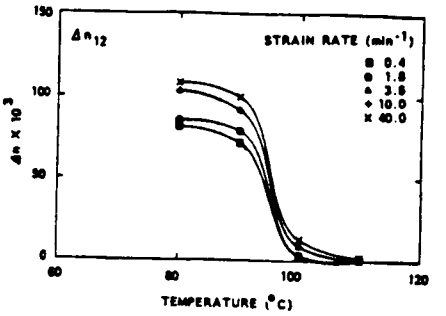
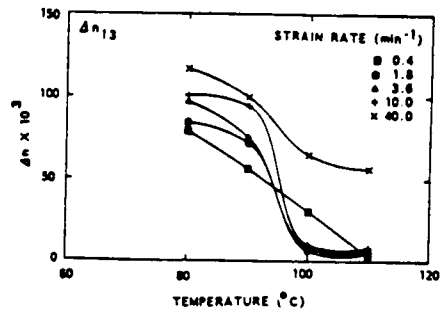
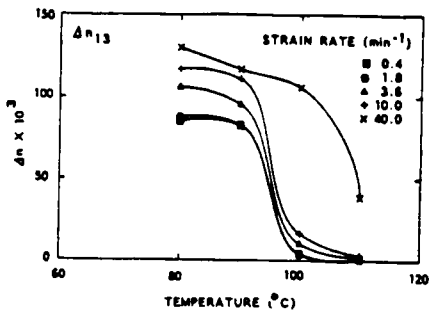


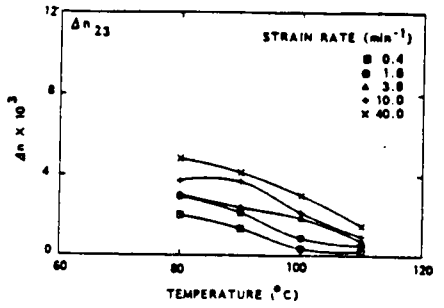
Figure IV-5. Effect of strain rate on crystallization of stretched films: (a) uniaxial NGA; uniaxial NGB; (c) UCW NGA and (d) UCW NGB at various temperatures.

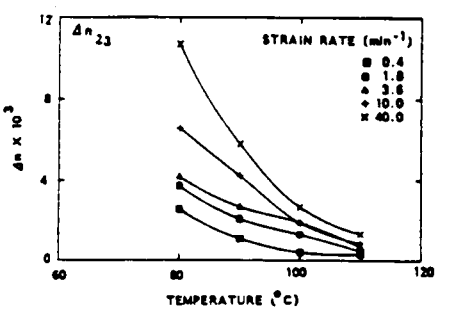












(a) (b)

Figure IV-6. Variation of birefringence with temperature for uniaxial films: (a) NGA and (b) NGB.

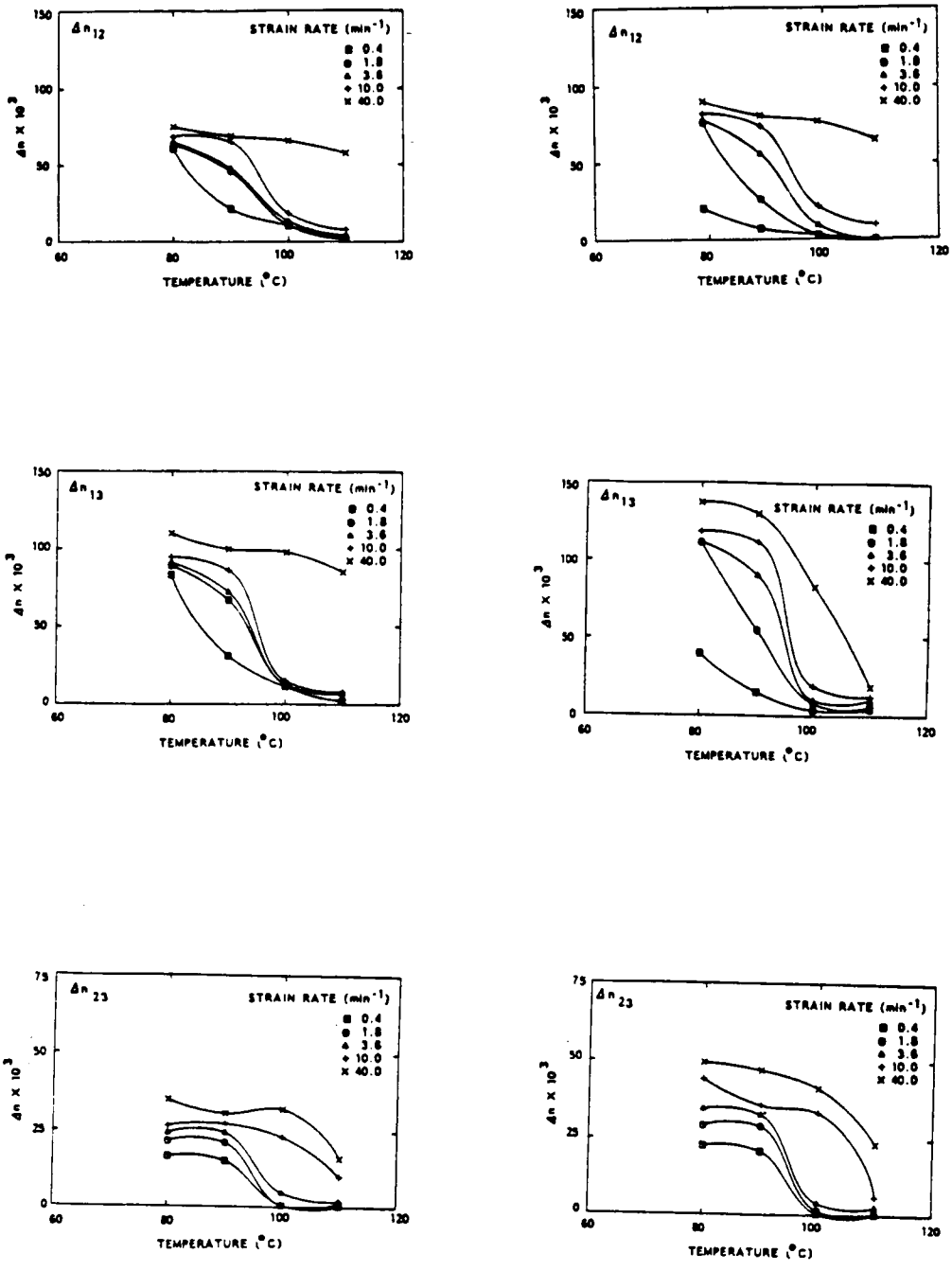


Figure IV-7. Variation of birefringence with temperature for UCW films: (a) NGA and (b) NGB.

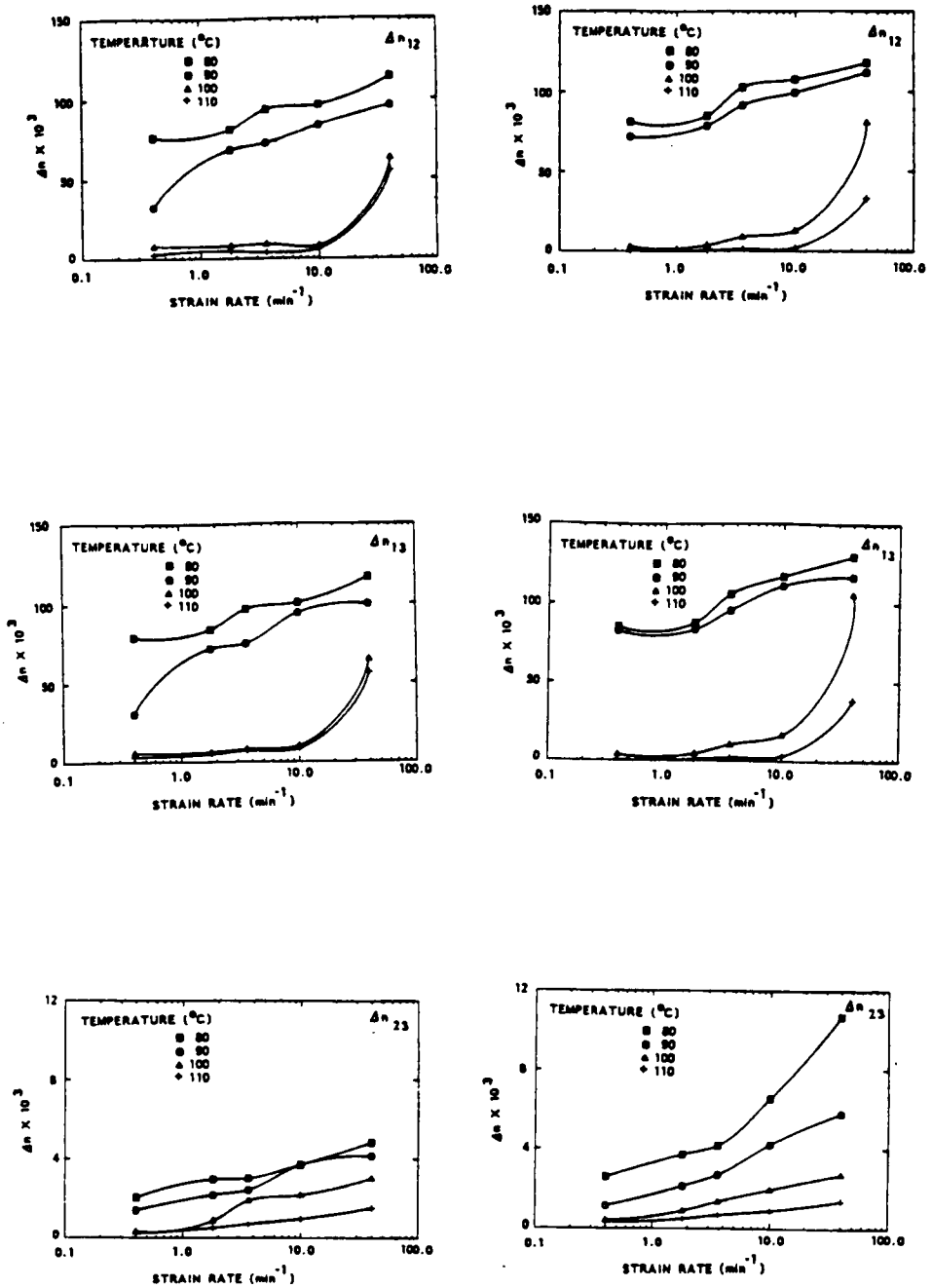


Figure IV-8. Variation of birefringence with strain rate for uniaxial films: (a) NGA and (b) NGB.

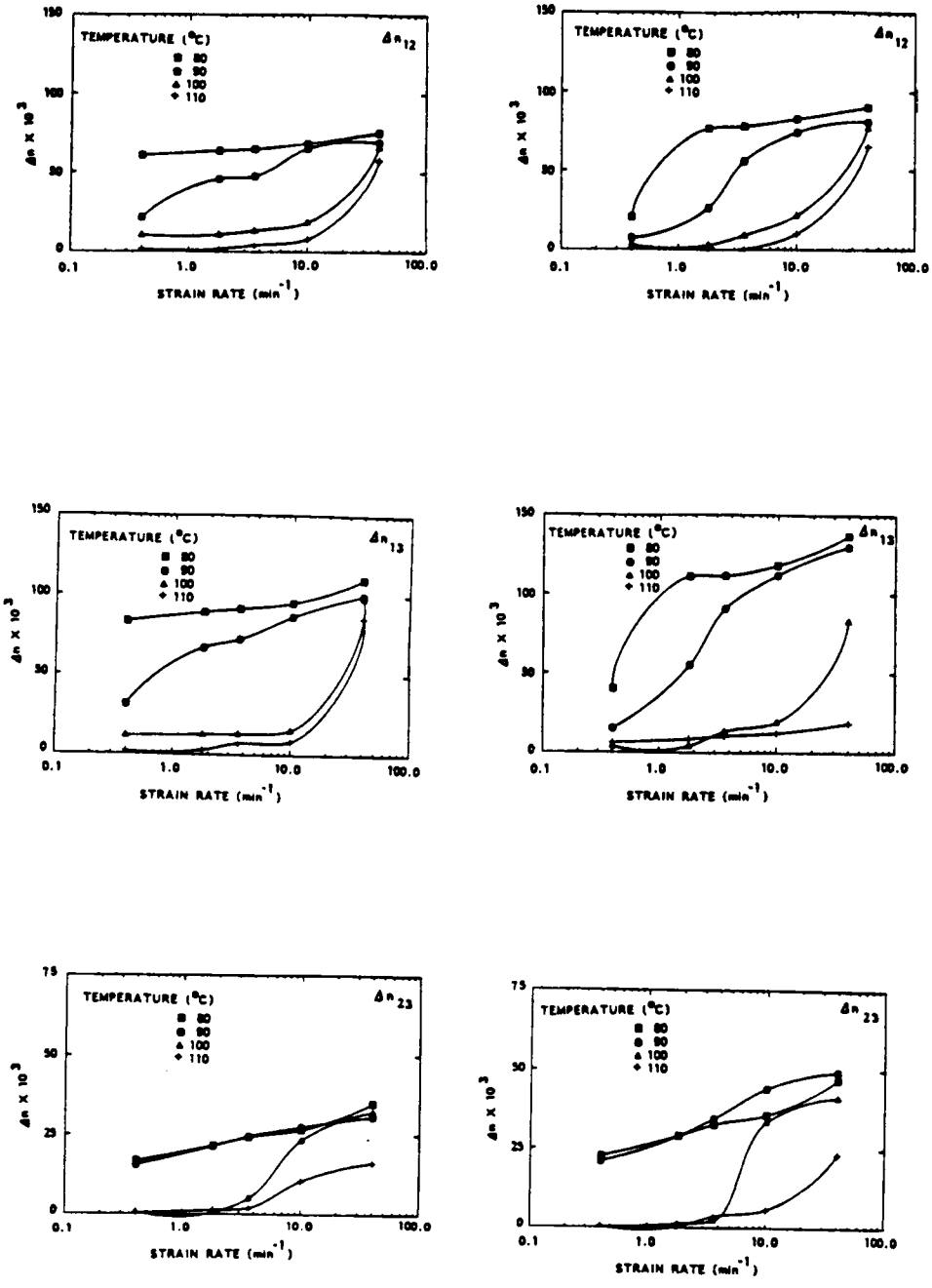


Figure IV-9. Variation of birefringence with strain rate for UCW films: (a) NGA and (b) NGB.

several previous investigators. Recently Hinrichsen and coworkers (56) produced films with little, if any, molecular orientation by drawing PET films between 95°C and 110°C at low strain rates.

d. Small-Angle Light Scattering

The scattering of light from polymer films arises from the interaction of light with heterogeneities having dimensions comparable to the wavelength of light (135). The heterogeneities are regions of different density or fluctuations in refractive index. The deformation mechanism and superstructure produced in drawn films was studied by using the conventional photographic SALS technique. The objective of the experiment was to qualitatively detect the dependence of film morphology on temperature and strain rate.

Scattering patterns were obtained with polarizer and analyzer parallel (V_v) and perpendicular (H_v). The effect of temperature on H_v patterns for uniaxial film NGB drawn at 10.0 min^{-1} is shown in Figure IV-10. The patterns consist of four broad lobes at small azimuthal angles and four narrow streaks at large azimuthal angles. The stretch direction in all cases is taken to be vertical. The origin of the scattering patterns is attributed to stress-induced crystallization. The shape of the patterns has been suggested to represent the growth of sheaf-like

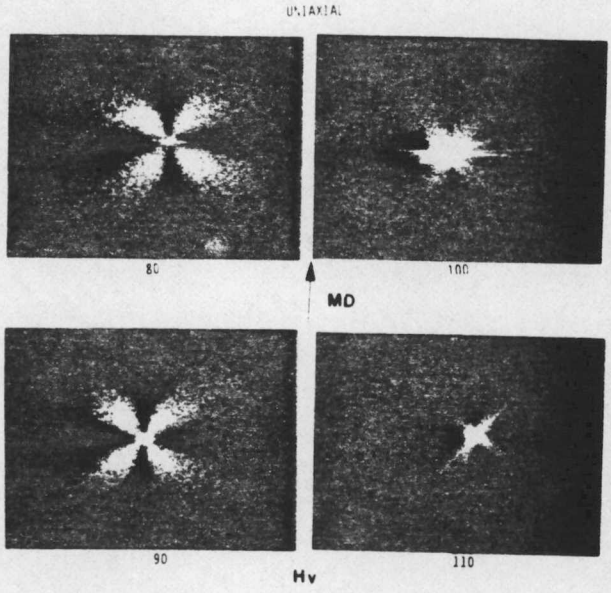


Figure IV-10. Effect of temperature on H_v patterns for uniaxial film NGB drawn at 10.0 min^{-1}.

superstructures. The sharp narrow streaks have been shown to be dependent on the degree of crystallinity (87).

The influence of strain rate on H_v and V_v patterns for film sample NGB stretched at 80°C is shown in Figure IV-11. In general the patterns reveal an increase in crystallinity and orientation with strain rate. An examination of the patterns in Figures IV-10 and IV-11, reveals that the broad lobes are inclined at an angle of 45 degrees or more to the stretch direction. The inclination of the broad lobes is interpreted by Matsuo (73) to be related to the orientation of the sheaf-like superstructure to the deformation direction.

C. COMPARISON OF NONGRADIENT AND GRADIENT DRAWN FILMS

a. Heat Transfer Theory

The study of heat transfer in this section is limited to predicting the average temperature of PET cast sheet prior to stretching. The general equation describing transient heat conduction in an isotropic solid with heat generation is given by

$$\partial T / \partial t = \alpha \nabla^2 T + g \qquad \text{(IV-2)}$$

Considering only one-dimensional transfer, neglecting the internal heat generation term, g, and assuming constant thermal properties Equation IV-2 reduces to

$$\partial T / \partial t = \alpha \partial^2 T / \partial x^2 \qquad \text{(IV-3)}$$

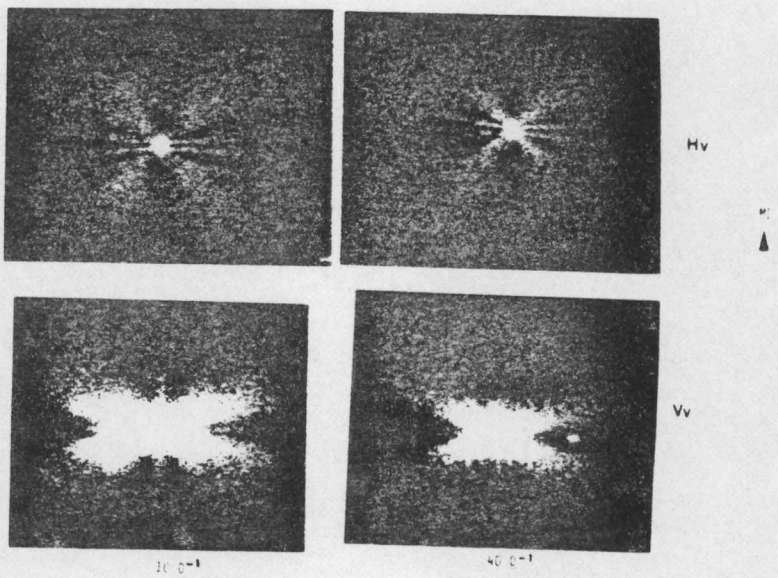


Figure IV-11. Effect of strain rate on H_v and V_v patterns for uniaxial film NGB1.

where α is the thermal diffusivity ($\alpha = k / \rho C_p$), k is the thermal conductivity, ρ is the density and C_p is the heat capacity. The values used for PET cast sheet are given in Table IV-4.

Convective boundary conditions are specified by

$$-k_1 \left(d T / dx \right) = h_1 \left(T_a - T \right) \qquad \text{(IV-4)}$$

$$k_2 \left(d T / d x \right) = h_2 \left(T - T_a \right) \qquad \text{(IV-5)}$$

where T_a is the ambient (air stream) temperature.

The solution of Equation IV-3 subject to the boundary conditions given by Equation IV-4 and IV-5 can be obtained by using numerical methods. The Crank-Nicolson method (21) was chosen because of its stability and minimal programming requirements. This method replaces the derivatives in Equations IV-3, IV-4 and IV-5 with approximations in the form of finite-sized differences between values at particular points. A detailed derivation of the finite difference equations and application of the technique is presented by Croft and Lilley (21) and Ozisik (94). A complete listing of the actual computer program used to generate profiles in cast sheet is given in the Appendix.

Predicted average temperatures as a function of residence time in the heating chamber are listed in Table IV-5. Values shown are for an experimentally

TABLE IV-4

THERMAL PROPERTIES OF PET

Parameter	Value	Units	Reference
ρ	1.338	g / cm^3	*
k	3.7×10^4	(cal / g) / (s cm^2 ^oC)	12
C_p	3.0×10^1	cal / (g ^oC)	12
h	4.1×10^{-4}	cal / (s cm^2 ^oC)	*

* - Experimentally determined values.

TABLE IV-5

INFLUENCE OF RESIDENCE TIME ON THE PREDICTED AVERAGE TEMPERATURES IN CAST SHEET SAMPLE C5

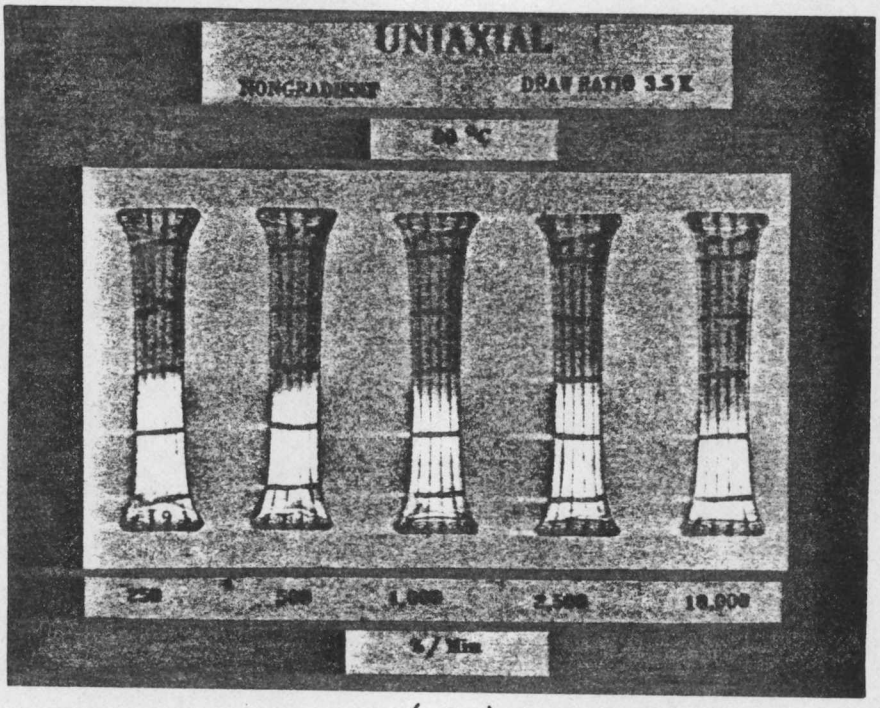
Residence Time (min)	T_{avg} (°C)	ΔT (°C)
0.5	25.24	0.69
1.0	53.63	2.85
1.5	70.45	2.85
2.0	80.43	2.85
2.5	86.35	2.85
3.0	89.88	2.85
0.5	25.26	1.39
1.0	55.68	5.70
1.5	73.70	5.70
2.0	84.39	5.70
2.5	90.74	5.70
3.0	94.52	5.70

determined heat transfer coefficient of 4.1 X 10^{-4} cal/ (s cm^2 ^oC) (3.2 BTU/(hr ft^2 ^oF), this value seems reasonable but perhaps it is slightly higher than the true value.

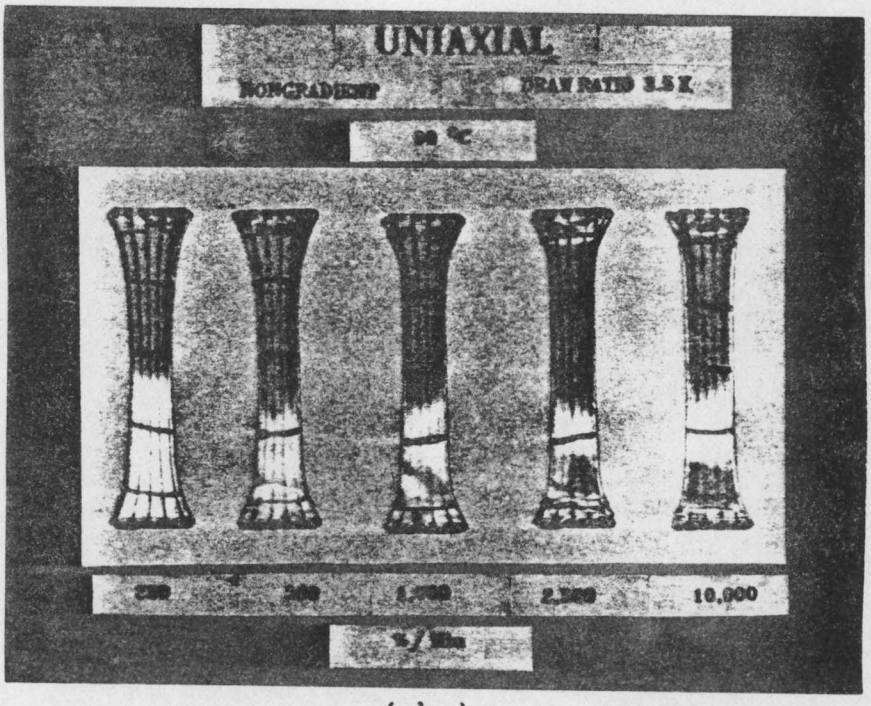
b. Deformation Behavior

The macroscopic deformation behavior of nongradient uniaxial films NGB1 and NGB2 is shown in Figure IV-12. Figure IV-13 shows the stretched films GA3 and GB3. Similar behavior was observed in UCW samples NGB1 and GA3 as can be seen by comparing the samples in Figure IV-14a with those in IV-14b. The most obvious aspect is the poor quality of the gradient samples. Observe the nonhomogeneous drawing as evidenced by the necking and different draw ratios.

Foster and Hook (35) have shown that stress-induced crystallization is a major source of heat generation in PET during drawing. Any heat generated during deformation whether due to crystallization or the result of viscous deformation would be expected to have a significant effect on stress strain behavior. Furthermore, any heat generated would alter the superimposed profile in a gradient film. As can be seen in Figures IV-13 and IV-14b, the overall degree of inhomogeneity decreases substantially with increasing strain rate. For high strain rates the film can be considered to be almost adiabatic, with little heat transfer to the surrounding air. Comparing uniaxial nongradient film samples NGB1 (80^oC) and NGB2 (90^oC) and gradient films drawn at high strain rates, little difference in the overall

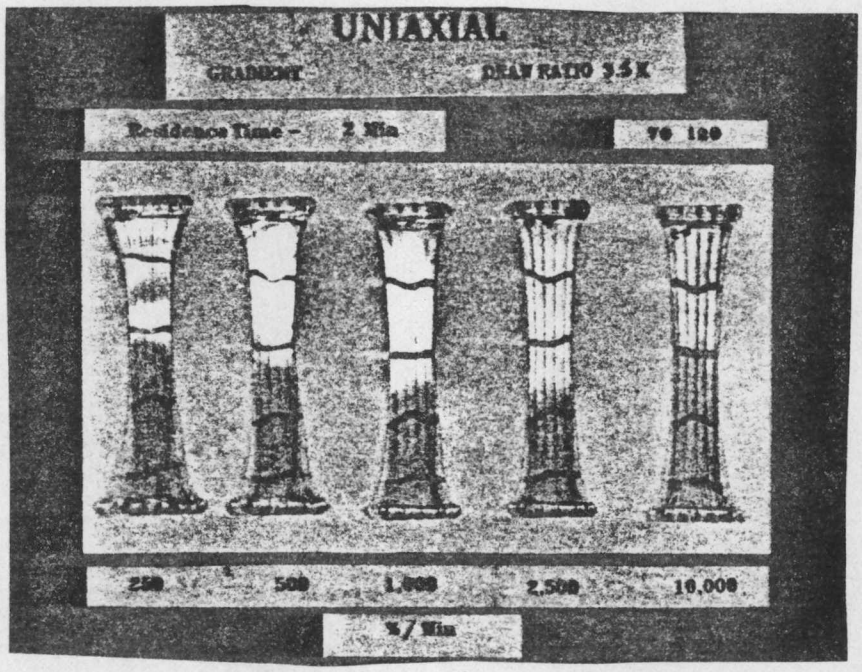


(a)

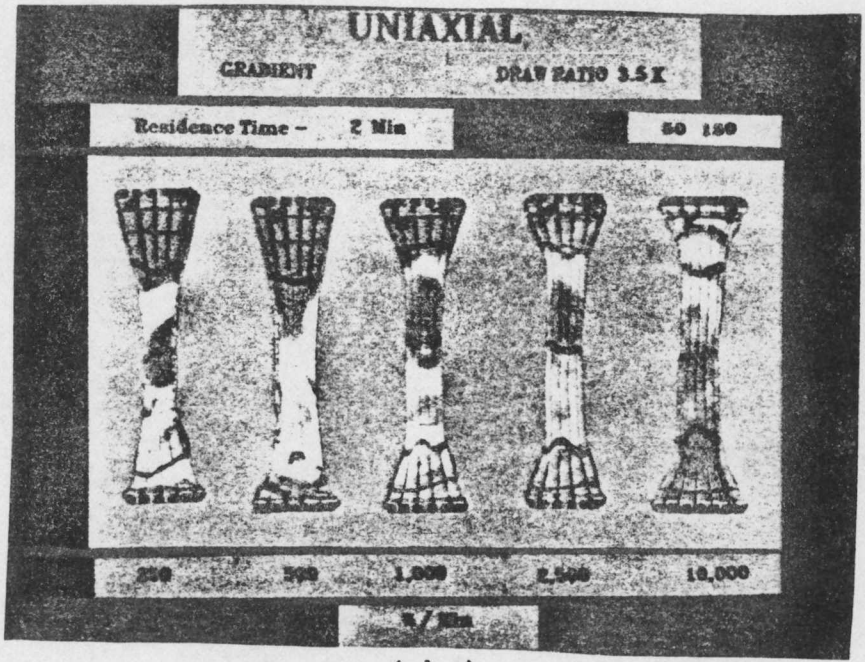


(b)

Figure IV-12. Photographs of nongradient uniaxial films: (a) NGB1 and (b) NGB2.

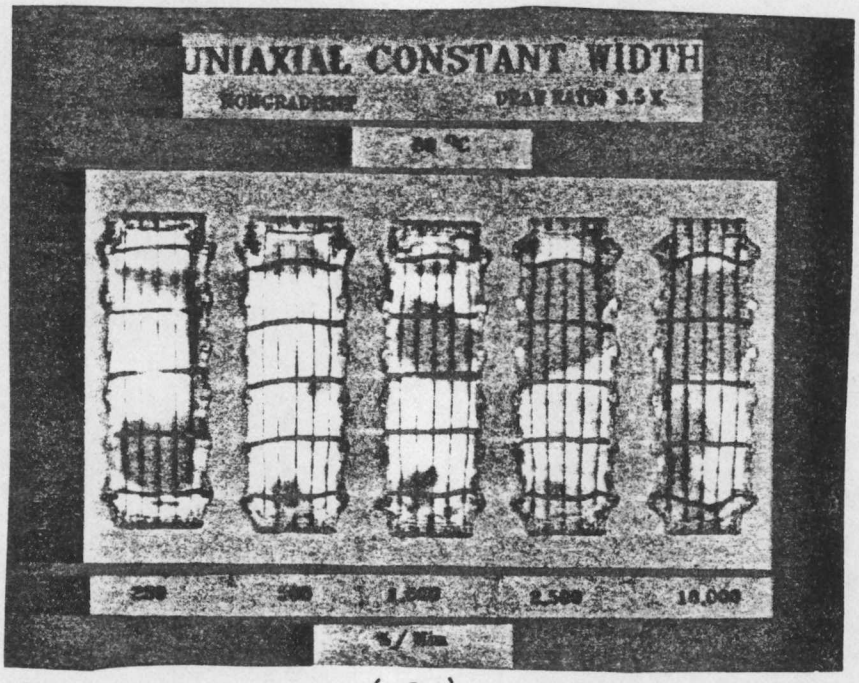


(a)



(b)

Figure IV-13. Photographs of gradient uniaxial films: (a) GA3 and (b) GB3.



(a)



(b)

Figure IV-14. Photographs of nongradient and gradient UCW films: (a) NGB1 and (b) GA3.

macroscopic degree of deformation can be observed. Stress--strain curves for uniaxial films GA3 and GB3 are shown in Figure IV-15 and IV-16 respectively. Notice the increase in stress with high strain rates, this is an indication of substantial stress-induced crystallization.

c. Birefringence

An attempt was made to correlate average properties with predicted average temperatures obtained from heat transfer theory for gradient films. The results are shown in Table IV-6. Birefringence and crystallinty values are in relatively good agreement with average temperatures predicted by heat transfer theory. In general, the values fall within the range of values for nongradient films. The small differences are most likely a result of the assumptions and errors involved in the heat transfer analysis and a reflection of the small through the thickness temperature gradient existing in the cast sheet prior to drawing.

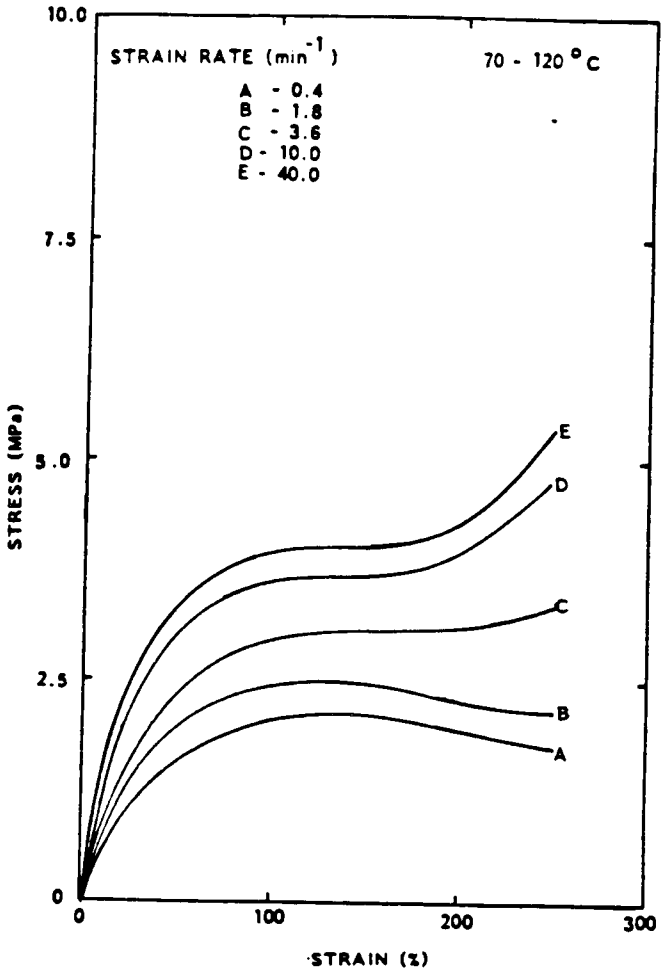


Figure IV-15. Stress--strain curves for gradient uniaxial film GA3.

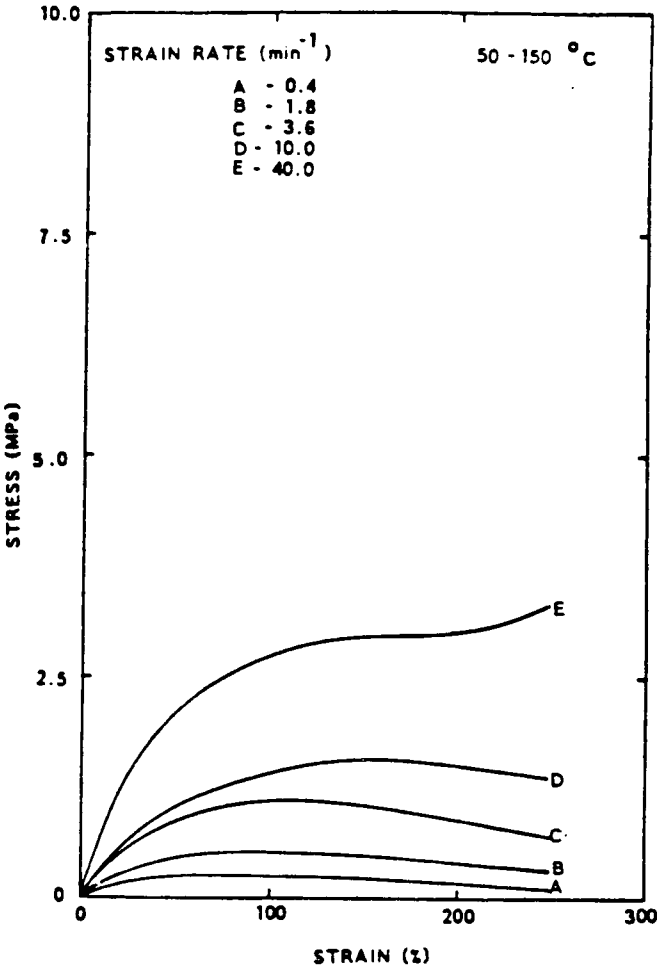


Figure IV-16. Stress--strain curves for gradient uniaxial film GB3.

TABLE IV-6

COMPARISON OF NONGRADIENT AND GRADIENT DRAWN FILMS

T (^{o}C)	$\Delta n_{12} \times 10^3$	$\Delta n_{13} \times 10^3$	$\Delta n_{23} \times 10^3$
	Nongradient Uniaxial Film NGB		
80	99.4	104.0	4.6
90	86.2	89.9	3.7
100	8.0	10.2	2.2
110	3.1	4.1	1.0
	Gradient Uniaxial Film GA3[a]		
Cold (79.0)	110.0	115.0	5.0
Hot (82.0)	106.5	111.1	4.6
Avg (80.5)	108.3	113.1	4.8
	Gradient Uniaxial Film GB3[b]		
Cold (82.1)	87.5	89.9	2.3
Hot (86.1)	115.3	118.2	2.9
Avg (84.1)	101.4	104.0	2.6

a -- Air Stream Temperatures: $T_H = 120^{o}C$, $T_C = 70^{o}C$

b -- Air Stream Temperatures: $T_H = 150^{o}C$, $T_C = 50^{o}C$

All Films Drwan at 10.0 min^{-1}.

CHAPTER V

CHARACTERIZATION OF DRAWN FILMS: THROUGH THE THICKNESS VARIATIONS

A. CHARACTERIZATION TECHNIQUES

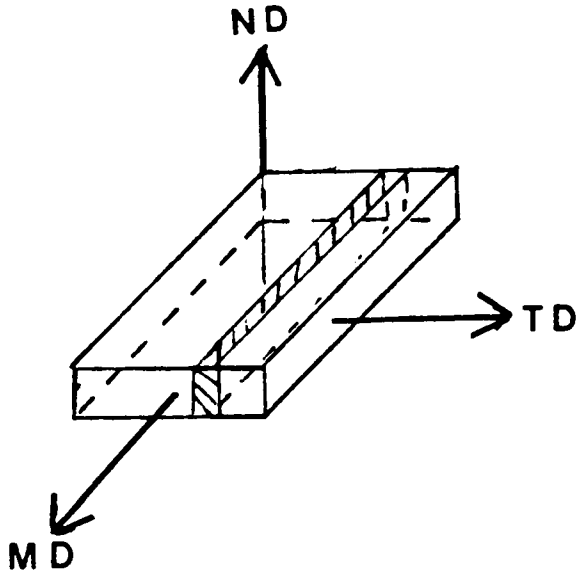
Few techniques are available for directly investigating inhomogeneity through the thickness of oriented films. Inhomogeneity can best be described as regions of different density, morphology or orientation or a combination of all three at various points within the film. A variety of experimental techniques were utilized in an attempt to characterize through the thickness variations in orientation and structure. The advantages and limitations associated with each technique are discussed.

a. Birefringence

The simplest and most commonly used technique for measuring birefringence is the compensator method. Numerous studies have used this method to obtain birefringence profiles through the thickness of polymer slabs (114,152). For the purpose of this research, thick PET cast sheet will be considered to be a slab. Practically, however, thick PET moldings are not quenched to an amorphous state but rather the crystallization behavior of the material is controlled by the addition of nucleating agents (52).

In the chill-roll cast film process, the extrusion of molten polymer onto a cold metal roll produces a thermal gradient through the thickness. One of the major steps in the production of oriented PET film involves extrusion of molten PET at 290^{o}C directly onto an internally cooled casting roll. Since only one surface of the sheet contacts the chill roll, the quench conditions for each surface are different. The surface in direct contact with the roll solidifies almost instantaneously, whereas the side exposed to the air cools slowly. In the case of thick films, there is a sharp temperature gradient through the thickness, a consequence of the poor thermal conductivity of the polymer. Since thermal conductivity is a material property, the heat transfer coefficient would be expected to be the controlling factor in determining the severity of the gradient.

To demonstrate the simplicity and utility of the compensator technique, thick slabs of PET were prepared by rapidly quenching thick moldings in ice water. Specimens for birefringence measurements were cut from quenched slabs as shown in Figure V-1. Retardation was measured as a function of through the thickness position to determine the magnitude of any residual stresses produced during quenching. Wust (152) prepared polystyrene samples essentially free of stress by allowing the slabs to cool slowly. Birefringences of sections cut from the stress-free slabs were found to be zero throughout the sections except



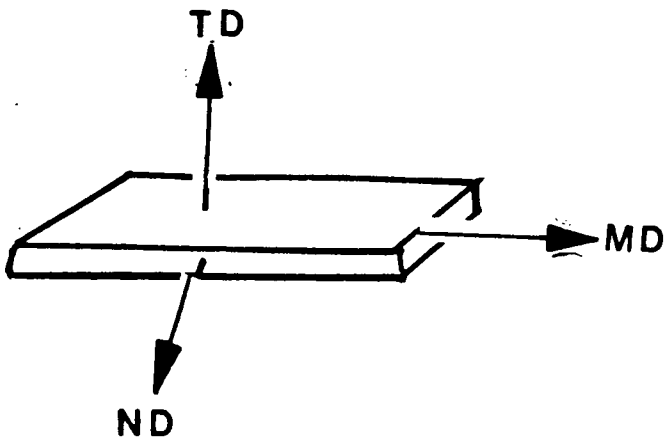


Figure V-1. Cross section of slab film used for birefringence measurements.

at the unpolished edges. This observation led Wust to conclude that the cutting technique used to prepare sections for birefringence measurements did not introduce any additional stresses in the sample. Similar samples cannot be prepared from PET because unlike polystyrene the material will crystallize if allowed to cool slowly. A birefringence profile for a 0.125 in. slab quenched in ice water is shown in Figure V-2. The magnitude of the birefringence is small, an indication that the stresses present in the sample are small. As can be seen in Figure V-2, the profile is not flat, this is due to the poor thermal conductivity of the polymer. Since homogeneous stress-free samples cannot be obtained for PET no further investigation was attempted.

The technique has also been used to study the variation of birefringence through the thickness of semicrystalline polymers. Roylance and Roylance (114) measured birefringence distributions in rolled polypropylene. In an attempt to extend the technique to thin PET films, retardation was measured at three positions across the thickness of a microtomed cross section of cast sheet sample C5. As shown in Table V-1, the values are in rough agreement with those obtained by the Abbe' refractometer method. The slightly higher values for the sample used in the compensator method may be related to stressess produced during sectioning. In-plane birefringences for cast sheet

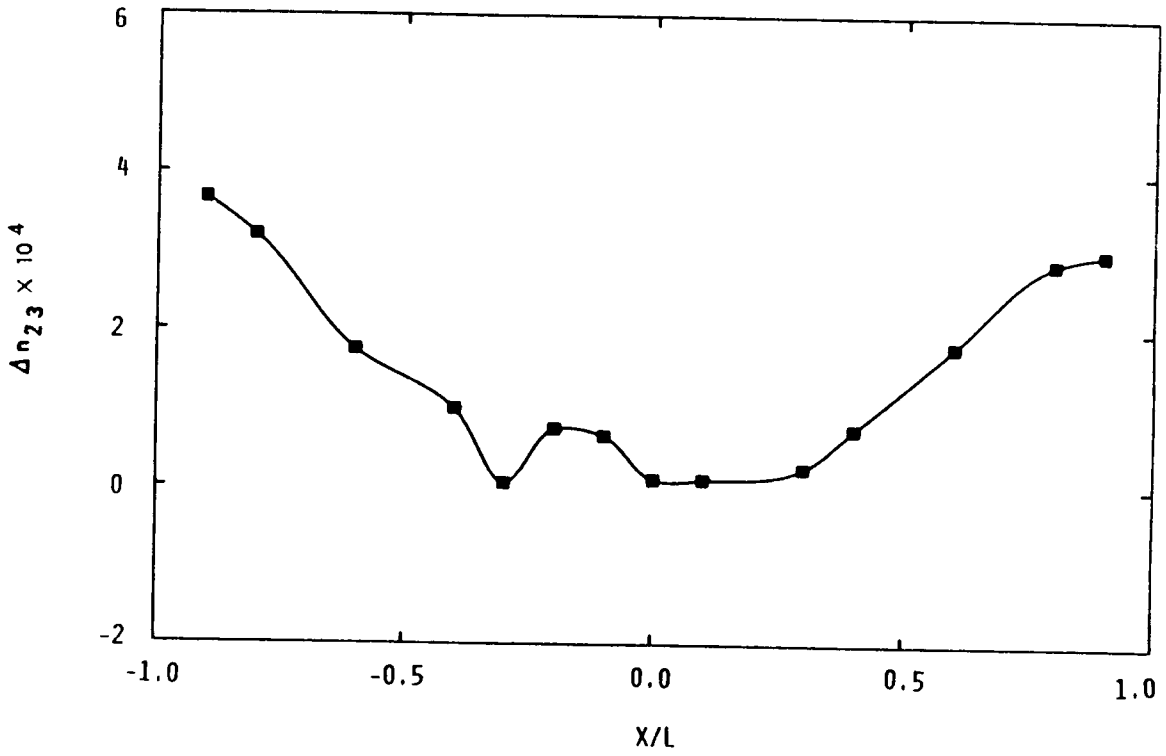


Figure V-2. Birefringence profile for a (0.125 in.) PET slab quenched from the melt (290°C) in ice-water.

TABLE V-1

THROUGH THE THICKNESS BIREFRINGENCE VALUES
FOR CAST SHEET SAMPLE C5

Position	Compensator Method $\Delta n_{12} \times 10^3$	Abbe' Method $\Delta n_{12} \times 10^3$
1	13.0	8.4
2	12.0	---
3	13.0	7.5

samples are shown in Table V-2. All samples are slightly oriented.

The major limitation of the compensator methods is the need to measure thickness of the specimen at the point where retardation is measured. The ability to accurately measure thickness becomes prohibitive as the thickness of the sample decreases. It is also difficult to locate the exact position at which retardation is to be measured with sufficient accuracy in thin samples.

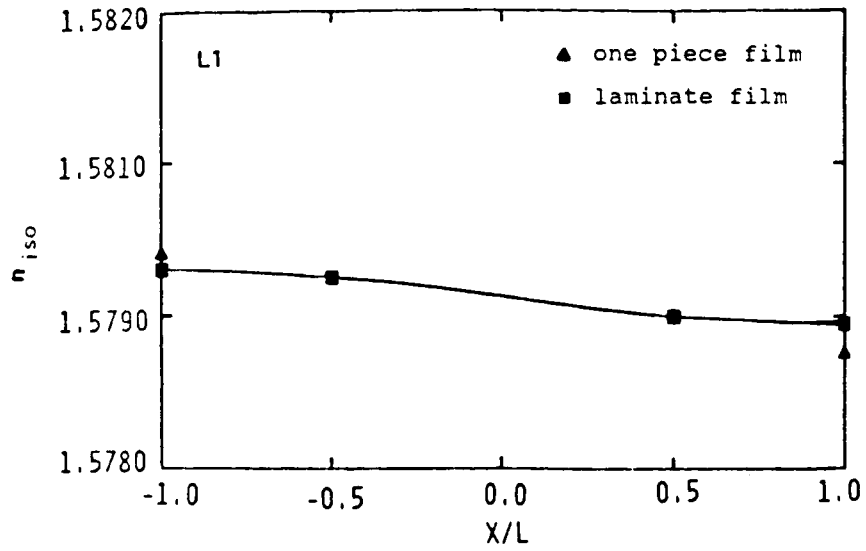
b. Refractive Index

As discussed in Chapter II, the Abbe' refractometer can be used to determine the three principal refractive indices at the surface of a film. To confirm the principle of the technique and to verify the concept of applying the method to the study of through the thickness inhomogeneity, a series of multilayer films were prepared from PET cast sheet using a hot press. The present study is essentially identical to that of Tanaka et al. (137,138) except that PET was substituted for polypropylene. Refractive index profiles for 534 μm (21 mil) and 1068 μm (42 mil) thick multilayer films are shown in Figures V-3 and V-4 respectively. A complete description of the laminate films is given in Table III-2 (see Chapter III, page 99). The profiles plotted in Figure V-4 reflect the unequal cooling rates at opposite surfaces, a consequence of having metal plates of different thicknesses adjacent to each of the

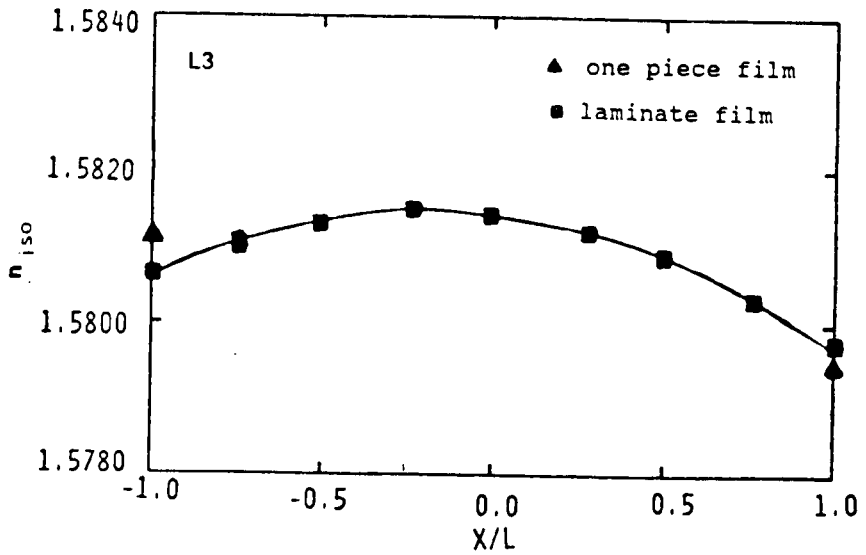
TABLE V-2

BIREFRINGENCE RESULTS ON CAST SHEET SAMPLES USING THE COMPENSATOR TECHNIQUE

Cast Sheet Sample	Thickness μm (mil)	$\Delta n_{12} \times 10^3$
C1	279 (11)	6.0
C2	483 (19)	2.0
C3	762 (30)	7.0
C4	965 (38)	7.0
C5	1067 (42)	6.0

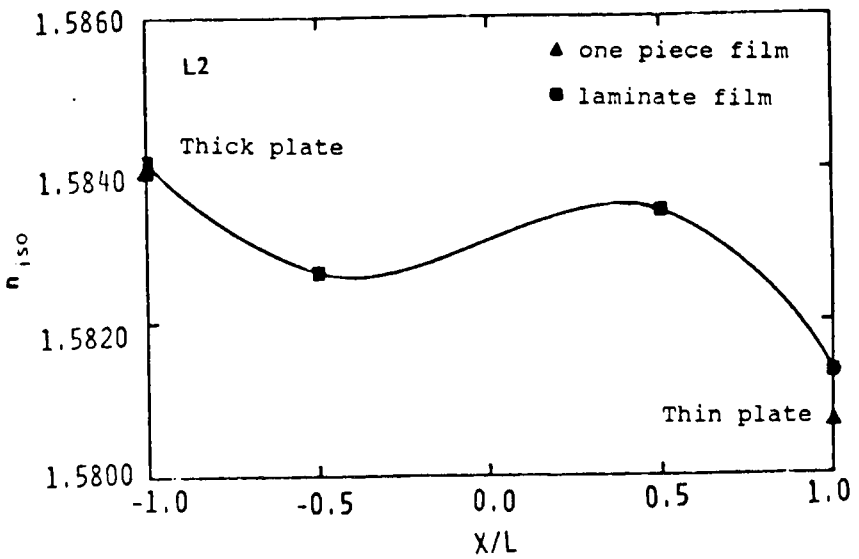


(a)

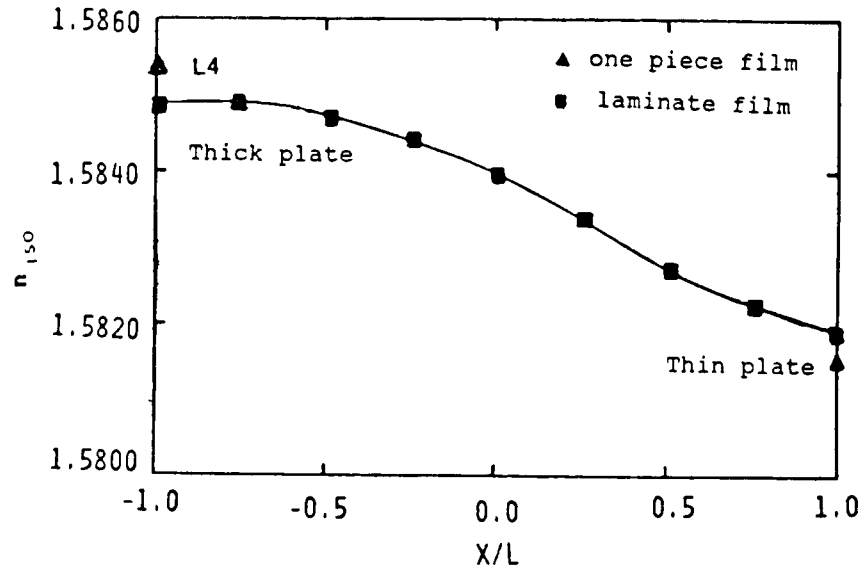


(b)

Figure V-3. Refractive index distribution through the thickness of laminate PET films quenched from the melt (290^{o}C) in ice water:(a) L1 and (b) L3. Equal cooling rates at the outer surfaces.



(a)



(b)

Figure V-4. Refractive index distribution through the thickness of laminate PET films quenched from the melt (290°C) in ice water: (a) L2 and (b) L4. Unequal cooling rates at the outer surfaces.

surfaces. The refractive indices of one piece films prepared under identical quenching conditions are also shown in Figures V-3 and V-4. As can be seen in the profiles, the refractive index values of the surface layers of multilayer films are in relatively good agreement with those measured on one-piece samples. This finding confirms the principle of the operation of the Abbe' refractometer and also serves to warrant applying the technique to the study of through the thickness inhomogeneity.

c. Microscopy

Optical micrographs of microtomed 10 m thick TD cross sections cut from selected nongradient and gradient uniaxial films are shown in Figure V-5. Clearly, as can be seen in the photomicrographs, the sections cut from gradient uniaxial films GA3 and GB3 exhibit significant lateral "chatter marks" and longitudinal knife marks, both related to sample distortion during cutting. In contrast, the sections cut from nongradient uniaxial film NGB3 is comparitively smooth and free from cutting artefacts.

Since the thickness across each section is not uniform no comaprison could be made about variations within a particular section or between sections. It is important to note the poor quality of the section cut from the gradient sample. These cutting artefacts were the major problem in obtaining interference fringe patterns free from distortion. The importance of obtaining high quality (uniform thickness)

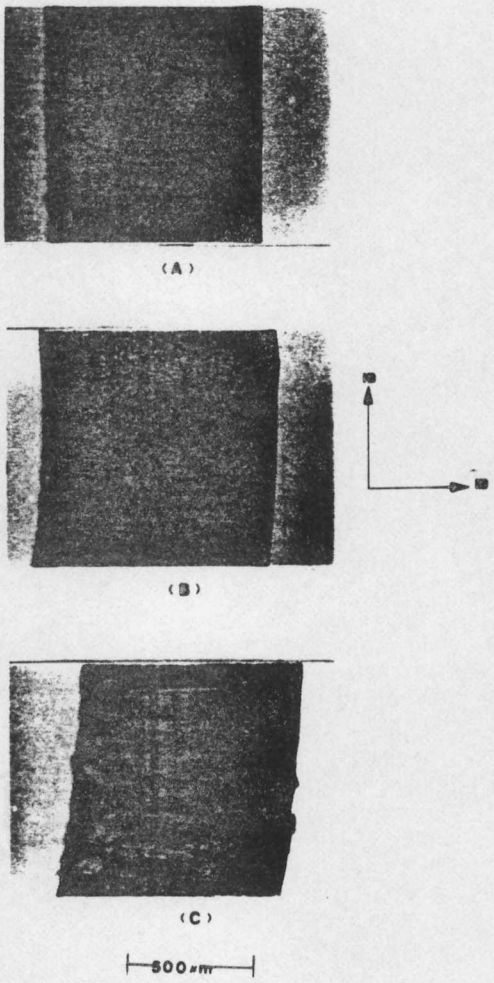


Figure V-5. Optical photomicrographs of TD cross sections of uniaxial stretched films in polarized light: (a) NGB1; (b) GA3 and (c) GB3. All films drawn at 10.0 min^{-1}.

cross sections when preparing samples for interference microscopy must be emphasized.

SEM photomicrographs of TD fracture surfaces for selected films are shown in Figure V-6. Qualitatively, the nongradient films appear to have smoother fracture surface macrostructures than do gradient films. However, no outstanding features are evident in any sample.

B. CAST SHEET AND GRADIENT DRAWN FILMS

a. Heat Transfer Analysis

The temperature distribution within a polymer film during drawing is considerably more complicated than the idealized one-dimensional model presented in Chapter IV; this presents significant problems in performing a thermal--structure development analysis. During drawing a number of complications arise including the problem of specifying boundary conditons, anisotropic thermal properties and predicting heat generation rates due to crystallization and deformation. Experimentally measured temperatures along with the values predicted by heat transfer theory for films GA and GB are shown in Figures V-7 and V-8, respectively.

The profiles represent cross sections of a cast sheet sample or slab. Initially the sample is at a uniform temperature of 25^{o}C, suddenly the temperatures at the opposite surfaces were changed and the sample allowed to

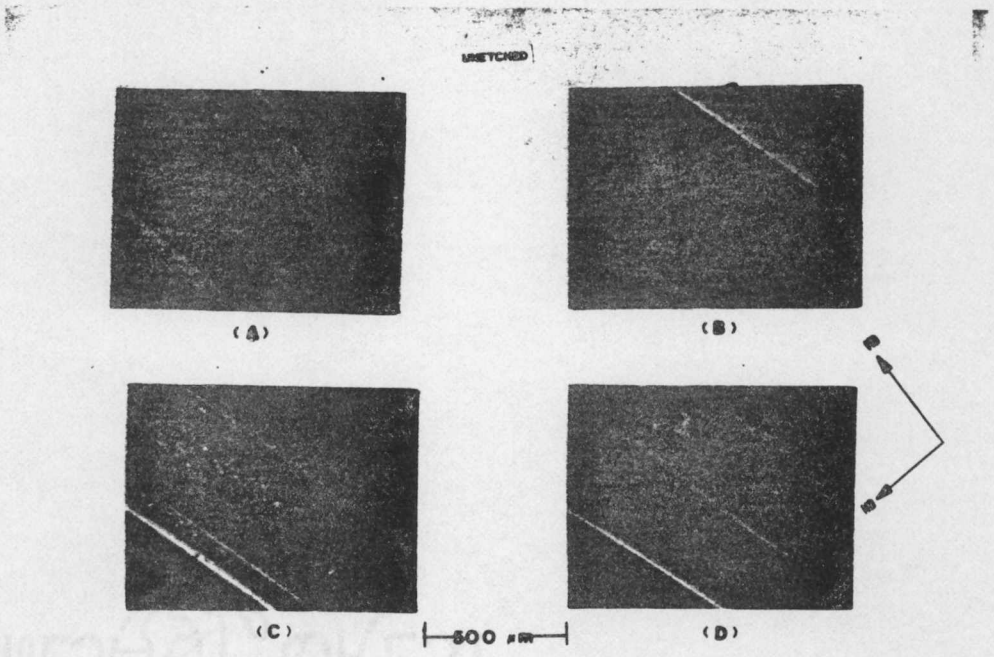


Figure V-6. SEM photomicrographs of TD cross sections of uniaxial stretched films: (a) NGB1 (80°C); (b) NGB3 (100°C); (c) GA3 (70--120°C) and (d) GB3 (50--150°C). All films drawn at 10.0 min^{-1}.

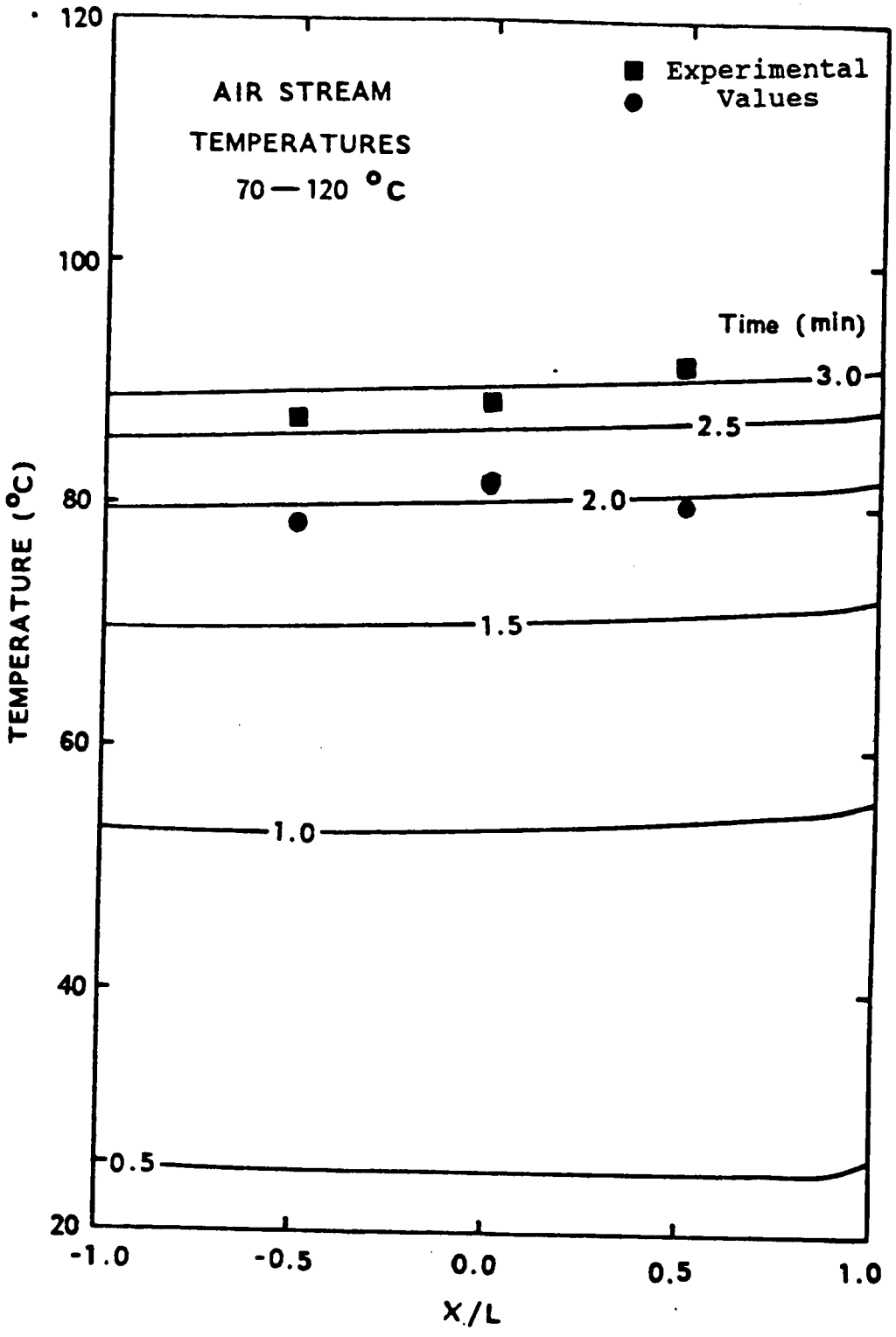


Figure V-7. Temperature profiles for cast sheet sample C5 prior to stretching: Air stream temperatures: T_C = 70°C and T_H = 120°C.

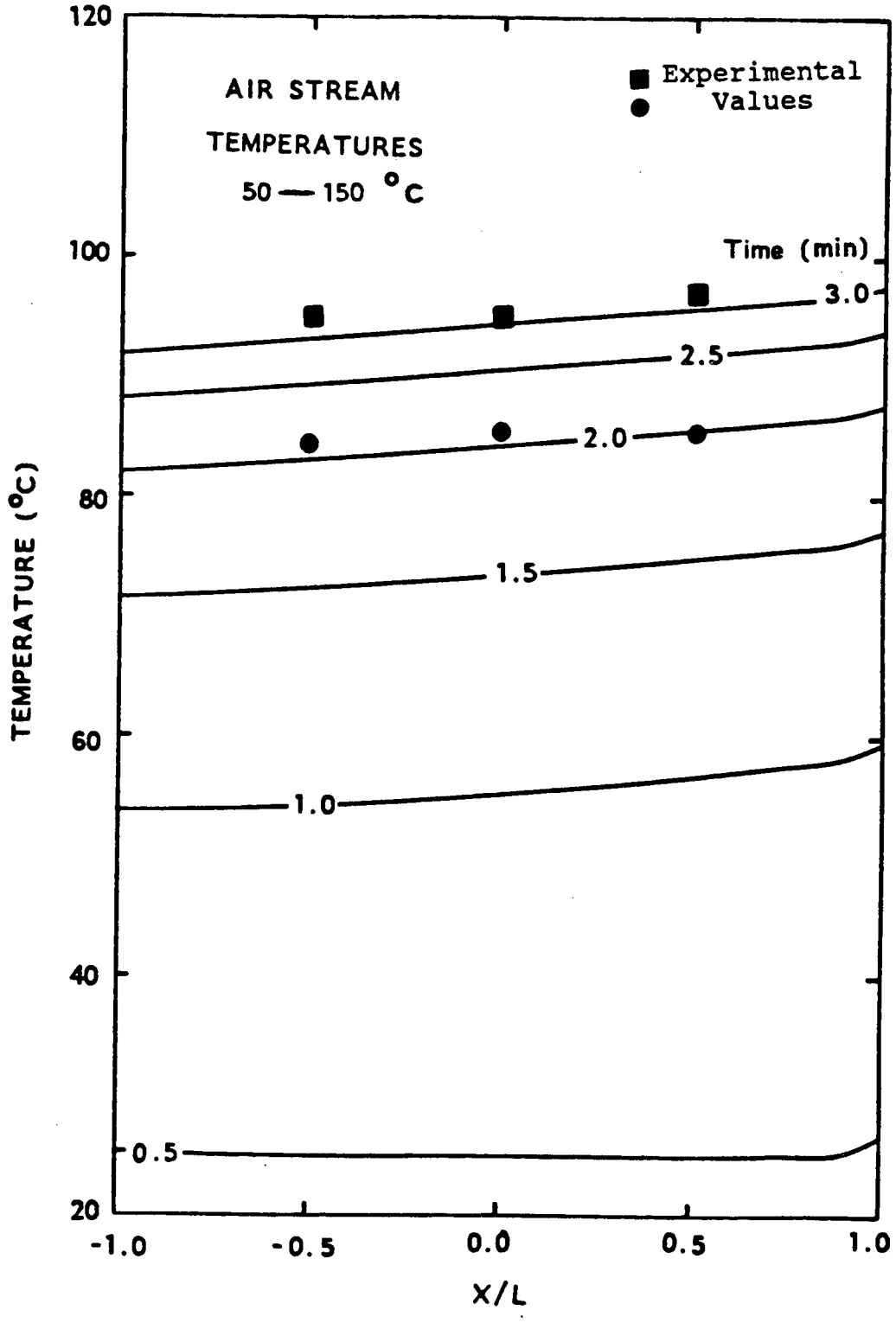


Figure V-8. Temperature profiles for cast sheet sample C5 prior to stretching: Air stream temperatures: T_C = 50°C and T_H = 150°C.

reach a steady state. Experimentally, this was achieved by isolating the two heating plates of the T.M. Long Film Stretcher using a suitable piece of insulation. The insulation was removed and the sample inserted into the grips as quickly as possible.

The most significant problem in the heat transfer analysis is the choice of the heat transfer coefficient. Predicted profiles plotted as a function of residence time for several heat transfer coefficients were used to determine the best fit to the experimentally measured temperatures. All profiles are relatively flat, an indication of the strong influence of the heat transfer coefficient.

b. Surface-to-Surface Variations in Refractive Index and Birefringence Obtained Using an Abbe' Refractometer

Refractive indices measured on opposite sides of cast sheet samples are listed in Table V-3. There is no indication of a strong through the thickness variation in refractive index for any sample. Corresponding birfringence values are shown in Table V-4. The samples did not reveal any large difference in birefringence from side-to-side even in the case of the thick cast sheet samples. Differential birefringence values for cast sheet samples and selected gradient drawn films are listed in Table V-5.

TABLE V-3

SURFACE-TO-SURFACE VARIATIONS IN REFRACTIVE INDEX OF CAST SHEET SAMPLES

Sample	Side	n_1	n_3	n_2	n_3'	n_{iso}
C1	1	1.5777	1.5760	1.5776	1.5757	1.5768
	2	1.5786	1.5771	1.5780	1.5770	1.5777
C2	1	1.5781	1.5765	1.5765	1.5766	1.5769
	2	1.5780	1.5745	1.5760	1.5745	1.5774
C3	1	1.5780	1.5745	1.5760	1.5745	1.5760
	2	1.5780	1.5750	1.5765	1.5755	1.5763
C4	1	1.5769	1.5740	1.5755	1.5740	1.5751
	2	1.5770	1.5752	1.5760	1.5751	1.5758
C5	1	1.5790	1.5688	1.5706	1.5688	1.5723
	2	1.5810	1.5710	1.5735	1.5711	1.5737

TABLE V-4

SURFACE-TO-SURFACE VARIATIONS IN BIREFRINGENCE OF CAST SHEET SAMPLES

Sample	Side	Birefringence		
		$\Delta n_{12} \times 10^3$	$\Delta n_{13} \times 10^3$	$\Delta n_{13} \times 10^3$
C1	1	0.1	1.9	1.8
	2	1.2	1.5	0.3
C2	1	1.5	1.6	0.1
	2	2.0	3.5	1.5
C3	1	2.0	3.5	1.5
	2	2.7	3.7	1.0
C4	1	1.4	2.9	1.5
	2	1.0	1.8	0.8
C5	1	8.4	10.2	1.8
	2	7.5	9.9	2.4

TABLE V-5

DIFFERENTIAL BIREFRINGENCES OF CAST SHEET AND SELECTED NONGRADIENT AND GRADIENT UNIAXIAL FILMS

Sample	$\delta n_{12} \times 10^3$	$\delta n_{13} \times 10^3$	$\delta n_{23} \times 10^3$
C1	1.1	0.4	1.5
C2	0.5	2.1	1.4
C3	0.7	0.2	1.5
C4	0.4	1.1	0.7
C5	0.9	0.3	0.6
NGB1	1.2	2.7	1.4
NGB2	0.4	1.4	0.9
NGB3	0.6	0.8	0.5
NGB4	0.2	0.5	0.1
GA3	3.5	8.5	12.0
GB3	27.8	26.4	1.5

All stretched films drawn at 10.0 min^{-1}.

c. Refractive Index and Birefringence Obtained from Interference Microscopy

As already discussed, interference microscopy is the most sensitive technique for studying local variations in refractive index in inhomogeneous materials. Thus it was chosen as the technique for chracterizing through the thickness inhomogeneity in gradient films. Another area where through thickness variations might be expected is in the production of hollow articles produced by the stretch blow molding process. Since PET is used in the production of stretch blow molded beverage bottles and the results of a previous study (14) using the Abbe' refractometer indicated surface-to-surface differences in refractive indices, this study was expanded to include a bottle sample. Samples for interference microscopy included a uniaxially drawn PET film and a stretch blow molded PET bottle. A complete description of the samples is listed in Table V-6.

The objective of the interference microscopy experiments was primarily to demonstrate the applicability and the versatility of using interference microscopy as a technique for characterizing gradients through the thickness and secondly to determine the magnitude of such gradients. Sections from film and bottle samples were prepared as described in Chapter III (see page 115). Sections cut parallel and perpendicular to the stretch direction of the film sample were designated as "machine direction" (MD) and

TABLE V-6

SAMPLES FOR INTERFERENCE MICROSCOPY

Sample	Identification	Source	[η] (g/dl)
Film	Hot Press Uniaxial, 90°C 10.0 min^{-1}	UT[a] (AMERICAN ENKA)[b]	0.65
Bottle	Stretch Blow Molded (12 cm) 90°C, 60 psig	UT[a] (AMERICAN ENKA)[b]	0.92

a - Fabricated at the University of Tennessee.

b - Source of polymer.

"transverse direction" (TD) sections, respectively. In the case of the bottle sample, sections cut parallel to the circumferential direction were designated as "hoop direction" (HD) sections.

A Leitz Double-Beam Interference Microscope was used to measure refractive index as a function of through the thickness position. The film or bottle sample was positioned in the image field such that the fringes were perpendicular to the long axis of the specimen. Refractive indices calculated from fringe displacements using Equation II-9 are plotted as a function of through the thickness position of the stretched film sample as shown in Figure V-9. Similarly, refractive index profiles for the bottle sample are presented in Figure V-10. Corresponding birefringence profiles for the film and bottle samples are shown in Figures V-11 and V-12 respectively. As can be seen in the figures, the profiles appear to be relatively flat with the noticable absence of any steep gradients. The bottle sample does not show any indication of a steep through the thickness gradient, this finding is in direct contradiction to the results obtained using the Abbe' refractometer. One possible explanation for the discrepancy in results is the curvature of the bottle sample used in making measurements with the Abbe' refractometer.

A comparison of birefringence values obtained from the Abbe' refractometer and interference microscopy measurements

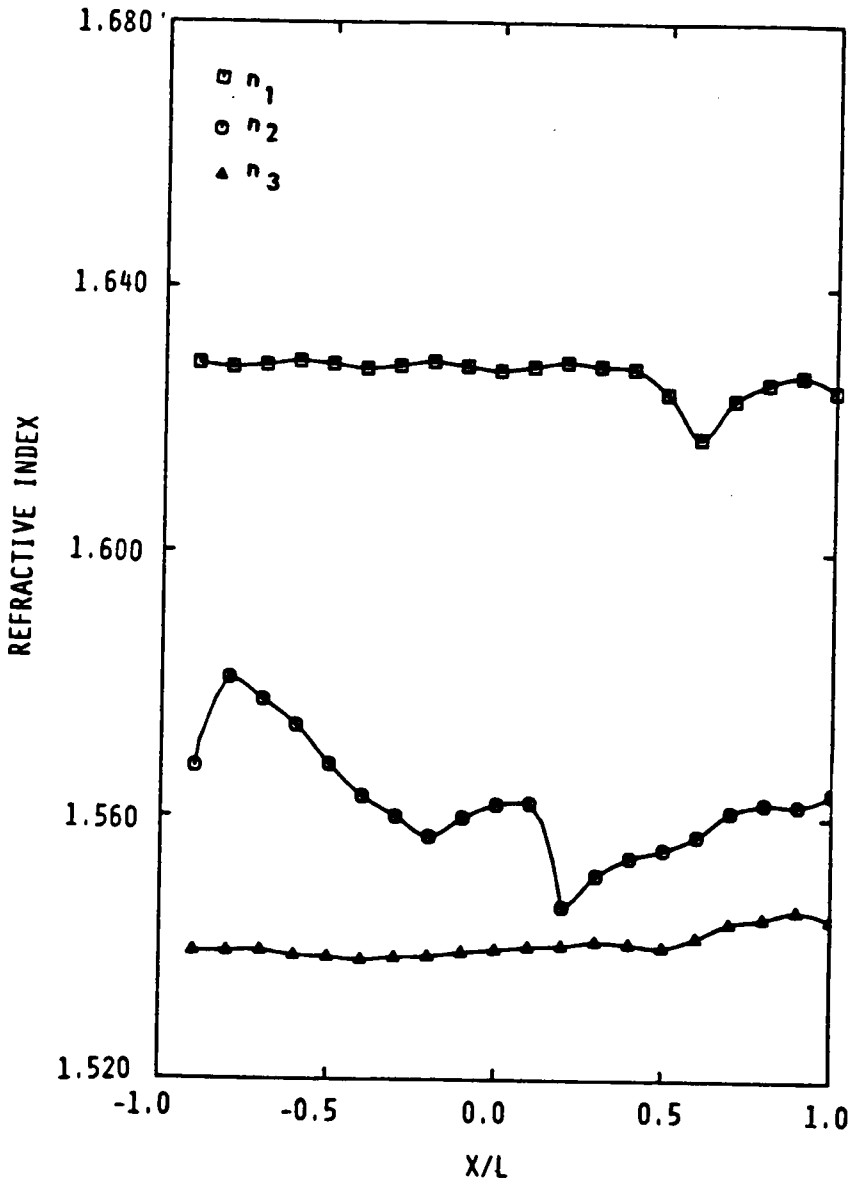


Figure V-9. Refractive index profiles through the thickness of the film sample obtained from interference microscopy.

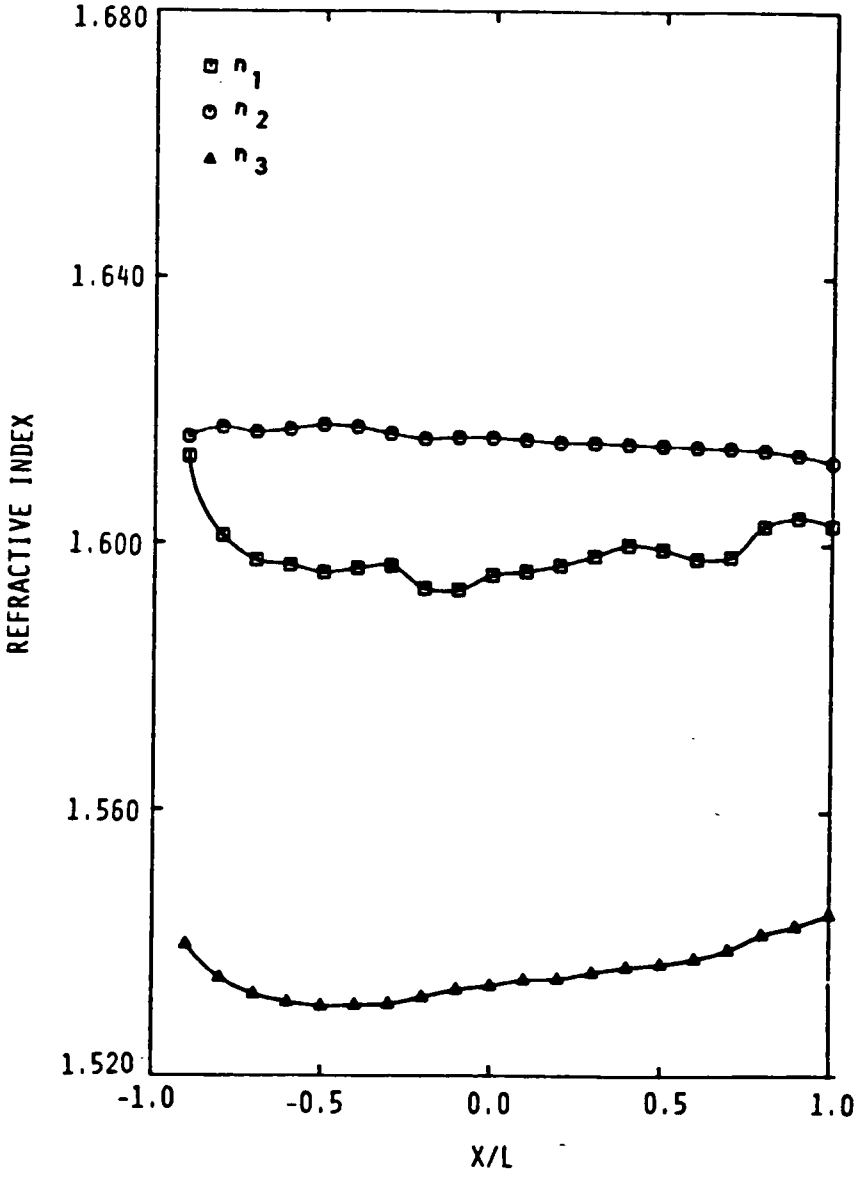


Figure V-10. Refractive index profiles through the thickness of the bottle sample obtained from interference microscopy.

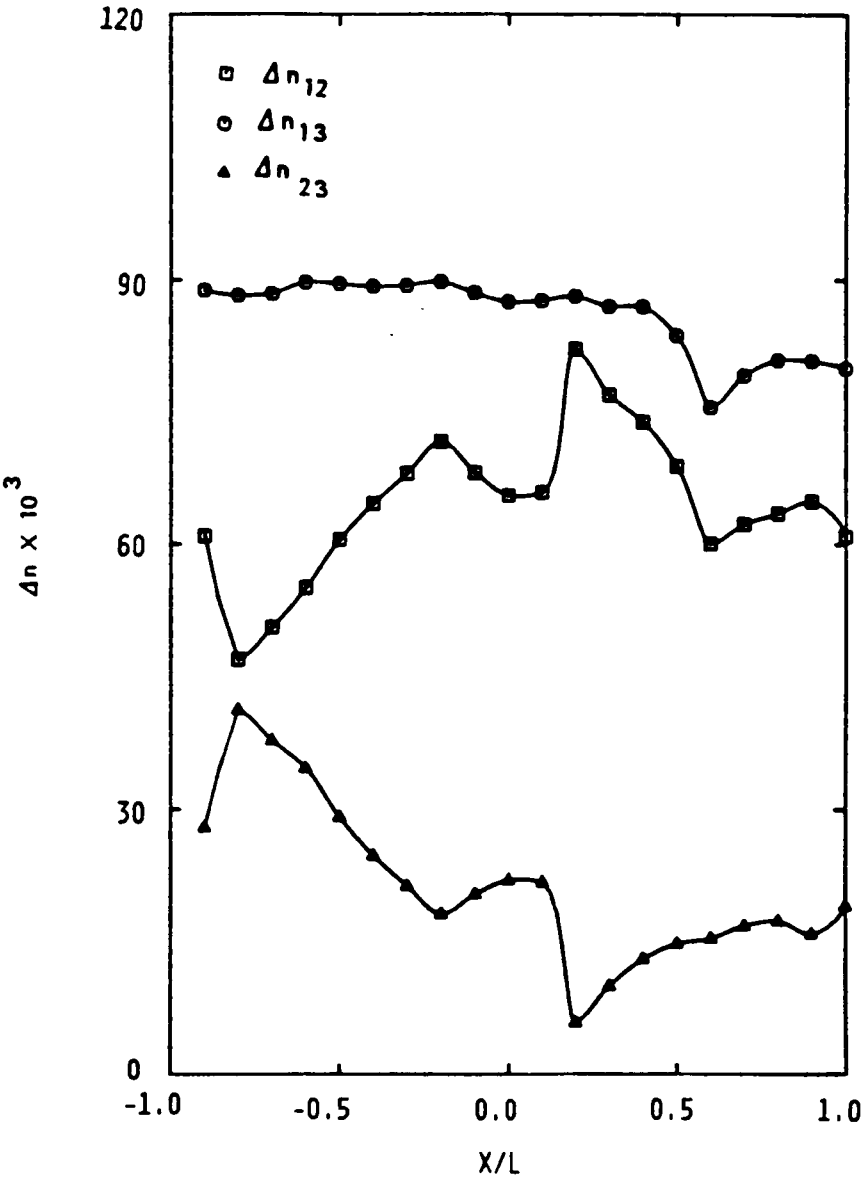


Figure V-11. Birefringence profiles through the thickness of the film sample obtained from interference microscopy.

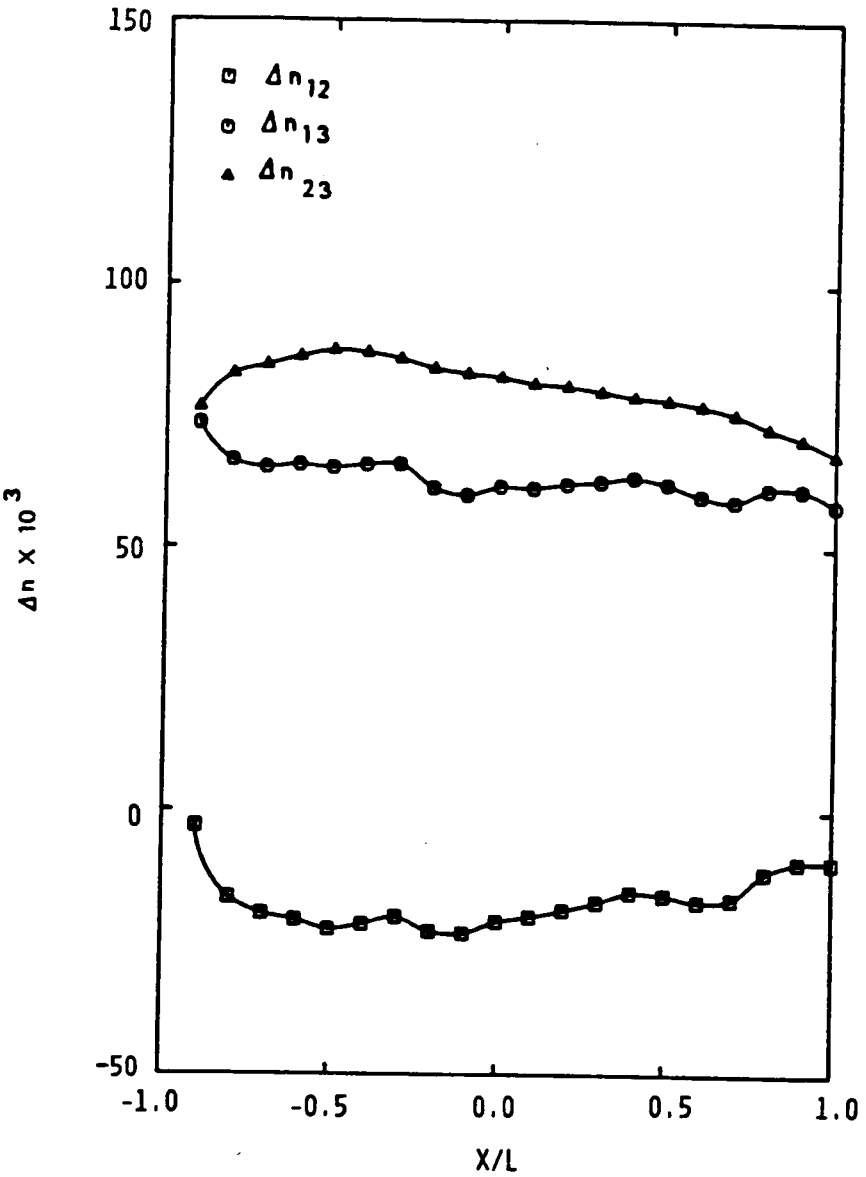


Figure V-12. Birefringence profiles through the thickness of the bottle sample obtained from interference microscopy.

is given in Table V-7. The inability to correctly match fringes is the most likely explanation for the lower average birefringence calculated from refractive indices obtained from interferene measurements. The low refractive index values arise from the experimental difficulty of fringe matching encountered when observing a large object such as a film section. When monochromatic light is used, all of the fringes appear to be identical and hence it is not possible to determine which fringe in the specimen corresponds to a given fringe in the background. Thus the actual fringe displacement, that is the distance between corresponding fringes may be D, D+d, D+2d, etc.. This ambiguity can be resolved by using white light instead of a monochromatic source and measuring the fringe separation between the white fringe having zero path difference in the specimen section and the corresponding fringe in the background. However, dispersion effects often preclude using this method. An alternate method is to use wedge shaped sections. The fringes can be matched by determinig the fringe shift at the point where the thickness of the specimen approaches zero. However, this error only reduces the absolute values of the actual refractive indices but does not alter the profile.

TABLE V-7

COMPARISON OF BIREFRINGENCE RESULTS

Sample	$\Delta n \times 10^3$	Abbe' Refractometer	Interference Microscope
Film	12	90.1	64.7
	13	95.1	85.9
	23	5.0	21.2
Bottle (Outside)	13	74.8	61.3
	23	89.7	73.4
Bottle (Inside)	13	113.6	70.7
	23	154.0	83.1

C. LAMINATE FILMS

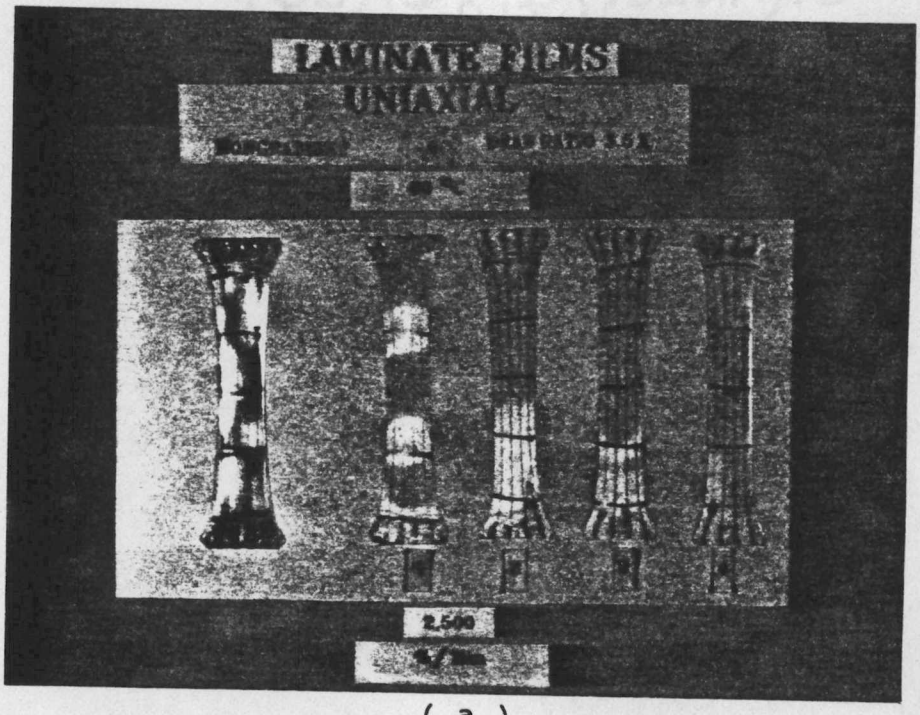
a. General Characteristics

Drawn laminate films were utilized in an attempt to characterize through the thickness variations in orientation and structure. Laminates were also used as an approximate means of modelling inhomogeneity and imposing a larger through the thickness temperature gradient.

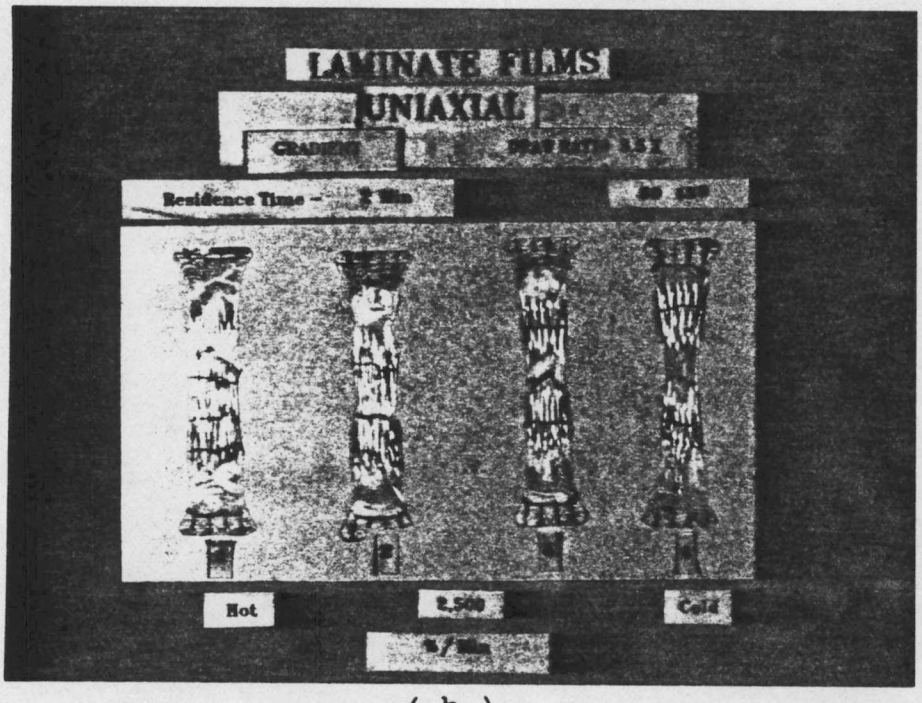
The deformation behavior of uniaxial and UCW laminate drawn films can be seen in Figures V-13 and V-14 respectively. Clearly, the drawing behavior of the nongradient films appears to be homogeneous whereas gradient samples exhibited nonhomogeneous characteristics. A direct comparison between a nongradient and gradient laminate uniaxial sample is shown in Figure V-15. Notice the variation in draw ratios between the individual layers and the general degree of inhomogeneity.

b. Birefringence

Birefringences and densities for the individual layers of UCW laminate drawn film GL2 are listed in Table V-8. The results shown in Table V-8 confirm that the layers act as independent films, this is reflected in the differences in birefringence and crystallinity of the individual layers. Layers one, two and three have essentially the same levels of orientation and crystallinity whereas layer four has a lower degree of orientaion. The lower birefringence value

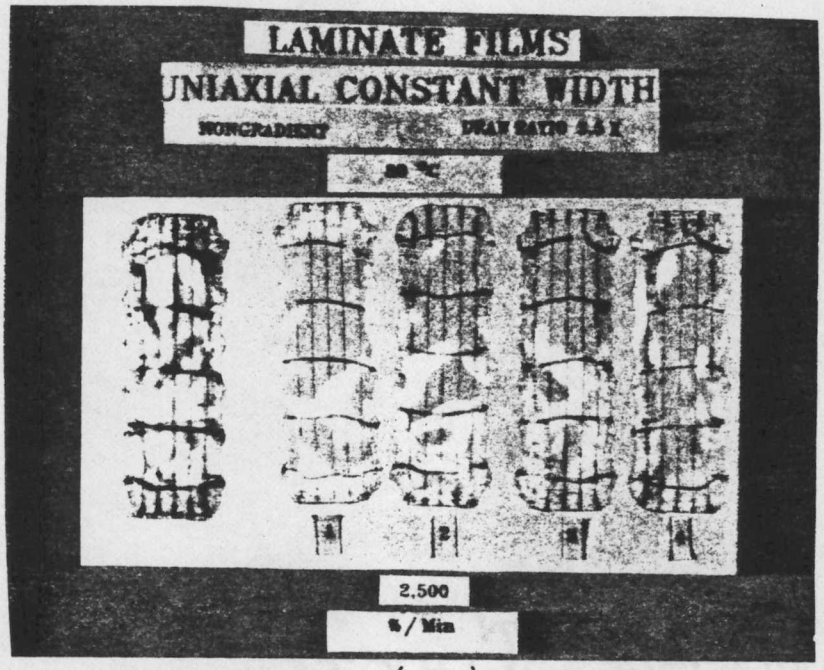


(a)

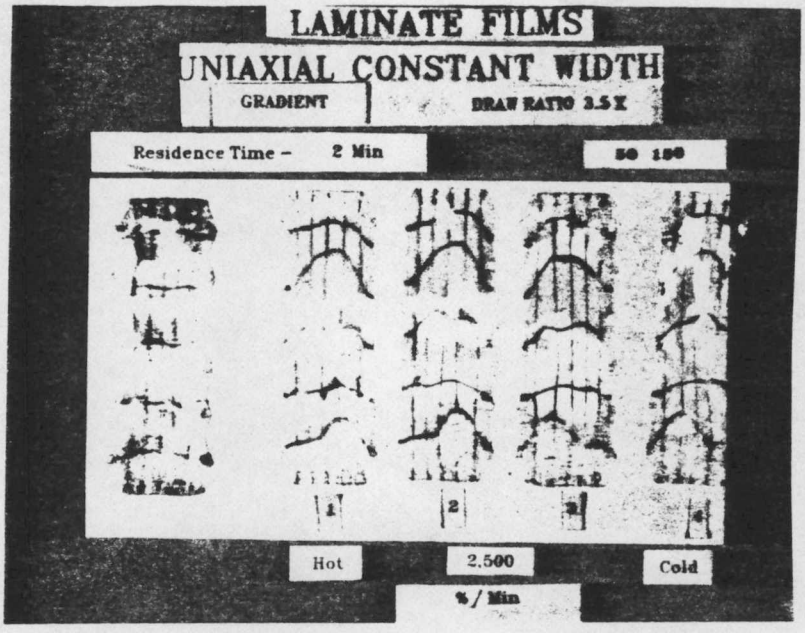


(b)

Figure V-13. Photographs of uniaxial laminate films drawn at 10.0 min^{-1}: (a) NGL1 and (b) GL2.



(a)



(b)

Figure V-14. Photographs of UCW laminate films drawn at 10.0 min^{-1}: (a) NGL1 and (b) GL2.

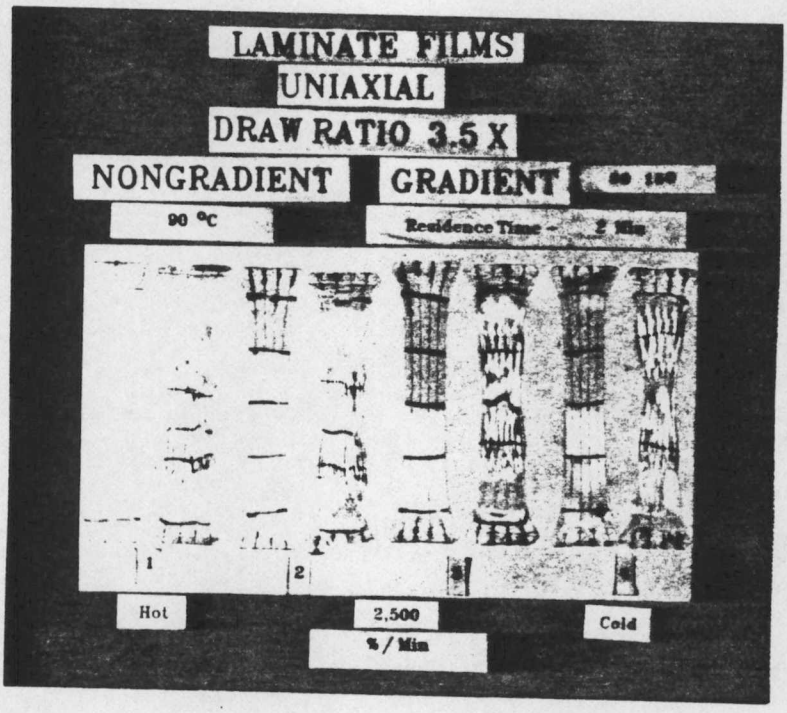


Figure V-15. Photograph showing the comparison between nongradient (NGL2) and gradient (GL2) uniaxial laminate films. Both films drawn at 10.0 min^{-1}.

TABLE V-8

DENSITY AND BIREFRINGENCES OF THE INDIVIDUAL LAYERS OF UCW LAMINATE FILM GL2

Layer	Density (g/cm^3)	X_c (%)	Birefringence $\Delta n_{12} \times 10^3$	$\Delta n_{13} \times 10^3$	$\Delta n_{23} \times 10^3$
1	1.3500	13.9	84.7	128.7	4.4
2	1.3640	25.4	89.1	131.0	4.2
3	1.3650	26.2	96.1	131.0	3.5
4	1.3650	26.2	78.7	110.0	3.2

for layer four which was in direct contact with the 150°C air stream is a reflection of the higher temperature and slower quench rate for that particular layer. The results should be interpreted with some degree of caution because of the absence of cohesive bonding between the individual layers. However, the differences in birefringence and density due indicate the possibility of significant through the thickness gradients existing provided the applied temperature gradient is large.

c. DSC Results

DSC Thermograms of the individual layers of uniaxial and UCW laminate film samples GL2 drawn at 10.0 min^{-1} are shown in Figures V-12 and V-13, respectively. The thermograms corresponding to one-piece uniaxial and UCW film GB3 drawn at the same conditions are included in the figures. The most significant feature of the curves is the appearance of two peaks in the vicinity of the glass transition in some of the samples.

The glass transition is defined as the temperature at which the onset of motion of the main chain segments in the amorphous regions is observed. This point is accompanied by marked changes in properties most notably modulus. T_g can be determined to be either the extrapolated onset temperature or the inflection point on the glass transition peak. For the purpose of this research T_g was obtained from the inflection point of expanded thermograms of the glass

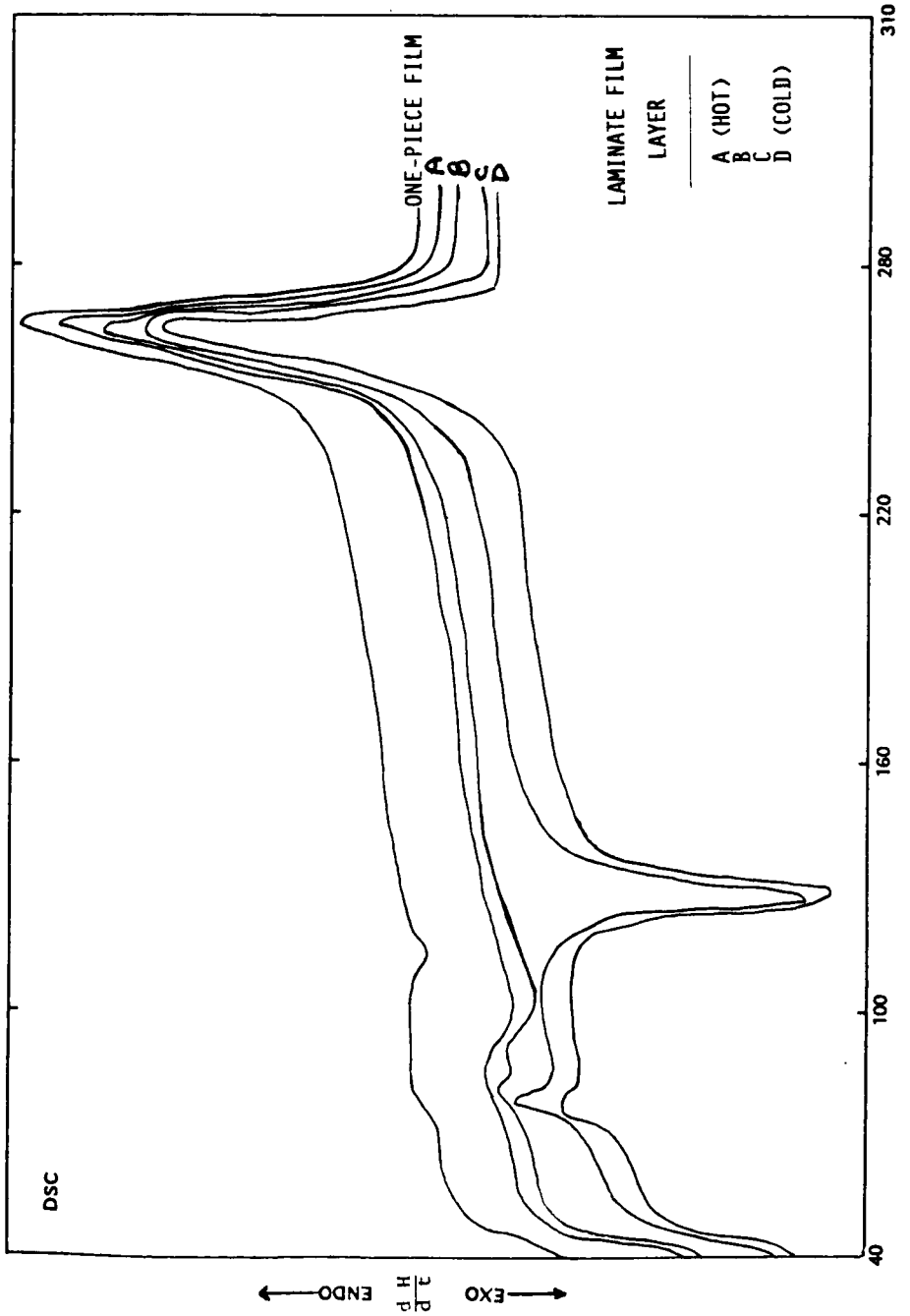


Figure V-16. DSC thermograms of gradient uniaxial laminate film GL2 drawn at 10.0 min^{-1}.

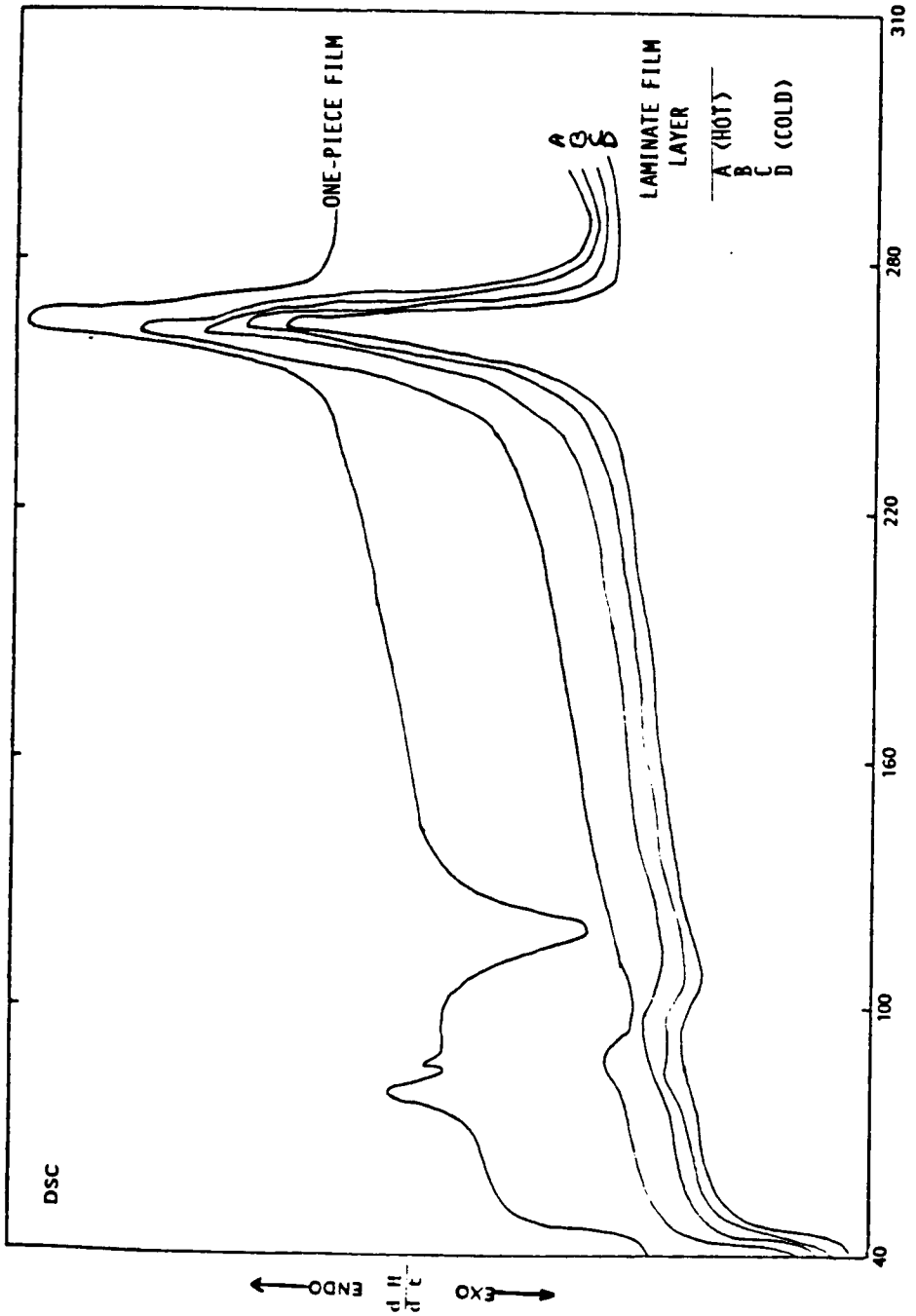


Figure V-17. DSC thermograms of gradient UCW laminate film GL2 drawn at 10.0 min^{-1}.

transition region. Expanded thermograms for selected films are shown in Figures V-18 and V-19.

The appearance of two peaks is more likely the results of a splitting of the single peak into two as opposed to being two true glass transitions as observed in multicomponent systems. This behavior may be the result of different degrees of order existing within the amorphous regions through the thickness, a reflection of the temperature gradient within the film prior to stretching.

A complete description of the thermal characteristics of UCW laminate film GL2 are given in Table V-9. The influence of crystallinity on T_g has been shown to be complex. Some investigators report an increase in Tg with increasing levels of crystallinity, a consequence of the crystallites restricting chain mobility. However, the variability and low level of reproducibility of the thermograms did not permit any correlation between the temperature gradient and the thermal properties to be made.

d. Small-Angle Light Scattering

In the present investigation the technique was used to determine the possible variation in through the thickness superstructure by observing SALS patterns from individual layers of laminate samples.

H_V and V_V patterns from the individual layers of uniaxial laminate film GL2 drawn at 10.0 min^{-1} are shown in Figure V-20. The magnitude of the gradient as predicted by

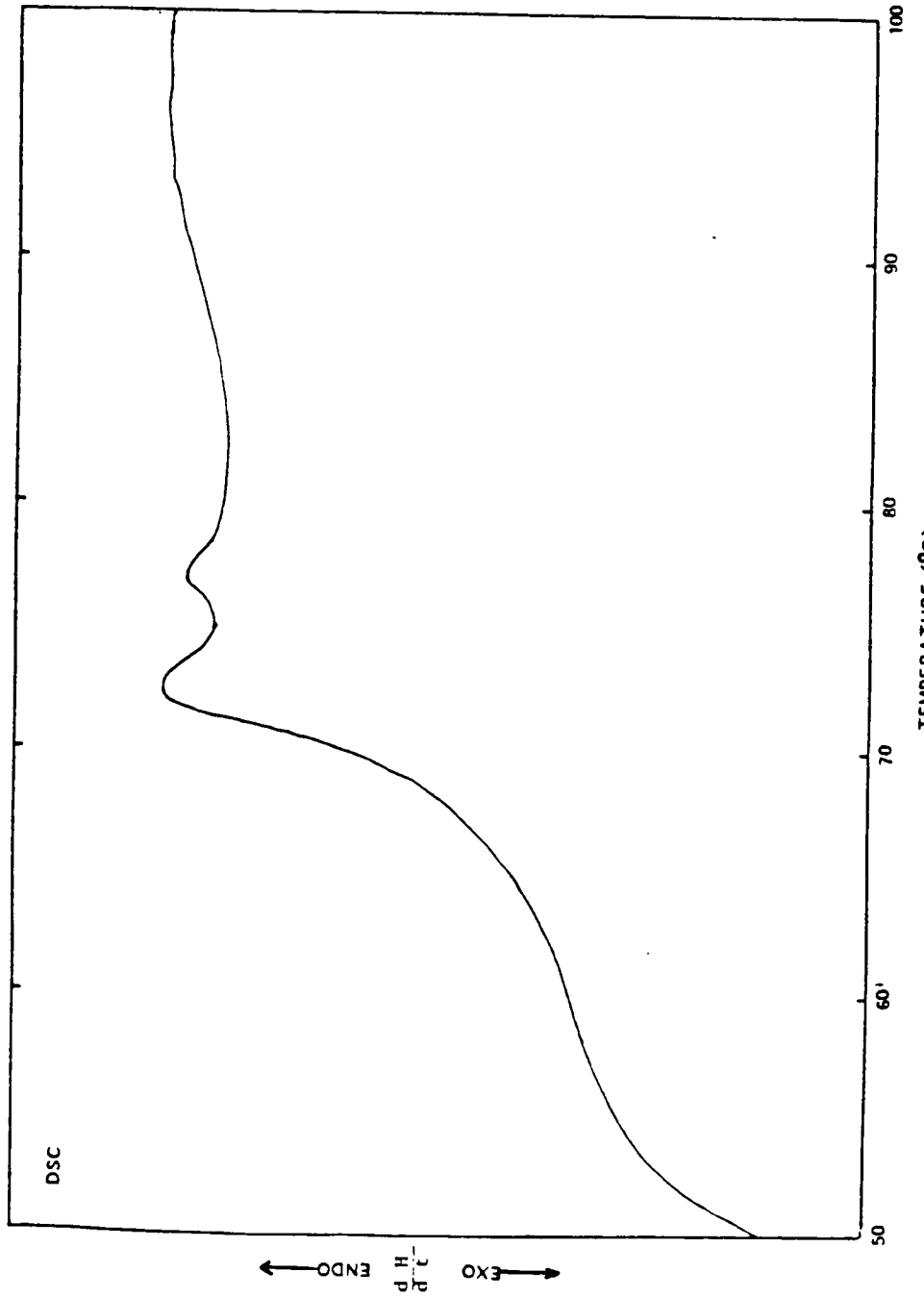


Figure V-18. DSC thermogram of the glass transition region of gradient uniaxial film GB3.

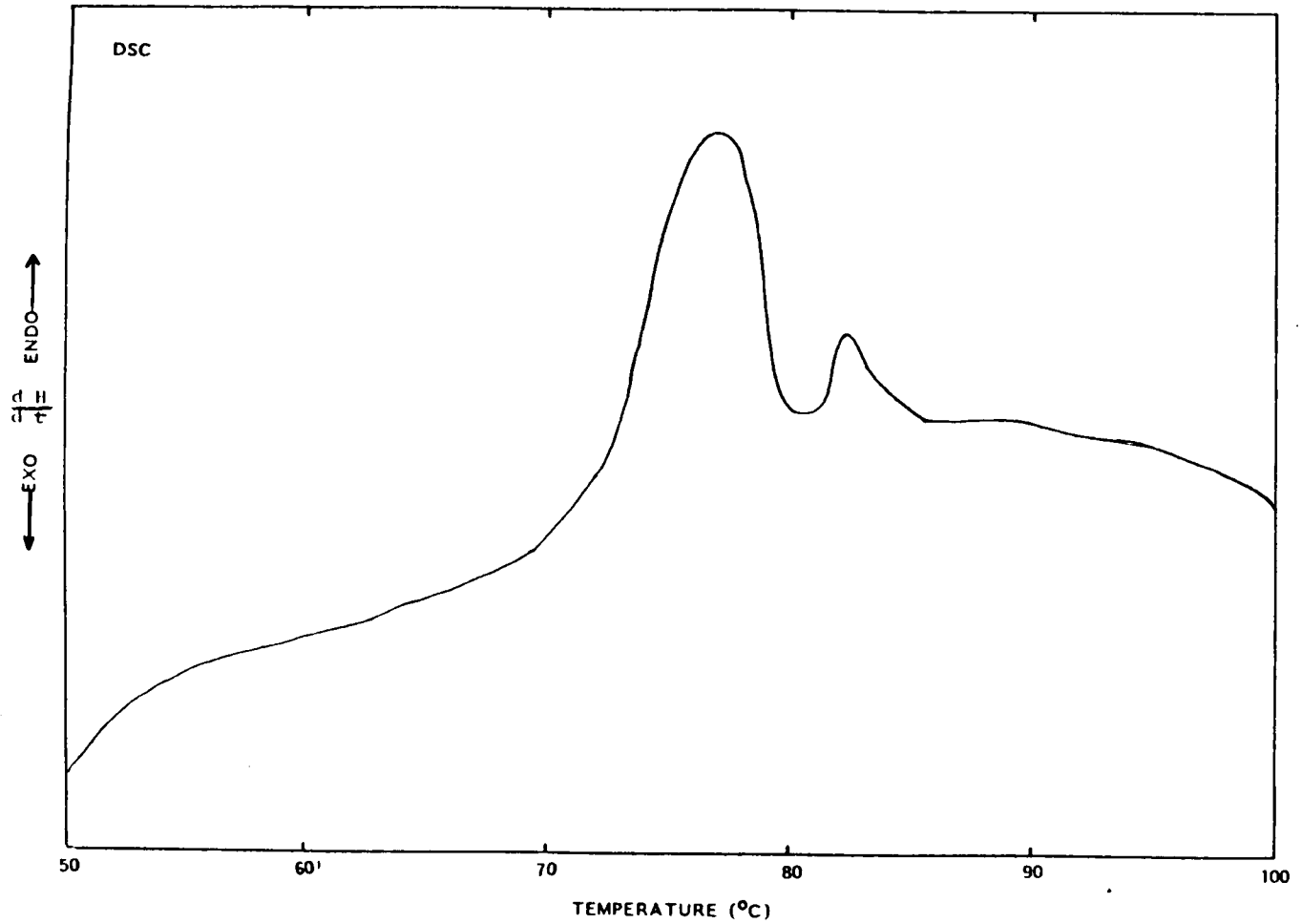


Figure V-19. DSC thermogram of the glass transition region of gradient UCW film GL2 (Layer 1).

Table V-9

THERMAL CHARACTERISTICS OF GRADIENT ONE-PIECE AND LAMINTE FILMS

Sample	Density (g/cm^3)	T_g (^oC)	T_c (^oC)	T_m (^oC)	X_c(DSC) (%)
U/GB3	1.3450	74	108	249	12
U/GL2 (1)	1.3325	69 (74)*	123	248	9
(2)	1.3400	71	115	248	11
(3)	1.3545	75 (81)*	98	249	11
(4)	1.3560	74	97	250	16
UCW/GB3	1.3340	73 (81)*	115	249	11
UCW/GL2 (1)	1.3500	77	104	250	10
(2)	1.3640	77	107	251	10
(3)	1.3650	75 (82)*	107	250	14
(4)	1.3650	74	100	249	13

* Two glass transition temperatures observed.

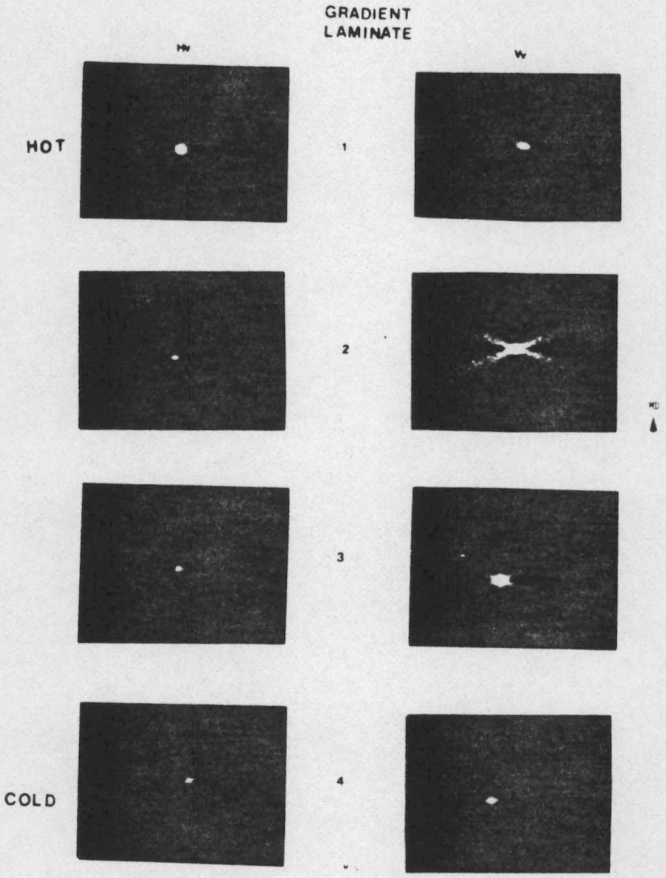


Figure V-20. SALS Hv and V_V patterns from the individual layers of uniaxial laminate film GL2 drawn at 10.0 min^{-1}.

heat transfer model is about 6.0°C. All patterns indicate a spherulitic or deformed spherulitic morphology, this finding suggests crystallization occurred in the cast sheet prior to stretching.

The scattering of light from heterogenous films, that is gradient and laminate films can be interpreted to a first approximation in terms of the theory of multiple scattering. As discussed by Prudhomme et al. (103), the effect of multiple scattering is to make the patterns more diffuse by increasing the intensity in the low intensity regions and decreasing the intensity in the high intensity regions. Prudhomme et al. used a multiple layer model to describe multiple scattering from thin low density polyethylene films.

The model can be described as follows: Consider a film sample of thickness L to be composed of i individual layers having thickness l as shown in Figure V-21. At point x_o a beam of light will have intensity I_o. As the beam traverses the first layer, a portion of its energy is lost due to scattering. This portion of lost energy constitutes the primary scattering beam. The incident beam and primary beam continue to pass through the second layer of the film where again a portion of the intensity is lost, this process is repeated for each theoretical layer.

Both H_v and V_v patterns from a gradient one-piece film GB3 and laminate film sample GL2 drawn 10.0 min^{-1} are

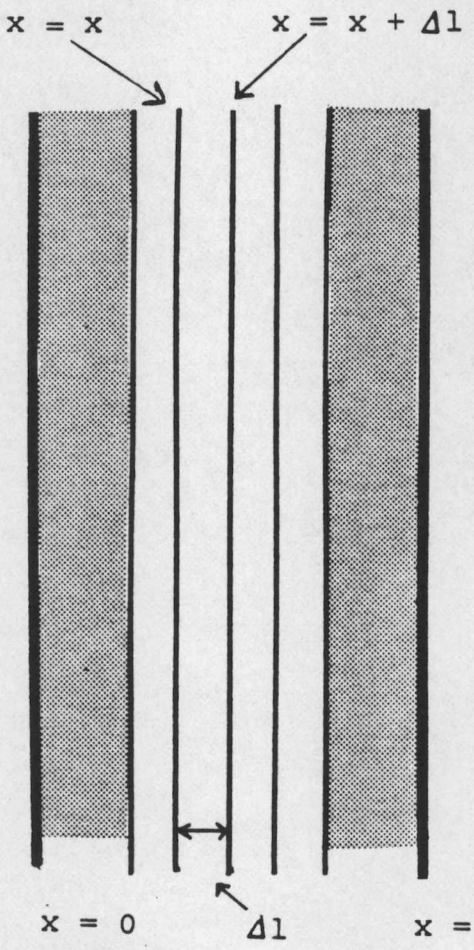


Figure V-21. Schematic of the layered structure of a thin polymer film.

Source: Prud'homme, R.E., L. Bourland, R.T. Natarajan and R.S. Stein, J. Polym. Sci., Polym. Phys Ed., 12, 1955 (1974).

presented in Figure V-22. Note the similarity in the shape of the patterns and in the more diffuse character of the patterns from the laminate film. Both patterns were taken at the same exposure time of 30 seconds for the H_v pattern and 1/10 second for the V_v pattern.

e. Chemical Etching

The chemical etching of PET film by aliphatic amines is based on the attack of the ester group by the amine. Aminolysis of PET by n-propylamine results in the formation of two degradation products, N, N' n-propyl terephthalamide and ethylene glycol. Infrared spectroscopy of the reaction products by Baker (5) showed the reaction to be free of any side reactions.

Several studies (25,88) have demonstrated that both the crystalline and noncrystalline regions of the film were attacked, however the rate of attack was different for each region. All prior studies on PET films degraded by the aminolysis technique have been limited to the study of the development of surface macrostructure in homogeneously deformed films. In this investigation the technique was applied to the study of through the thickness inhomogeneity. If different levels of crystallinity and degrees of orientation are present some knowledge might be gained by studying differences in surface macrostructure.

Optical Microscopy. The dependence of the size of the surface morphology on the degree of orientation in uniaxial

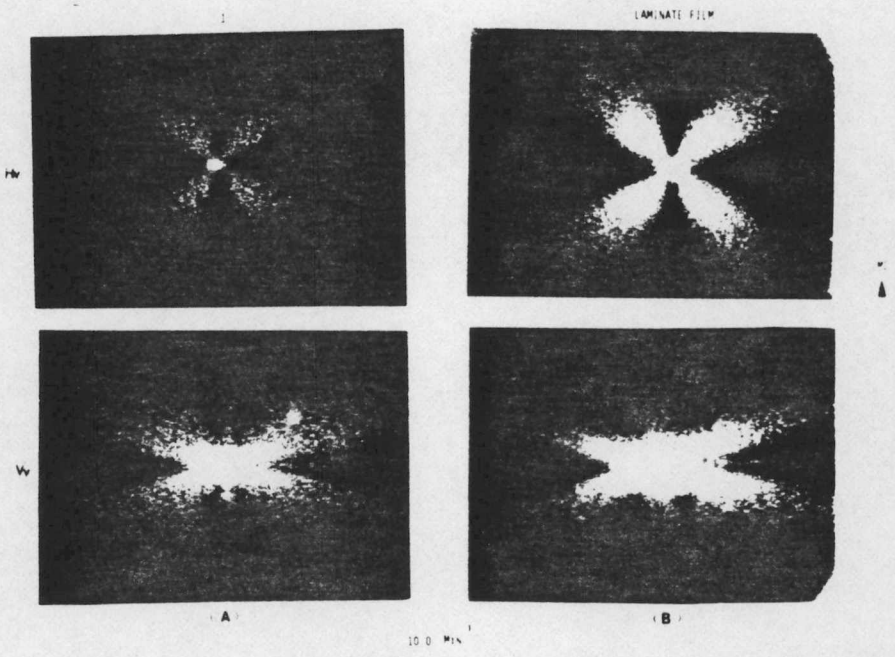


Figure V-22. SALS H_V and V_V patterns from uniaxial gradient films drawn at 10.0 min^{-1}: GB3 (one-piece) and (b) GL2 (4--layer laminate).

flim NGB is shown in Figure V-23. In general, films of higher orientation possess smaller surface features. As can be seen in Figure V-23, the number of etch lines per unit width is considerably greater for the film drawn at 90°C than for the film stretched at 110°C. Optical photomicrographs of opposite surfaces of uniaxial gradient films GA and GB are presented in Figure V-24. The surface etch patterns are significantly different, especially for film GB which was exposed to the 50°C and 150°C air stream temperatures. The pattern from the surface exposed to the 150°C closely resembles that of the cast sheet sample whereas the surface exposed to the 50°C appears more like that of oriented films drawn at 80°C or 90°C.

Although the use of etchants is somewhat questionable when applied to the study of morphology, it is likely that the differences observed of surface macrostructures in gradient films does provide at least qualitative evidence for surface-to-surface variations in orientation and crystallinity.

Scanning Electron Microscopy. In order to determine whether differences in etch rates existed for uniaxial gradient films, SEM photomicrographs of fracture surfaces of etched films were examined. Photomicrographs of TD fracture surfaces are shown in Figure V-25. Etched films did not show any penetration boundaries. For the case of gradient samples, the surfaces exposed to the higher air stream

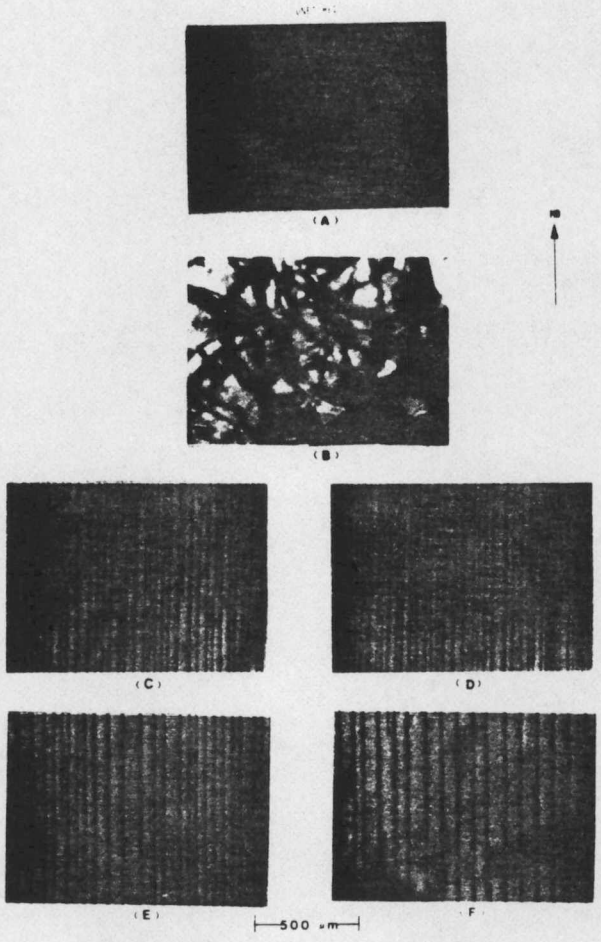


Figure V-23. Optical photomicrographs of n-propylamine etched uniaxial films drawn at 10.0 min^{-1}: (a) Unetched NGB1 (80°C); (b) Cast Sheet C5; (c) NGB1 (80°C); (d) NGB2 (90°C); (e) NGB3 (100°C) and (f) NGB4 (110°C).

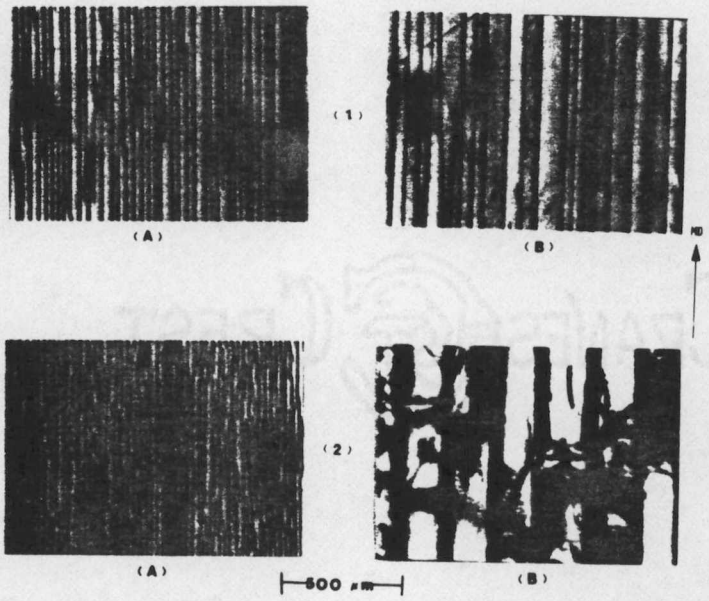


Figure V-24. Optical photomicrographs of n-propylamine etched uniaxial films drawn at 10.0 min^{-1}: (1) GA3: (a) Cold (70°C), (b) Hot (120°C) and (2) GB3: (a) Cold (50°C), (b) Hot (150°C).

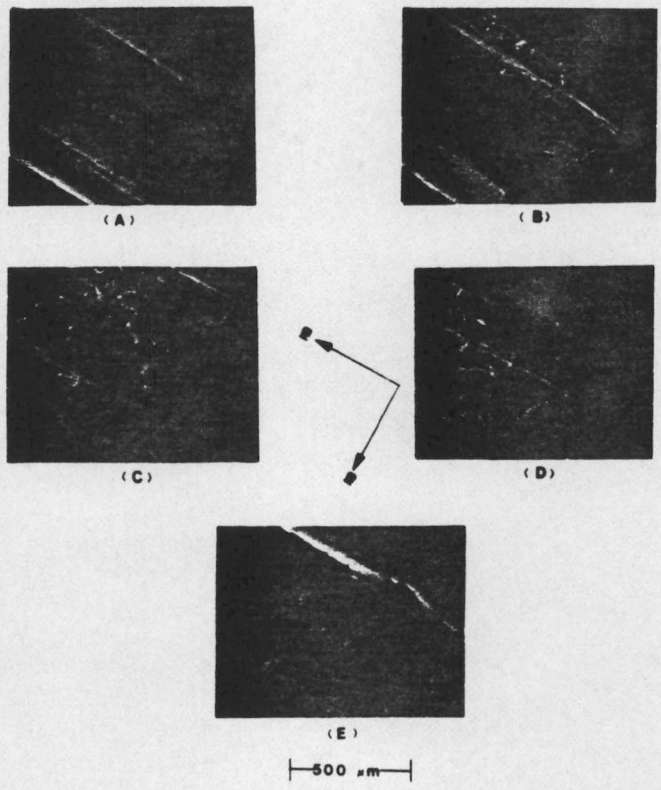


Figure V-25. SEM photomicrographs of TD_1 fracture surfaces of uniaxial films drawn at 10.0 min^{-1}: (a) NGB1 (80°C); (b) NGB3 (100°C); (c) GA3 (70--120°C); (d) GB3 (50--150°C) and (e) Cast Sheet C5.

temperatures appear to have been degraded to a greater extent than the cold surfaces. Observe the surface (upper) macrostructure of gradient film GB3 (see Figure V-25d) exposed to the 150^{o}C air stream temperature, a portion of the surface appears to have "flaked off". This finding is in agreement with the low birefringence values, indicative of an unoriented surface layer. In general, SEM photomicrographs of chemically etched films are similar in appearance to those of unetched samples.

CHAPTER VI

CONCLUSIONS

From the results obtained in the present invesitgation several conclusions can be drawn, they include:

1. Through the thickness variations that exist in PET films drawn in the presence of superimposed thermal gradients using convective heat transfer techniques were observed to be small.

2. An Abbe' refractometer can be used to detect through the thickness differences in orientation (birefringence) in oriented films provided the film surfaces are smooth and specimens used in making the measurements are flat.

3. Interference microscopy is the most useful technique currently available for measuring refractive index profiles through the thickness of thin polymer films. A limitation of the technique is the need to prepare sections from films prior to making measurements.

CHAPTER VII

RECOMMENDATIONS

1. A more thorough study of the use of interference microscopy as a means of investigating through the thickness inhomogeneity in thin polymer films and bottles is needed. Any future study should concentrate on unoriented fibers and films quenched under identical conditions to determine the effect of sectioning on the measured profile.

2. PET was the only polymer investigated in this study. Perhaps a better polymer to study would be PETG, a glycol modified copolyester which has sluggish crystallization kinetics. This would provide a means of minimizing the effects due to crystallization.

3. The area of blow molding appears to be a more likely source of producing large through the thickness variations in orientation and structure in PET. Preliminary results do show a slight gradient in stretch blow-molded PET bottles. A thick parison combined with radiant heating and the inherent dynamics of the process are believed to be the combined source of the gradient. It is suggested that the application of interference microscopy to the study of the gradients in blow molded PET bottles would be a fertile area for developing a better understanding of the bottle blowing process and the techniques for evaluating through the thickness gradients.

LIST OF REFERENCES

LIST OF REFERENCES

1. Adams, G.C., Polym. Eng. Sci., 16, 222 (1976).

2. Alles, F.P., (E.I. du Pont de Nemours and Co.) U.S. Patent 2,884,663 (May 5, 1959).

3. Alles, F.P., and W.R. Saner, (E.I. du Pont de Nemours and Co.) U.S. Patent 2,627,088 (Feb. 3, 1953).

4. Arnott, S. and A.J. Wonacott, Polymer, 7, 137 (1966).

5. Baker, W.P., J. Polym. Sci., 57, 993 (1962).

6. Barakat, N., Textile Res. J., 41, 167 (1971).

7. Barakat, N. and H.A. El-Hennawi, Textile Res. J., 41, 391 (1971).

8. Baranov, V.G., A.V. Kenarov and T.I. Volkov, J. Polym. Sci., Part C, 30, 271 (1970).

9. Bennett, J.M. and H.E. Bennett in "Handbook of Optics", W. G. Driscoll and W. Vaughan Eds., McGraw-Hill, New York (1978).

10. Blumentritt, B.F., J. Appl. Polym. Sci., 23, 3205 (1979).

11. Bonart, R., Kolloid Z.Z. Polym., 199, 136 (1964).

12. Brazinsky, I. and H.L. Davis, Polym. Eng. Sci., 18, 955 (1978).

13. Carr, S.H., P.H. Geil and E. Baer, J. Macromol. Sci. (Phys.), B2, 13 (1968).

14. Cakmak, M., J.E. Spruiell and J.L. White, PATRA Report No. 209, The University of Tennessee, Knoxville, TN, August 1983.

15. Casey, M., Polymer, 18, 1219 (1977).

16. Clark, E.S., SPE J., 23, 46 (1967).

17. Clark, E.S., Appl. Polym. Symp., 24, 45 (1974).

18. Clark, E.S. and C.A. Garber, Intern. J. Polym. Mater., 1, 31 (1971).

19. Cobbs, W.H. and R.L. Burton, J. Polym. Sci., 10, 275 (1953).

20. Crank, J. and P. Nicolson, Proc. Cam. Phil. Soc., 43, 50 (1947).

21. Croft, D.R. and D.G. Lilley, "Heat Transfer Calculations Using Finite Difference Equations", Applied Science Publishers LTD, London (1977).

22. Cunningham, A., I.M. Ward, H.A. Willis and V. Zichy, Polymer, 15, 749 (1974).

23. Daubeny, R de P., C.W. Bunn and C.J. Brown, Proc. Roy. Soc. (London), A226, 531 (1954).

24. Dulmage, W.J. and A.L. Geddes, J. Polym. Sci., 31, 499 (1958).

25. Duong, D.T. and J.P. Bell, J. Polym. Sci., Polym. Phys. Ed., 13, 765 (1975).

26. Elias, H.G., "Macromolecules", Vol 2., Plenum Press, New York, (1977).

27. Elsner, G., M.H.J. Koch and J.R. Milch, Makromol. Chem., 182, 657 (1981).

28. Elsner, G., M.H.J. Koch, J. Bordas and H.G. Zachmann, Makromol. Chem., 182, 1263 (1981).

29. Fakirov, S., Polymer, 21, 373 (1980).

30. Fakirov, S., E.W. Fischer and G.F. Schmidt, Makromol. Chem., 176, 2459 (1975).

31. Faust, R.C., Proc. Roy. Soc., A211, 240 (1952).

32. Faust, R.C., Proc. Phys. Soc., B65, 48 (1952).

33. Faust, R.C., Proc. Phys. Soc., B67, 138 (1954).

34. Frankfort, R.E. and B.H. Knox, (E.I. du Pont de Nemours and Co.) U.S. Patent 4,134,882 (Jan. 16, 1979).

35. Foster, H.O. and D.E. Hook, Proc. 5th Itern. Congress on Rheology, Vol. 3. (Kyoto, Japan), 255 (1968).

36. Fouda, I.M., A.A. Hamza, M.M. El-Nicklawy and K.A. El-Farhaty, Textile Res. J., 40, 355 (1981).

37. Frolova, A.A. and P.V. Kozlov, J. Polym. Sci. (USSR), 7, 479 (1965).

38. Garber, C.A. and E.S. Clark, J. Macromol. Sci. (Phys.), B4, 499 (1970).

39. Geil, P.H., G.S.Y. Yeh, J.L. Koenig and M.J. Hannon, J. Macromol. Sci. (Phys.), B1, 793 (1967).

40. Goodman, I. and J.A. Rhys, "Polyesters", Vol. 1, American Elsevier, New York, (1965).

41. Groeninckx, G., H. Reynaers and H. Berghmans, Polymer, 15, 61 (1974).

42. Hale, A.J., "The Interference Microscope in Biological Research", E. S. Livingston LTD., London, 1958.

43. Hamza, A.A., I.M. Fouda, K.A. El-Farhaty and Y.K. Badawy, Textile Res. J., 50, 592 (1980).

44. Hamza, A.A. and H.I. Abd El-Kader, Textile Res. J., 53, 205 (1983).

45. Hamza, A.A. and J. Sikorski, J. Microsoc., 113, 15 (1978).

46. Hansen, D., A.N. Taskar and O. Casale, J. Polym. Sci. 10, 1615 (1972).

47. Hartley, F.D., F.W. Lord and L.B. Morgan, Phil. Trans. Roy. Soc. (London), A247, 23 (1954).

48. Haugh, E.F., (E.I. du Pont de Nemours and Co.) U.S. Patent 2,904,841 (Sept. 22, 1959).

49. Heffelfinger, C.J. Polym. Eng. Sci., 18, 1163 (1978).

50. Heffelfinger, C.J. and R.L. Burton, J. Polym. Sci., 47, 289 (1960).

51. Heffelfinger, C.J. and E.L. Lippert, J. Appl. Polym. Sci., 15, 2699 (1971).

52. Heffelfinger, C.J. and K.L. Knox in "The Science and Technology of Polymer Films", Vol. 2, O. J. Sweeting Ed., Wiley-Interscience, New York, (1971), p. 587-639.

53. Heffelfinger, C.J. and P.G. Schmidt, J. Appl. Polym. Sci., 9, 2661 (1965).

54. Hergenrother, W.L., J. Polym. Sci., Polym. Chem. Ed., 12, 875 (1974).

55. Hergenrother, W.L. and C.J. Nelson, J. Polym. Sci., Polym. Chem. Ed., 12, 2905 (1974).

56. Hinrichsen, G., H.G. Adam, H. Krebs and H. Springer, Coll. Polym. Sci., 258, 232 (1980).

57. Holmes, D.A., J. Opt. Soc. Am., 54, 1340 (1964).

58. Hovenkamp, S.G. and J.P. Munting, J. Polym. Sci.(A-1), 8, 679, (1970).

59. Hutchinson, I.J., I.M. Ward, H.A. Willis and V.Zichy, Polymer, 21, 55 (1980).

60. Ito, E. and T. Hatakeyama, J. Polym. Sci., Polym. Phys. Ed., 12, 1477 (1974).

61. Iyer, K.R., S. Screenivasan and N.B. Patil, Textile Res. J., 53, 442 (1983).

62. Kashiwagi, M., A. Cunningham, A.J. Manuel and I.M. Ward, Polymer, 14, 111 (1973).

63. Keller, A.J., J. Polym. Sci., 17, 291 (1955).

64. Keller, A., G.R. Lester and L.B. Morgan, Phil. Trans. Roy. Soc. (London), A247, 1 (1954).

65. Keller, A.J. and T. Waring, J. Polym. Sci., 17, 447 (1955).

66. Kilian, H.G., M. Haboth and E. Jenckel, Kolloid Z.Z. Polym., 172, 166 (1960).

67. Klement, J.J. and P.H. Geil, J. Macromol. Sci. (Phys.), B5, 505 (1971).

68. Klement, J.J. and P.H. Geil, J. Macromol. Sci. (Phys.), B5, 535 (1971).

69. Knox, K.L., (E.I. du Pont de Nemours and Co.), U.S. Patent 2,718,666 (Sept. 27, 1955).

70. Kolb, M.J. and E.F. Izard, J. Appl. Phys., 20, 571 (1949).

71. Koenig, J.L. and S.W. Cornell, J. Macromol. Sci. (Phys.), B1, 279 (1967).

72. Koenig, J.L., S.W. Cornell and D.E. Witenhafer, J. Polym. Sci. Part A, 5, 301 (1967).

73. Konda, A., K. Nose and H. Ishikawa, J. Polym. Sci., Polym. Phys. Ed., 14, 1495 (1976).

74. Koppehele, H.P., (American Viscose Corp.), U.S. Patent 3,055,048 (Sept. 25, 1962).

75. Korshak, V.V. and S.V. Vinogradova, "Polyesters", Pergamon Press, Oxford, (1965), p. 384-447.

76. Matsuo, M., M. Tamada, T. Terada, C. Sawatari and M. Niwa, Macromolecules, 15, 988 (1982).

77. Masuko, T., H. Tanaka and S. Okajima, J. Polym. Sci. (A-2), 8, 1565 (1970).

78. Mauro, J.B. and J.J. Levitsky in "The Science and Technology of Polymer Films", Vol. 1, O. Sweeting Ed., Wiley-Interscience, New York, (1968), p. 459-479.

79. Mayhan, K.G., W.J. James and W. Bosch, J. Appl. Polym. Sci., 9, 3605 (1965).

80. McCrone, W.C. and J.G. Delly, "The Particle Atlas", Vol. 1, Ann Arbor Science Publishers Inc., Ann Arbor Michigan, (1973), p. 34-39.

81. McGraw, G.E., J. Polym. Sci. (A-2), 8, 1323 (1970).

82. McKinney, P.V. and C.R. Foltz, J. Appl. Polym. Sci., 11, 189 (1967).

83. Merton, T., Proc. Roy. Soc., A189, 309 (1947).

84. Merton, T., Proc. Roy. Soc., A191, 1 (1947).

85. Miller, M. and D.R. McGregor, (E.I. du Pont de Nemours and Co.), U.S. Patent 2,920,352 (Jan. 12, 1960).

86. Misra, A. and R.S. Stein, J. Polym. Sci., Polym. Phys. Ed., 11, 108 (1973).

87. Misra, A. and R.S. Stein, J. Polym. Sci., Polym. Phys. Ed., 17, 235 (1979).

88. Mocherla, K.K. and J.P. Bell, J. Polym. Sci., Polym. Phys. Ed., 11, 1779 (1973).

89. Morgan, L. B. Phil. Trans. Roy. Soc. (London), A247, 13 (1954).

90. Muzzy, J.D., D.G. Bright and G.H. Hoyos, Polym. Eng. Sci., 18, 437 (1978).

91. Nobbs, J.H., D.I. Bower and I.M. Ward, Polymer, 17, 25 (1976).

92. Nobbs, J.H., D.I. Bower, I.M. Ward and D. Patterson, Polymer, 15, 287 (1974).

93. Okajima, S. and Y. Koizumi, Kogyo Kagaku Zasshi, 42, 810 (1939).

94. Ozisik, M.N., "Heat Conduction", Wiley-Interscince, New York, 1980 p. 471-519.

95. Pace, A. (E.I. du Pont de Nemours and Co.), U.S. Patent 2,578,899 (Dec. 18, 1951).

96. Pai, V.K. and D. Hyman, Textile Res. J., 42, 639 (1972).

97. Perna, J.M., R.A. Duckett and I.M. Ward, J. Appl. Polym. Sci., 25, 1381 (1980).

98. Plastics World, Feb. 1982 P. 57.

99. Plastics World, Mar. 1982 p. 11.

100. Pluta, M., Opt. Acta., 18, 661 (1971).

101. Pluta, M., J. Microsc., 6, 309 (1972).

102. Pollard, P. and J.D. Perkins, Polymer, 17, 1103 (1976).

103. Prud'homme, R.E., L. Bourland, R.T. Natarajan and R.S. Stein, J. Polym. Sci., Polym. Phys. Ed., 12, 1955 (1974).

104. Personal Communication H.A. Davis (E.I. du Pont de Nemours and Co.).

105. Private Communication (American Hoechst Corporation).

106. Rabesiaka, J. and A.J. Kovacs, J. Appl. Phys., 32, 2314 (1961).

107. Reddish, W., Pure and Appl. Chem., 5, 723 (1962).

108. Renninger, A.L. and D.R. Uhlmann, J. Polym. Sci., Polym. Phys. Ed., 14, 415 (1976).

109. Rhodes, R.S. in " Structure and Properties of Polymer Films", R. W. Lenz and R. S. Stein Eds., Plenum Press, New York (1973), p. 113.

110. Rietsch, F., R.A. Duckett and I.M. Ward, Polymer 20, 1133 (1979).

111. Robertson, R.E., J. Phys. Chem., 69, 1575 (1965).

112. Roche, E.J. and H.A. Davis, Preprints of the Fiber Producers Research Conference (Greenville, S. C.) August 1983.

113. Rochow, T.G. and E.G. Rochow, "An Introduction to Microscopy by Means of Light, Electrons, X-rays or Ultrasound", Plenum Press, New York, (1978).

114. Roylance, D. and M. Roylance, J. Polym. Sci., Part C, 10, 273 (1972).

115. Samuels, R.J., J. Polym. Sci. (A-2), 7, 1197 (1969).

116. Samuels, R.J., J. Appl. Polym. Sci., 26, 1383 (1981).

117. Schael, G.W., J. Appl. Polym. Sci., 8, 2717 (1964).

118. Schael, G.W., J. Appl. Polym. Sci., 12, 903 (1968).

119. Scarlett, A.C., (E.I. du Pont de Nemours and Co.), U.S. Patent 2,823,421 (Feb. 18, 1958).

120. Sheldon, R.P., Polymer, 4, 213 (1963).

121. Shih, N.C. and S. Middleman, Polym. Eng. Sci., 10, 4 (1970).

122. Shimizu, J., N. Okui, and T. Kikutai, Sen-i Gakkaishi, 33, T135 (1977).

123. Shimizu, J., N. Okni, T. Kitutani, A. Ono and A. Takaku, Sen-i Gakkaishi 37, T143, (1981).

124. Siegmann, A. and E. Turi, J. Macromol. Sci. (Phys.), B10, 689 (1974).

125. Sifleet, W.L., N. Dinos and J.R. Collier, Polym. Eng. Sci., 13, 10 (1973).

126. Slayter, E.M., "Optical Methods in Biology", Wiley-Interscience, New York, (1970).

127. Smith, F.S. and R.D. Steward, Polymer, 15, 283 (1974).

128. Spruiell, J.E., D.E. McCord and R.A. Beuerlein, Trans. Soc. Rheol., 16, 535 (1972).

129. Starkweather, H.W. and R.E. Brooks, J. Polym. Sci., 1, 236 (1959).

130. Statton, W.O. and G.M. Godard, J. Appl. Phys., 28, 1111 (1957).

131. Steel, W.H. "Interferometry", Cambridge University Press, London (1967).

132. Steel, W.H. Microscope, 18, 303 (1970).

133. Stein, R.S., J. Polym. Sci., 24, 383 (1957).

134. Stein, R.S., Polym. Eng. Sci., 16, 152 (1976).

135. Stein, R.S. and M.B. Rhodes, J. Appl. Phys., 31, 1873 (1960).

136. Swallow, J.C., D.K. Baird and B.P. Ridge, (Imperial Chemical Industries), U.S. Patent 2,497,376 (Feb. 14, 1950).

137. Tanaka, H., T. Masuko and S. Okajima, J. Appl. Polym. Sci., 16, 441 (1972).

138. Tanaka, H., T. Masuko and S. Okajima, J. Polym. Sci. (A-1), 7, 3351 (1969).

139. Terada, T., C. Sawatari, T. Chigono and M. Matsuo, Macromolecules, 15, 998 (1982).

140. Thompson, A.B., J. Polym. Sci., 34, 741 (1959).

141. Tilgner, R., Coll. Polym. Sci., 254, 972 (1976).

142. Tolansky, S., "An Introduction to Interferometry", Longmans, Green and Co. Ltd., London, (1955).

143. Tolansky, S., "Microstructure of Surfaces Using Interferometry", American Elsevier, New York, (1968).

144. Tomashpolskii, Y.Y. and G.S. Markova, J. Polym. Sci. (USSR), 6, 316, (1964).

145. Van Antwerpen, F. and D.W. Van Krevelen, J. Polym. Sci., Polym. Phys. Ed., 10, 2423 (1972).

146. Van Veld, G. and R.H. Morris, J. Appl. Polym. Sci., 12, 2709 (1968).

147. Wahlstrom, E.E., "Optical Crystallography", John Wiley and Sons, New York, (1978).

148. Whinfield, J.R. and J.T. Dickson, (E.I. du Pont de Nemours and Co.), U.S. Patent 2,465,319 (Mar. 22, 1949).

149. Whinfield, J.R. and J.T. Dickson, (Imperial Chemical Industries), British Patent 578,079 (Mar. 22, 1949).

150. Willard, H.H., L.L. Merritt and J.A. Dean,"Methods of Instrumental Analysis", Van Nostrand, New York (1974), p. 420.

151. Wunderlich, B., Polym. Eng. Sci., 18, 431 (1978).

152. Wust, C.J., Ph.D. Dissertation, The University of Tennessee, Knoxville 1982.

153. Wust, C.J. and D.C. Bogue, J. Appl. Polym. Sci., 28, 1931 (1983).

154. Yamashita, Y., J. Polym. Sci. A-3, 81 (1965).

155. Yeh, G.S.Y. and P.H. Geil, J. Macromol. Sci. (Phys.), B1, 235 (1967).

156. Yeh, G.S.Y. and P.H. Geil, J. Macromol. Sci. (Phys.), B1, 251 (1967).

157. Yokouchi, M., J. Mori and Y. Kobayashi, J. Appl. Polym. Sci., 26, 3435 (1981).

158. Zachmann, H.G. and H.A. Stuart, Makromol. Chem., 41, 131 (1960).

APPENDIX

APPENDIX

COMPUTER PROGRAM USED IN HEAT TRANSFER STUDIES

The following program listing is an adaptation of Program 5.2 presented by Croft and Lilley (21).

```
C   THIS PROGRAM COMPUTES ONE-DIMENSIONAL
C   TEMPERATURE PROFILES IN A POLYMER SHEET
C   USING THE CRANK-NICOLSON NUMERICAL METHOD.
C
      DIMENSION DL(100),TIN(100),T(100,4)
      INTEGER NIN
      REAL DL,INC,INCT,K,L
C
C   INPUT MATERIAL PROPERTIES
C
      READ(40,*) CP,K,RHO
      READ(40,*) L,INC,TRES
      READ(40,*) T1,T2,TSTART,TBULK
      READ(40,*) H1,H2
      WRITE(5,10010)
      WRITE(41,10010)
      WRITE(5,10020)
      WRITE(41,10020)
      WRITE(5,10030) CP,K,RHO
      WRITE(41,10030) CP,K,RHO
      WRITE(5,10040) L, INC,TRES
      WRITE(41,10040) L,INC,TRES
      WRITE(5,10050) T1,T2,TSTART,TBULK
      WRITE(41,10050) T1,T2,TSTART,TBULK
      WRITE(5,10060) H1,H2
      WRITE(41,10060) H1,H2
      NIN=L/INC
      N=NIN+1
      INCT=0.0
C
C   ESTABLISH INITIAL TEMPERATURE PROFILE
C
      DO 20 I=1,N
      TIN(I)=TSTART
      INCT=INCT+INC
      DL(I)=INCT-INC
      IF (I .GT. 1 )  GO TO 10
```

```
      CALL GAUSS(T,N)
      DO 60 I=1,N
      TIN(I)=T(I,4)
60    CONTINUE
      IF(TIME-TNOW)  30,70,70
70    WRITE(5,10120)
      WRITE(41,10120)
      DO 80 I=1,N
      WRITE(5,10130) DL(I),T(I,4)
      WRITE(41,10130) DL(I),T(I,4)
      WRITE(42,10130) DL(I),T(I,4)
80    CONTINUE
C
C  CALCULATE AVERAGE TEMPERATURE
C
      TSUM=0.0
      DO 90 I=1,N
      TSUM=TSUM+T(I,4)
90    CONTINUE
      TAVG=TSUM/N
      TNOW=TNOW+TRES
      DELTA=T(N,4)-T(1,4)
      WRITE(5,10140) TAVG
      WRITE(41,10140) TAVG
      WRITE(5,10150) DELTA
      WRITE(41,10150) DELTA
      WRITE(5,10160) TNOW
      WRITE(41,10160) TNOW
      IF(TBULK-TAVG)  100,30,30
100   CONTINUE
      STOP
10010       FORMAT('1',25X,'MATERIAL: PET CAST SHEET',//,1X,
     1  28X,'MATERIAL PROPERTIES')
10020       FORMAT('+',29X,19('*'),//)
10030       FORMAT(1X,10X,'SPECIFIC HEAT:',F10.3,2X,
     1  '(CAL/GM-DEG. C)',/,1X,10X,'THERMAL CONDUCTIVITY:',
     2  F12.5,2X,'(CAL/(S-CM-DEG. C))',/,1X,10X,
     3  'DENSITY:',F10.3,2X,'(GM/CM**3)')
10040       FORMAT(1X,10X,'THICKNESS:',F6.2,2X,'(MM)',/,
     1  1X,10X,'THICKNESS INCREMENT:',F6.3,2X,'(MM)',/,
     2  1X,10X,'RESIDENCE TIME:',F4.1,2X,'(S)')
10050       FORMAT(1X,10X,'AMBIENT TEMP. (T1):',F8.2,2X,
     1  '(DEG. C)',/,1X,10X,'AMBIENT TEMP. (T2):',F8.2,
     2  2X,'(DEG. C)',/,1X,10X,'INITIAL TEMP:',F8.2,2X,
     3  '(DEG. C)',/,1X,10X,'DESIRED AVERAGE TEMP.:',
     4  F8.2,2X,'(DEG. C)')
```

```
C
C  DISPLAY INITIAL FROFILE
C
      WRITE(5,10070)
      WRITE(41,10070)
      WRITE(5,10080)
      WRITE(41,10080)
10    WRITE(5,10090) DL(I),TIN(I)
      WRITE(41,10090) DL(I),TIN(I)
20    CONTINUE
      WRITE(5,10100)
      WRITE(41,10100)
      WRITE(5,10110)
      WRITE(41,10110)
      TIME=0.0
      TNOW=0.0
      DX=L/(NIN*10)
      DTIME=1.0*C2*RHO*DX**2/K
C
C  DETERMINE COEFFICIENTS FOR THE SYSTEM
C
      C1=H1/K
      C2=H2/K
C
C  COMPUTE MATRIX COEFFICIENTS
C
30    T(1,1)=0.0
      T(1,2)=-4.0-2.0*C1*DX
      T(1,3)=2.0
      T(N,1)=2.0
      T(N,2)=-4.0-2.0*C2*DX
      T(N,3)=0.0
      DO 40 I=2,NIN
      T(I,1)=1.0
      T(I,2)=-4.0
      T(I,3)=1.0
40    CONTINUE
      T(1,4)=-2.0*TIN(2)+2.0*C1*DX*TIN(1)-4.0*C1*DX*T1
      T(N,4)=-2.0*TIN(N-1)+2.0*C2*DX*TIN(N)-4.0*C2*DX*T2
      DO 50 I=2,NIN
      T(I,4)=-TIN(I-1)-TIN(I+1)
50    CONTINUE
C
C  COMPUTE TEMPERATURE PROFILE
C
C  CALL SUBROUTINE GAUSS TO SOLVE THE SYSTEM OF EQUATIONS
C
      TIME=TIME+DTIME
```

```
10060       FORMAT(1X,10X,'HEAT TRANS. COEFF.
(H1):',F9.5,2X,
     1  '(CAL/(S-CM**2-DEG. C))',/,1X,10X,'HEAT TRANS. COEFF.
(H2):',
     2  F9.5,2X,'(CAL/(S-CM**2-DEG. C))')
10070       FORMAT(1X,/////,1X,20X,'INITIAL TEMP. PROFILE')
10080       FORMAT('+',20X,21('*'),//,1X,10X,'DISTANCE
(MM)',10X,
     1  'TEMP. (DEG. C)')
10090       FORMAT(1X,10X,F8.2,17X,F8.2)
10100       FORMAT('1',//,1X,20X,'TEMPERATURE PROFILE')
10110       FORMAT('+',20X,19('*'),//)
10120       FORMAT(1X,//,1X,10X,'DISTANCE (MM)',10X,'TEMP.
(DEG. C)',/)
10130       FORMAT(1X,10X,F8.2,17X,F8.2)
10140       FORMAT(1X,//,1X,10X,'AVERAGE
TEMP.:',F8.2,2X,'(DEG. C)')
10150       FORMAT(1X,10X,'DELTA TEMP.:',F8.2,2X,'(DEG. C)')
10160       FORMAT(1X,10X,'TIME:',F8.1,2X,'(S)')
     END
C            SUBROUTINE GAUSS
C
     SUBROUTINE GAUSS(Z,N)
     DIMENSION A(100),B(100),C(100),D(100),Z(100,4)
C
C  INITIALIZE COEFFICIENT MATRIX
C
     DO 10 J=1,N
     A(J)=Z(J,1)
     B(J)=Z(J,2)
     C(J)=Z(J,3)
     D(J)=Z(J,4)
10   CONTINUE
C
C  COMPUTE NEW MATRIX ELEMENTS
C
     DO 20 J=2,N
     S=A(J)/B(J-1)
     B(J)=B(J)-S*C(J-1)
     D(J)=D(J)-S*D(J-1)
20   CONTINUE
```

```
C
C BACK SUBSTITUTE VALUES INTO SOLUTION MATRIX D(N)
C
      D(N)=C(N)/B(N)
      DO 30 J=2,N
      M=N-J+1
      D(M)=(D(M)-C(M)*D(M+1))/B(M)
30    CONTINUE
      DO 40 J=1,N
      Z(J,4)=D(J)
40    CONTINUE
      RETURN
      END
```

Source: Croft, D.R. and D.G. Lilley in "Heat Transfer Calculations Using Finite Difference Equations", Applied Science Publishers, LTD (1977) p. 275-277.

VITA

Richard John Wilk was born on January 21, 1959 in New York (QUEENS), New York. He received a Bachelor of Science degree in Chemical Engineering from the Polytechnic Institute of New York, Brooklyn, New York in June 1981. Upon graduation the author worked for Fiber Industries Inc. (Celanese Corporation) located in Charlotte, North Carolina. He entered the Polymer Engineering program at the of Tennessee September 1981. During his stay at the university, he participated in a graduate work-study program sponsored by the Film Division of American Hoechst Corporation (Greer, South Carolina).

The author is a member of Tau Beta Pi, Omega Chi Epsilon, the American Chemical Society, the American Institute of Chemists, the American Institute of Chemical Engineers, the Chemists' Club, the New York Academy of Sciences, the Society of Plastics Engineers, the Society of Rheology and the Technical Association of the Pulp and Paper Industry.